21 cm Line Astronomy and Constraining New Physics

A Thesis Submitted
in Partial Fulfilment of the Requirements
for the Degree of
Doctor of Philosophy

by

Pravin Kumar Natwariya
Roll No. *17330022*

Under the guidance of

Prof. Jitesh R. Bhatt
Theoretical Physics Division
Physical Research Laboratory, Ahmedabad 380009, India.

to the

Discipline of Physics
Indian Institute of Technology Gandhinagar,
Gujarat 382355, India.

June 2022

DECLARATION

I hereby declare that the work contained in this thesis represents my ideas in my own words and where others ideas or words have been included, I have adequately cited and referenced the original sources. I also declare that I have adhered to all principles of academic honesty and integrity and have not misrepresented or fabricated or falsified any idea/data/fact/source in my submission. I understand that any violation of the above can cause disciplinary action by the Institute and can also evoke penal action from the sources which have thus not been properly cited or from whom proper permission has not been taken when needed.

Signature: 

Pravin Kumar Natwariya
IITGn Roll No: 17330022
Theoretical Physics Division,
Physical Research Laboratory,
Ahmedabad 380009, India.

Date: 16 December 2022

Discipline of Physics,
Indian Institute of Technology Gandhinagar,
Gujarat 382355, India.

CERTIFICATE

It is certified that the work contained in the thesis entitled ***"21 cm Line Astronomy and Constraining New Physics"***, submitted by ***Pravin Kumar Natwariya (Roll No. 17330022)*** to the Indian Institute of Technology Gandhinagar, is a record of bona fide research work carried out with my supervision and has not been submitted elsewhere for a degree. I have read this dissertation and in my opinion, it is fully adequate, in scope and quality, for the degree of Doctor of Philosophy.

Signature:_____

Prof. Jitesh R. Bhatt
Theoretical Physics Division
Physical Research Laboratory
Ahmedabad 380009, India.
(Thesis Supervisor)

Date: 16 December 2022

List of publications included in the thesis

1. **Pravin Kumar Natwariya** and Alekha C. Nayak, ***"Bounds on sterile neutrino lifetime and mixing angle with active neutrinos by global 21 cm signal"***, *Physics Letters B* 827 (2022) 136955.
   DOI: https://doi.org/10.1016/j.physletb.2022.136955

2. **Pravin Kumar Natwariya**, Alekha C. Nayak and Tripurari Srivastava, ***"Constraining spinning primordial black holes with global 21-cm signal "***, *Mon Not R Astron Soc* 510, 4236–4241 (2022).
   DOI: https://doi.org/10.1093/mnras/stab3754

3. **Pravin Kumar Natwariya**, ***"Constraint on Primordial Magnetic Fields In the Light of ARCADE 2 and EDGES Observations"***, *Eur. Phys. J. C* 81 (2021) 5, 394.
   DOI: https://doi.org/10.1140/epjc/s10052-021-09155-z

4. Jitesh R. Bhatt, **Pravin Kumar Natwariya**, Alekha C. Nayak and Arun Kumar Pandey, ***"Baryon-Dark matter interaction in presence of magnetic fields in light of EDGES signal"***, *Eur. Phys. J. C* 80 (2020) 4, 334.
   DOI: https://doi.org/10.1140/epjc/s10052-020-7886-x

List of publications not included in the thesis

1. **Pravin Kumar Natwariya** and Jitesh R. Bhatt, ***"EDGES signal in the presence of magnetic fields"***, *Mon Not R Astron Soc: Letters* 497 (2020) 1, L35-L39.
   DOI: https://doi.org/10.1093/mnrasl/slaa108

2. **Pravin Kumar Natwariya**, Jitesh R. Bhatt and Arun Kumar Pandey, ***"Viscosity in cosmic fluids"***, *Eur. Phys. J. C* 80 (2020) 8, 767.
   DOI: https://doi.org/10.1140/epjc/s10052-020-8341-8

3. Arun Kumar Pandey, **Pravin Kumar Natwariya** and Jitesh R. Bhatt, ***"Magnetic fields in a hot dense neutrino plasma and the Gravitational Waves"***, *Phys. Rev. D* 101 (2020) 2, 023531.
   DOI: https://doi.org/10.1103/PhysRevD.101.023531

4. Kuldeep J. Purohit, **Pravin Kumar Natwariya**, Jitesh R. Bhatt and Prashant K. Mehta, ***"Rotating Scalar Field and Formation Of Bose Stars"***, arXiv:2109.02601 [astro-ph.CO].
   DOI: https://doi.org/10.48550/arXiv.2109.02601

Some choose the long road indefatigably;

Some alter the goal in pursuit of pleasure.

—Author

Enjoy the thesis...

To

my parents,

all my teachers,

Alekha & Tripurari.

ACKNOWLEDGEMENTS

It's been a joyous and exhilarating five years journey at PRL Ahmedabad, and I wish to express my deepest thanks to all the people who have been helpful during this journey. It has been one of the best duration, and as a physicist, I have learned a lot over these years. I believe that a person's success depends on the guidance, encouragement, and kind support of many individuals and organizations.

I would like to start by thanking PRL as an organization for providing a friendly and healthy academic environment to work here as a PhD student. I express my gratitude to all of them who have/had been involved in the establishment and nurturing of this institute. I am grateful to the Indian Institute of Technology, Gandhinagar (IITGn), for my PhD registration.

I am very grateful to my thesis supervisor, Prof. Jitesh R. Bhatt, for the continuous encouragement, good spirit, support and suggestions for academic/non-academic matters. Without him, I could not have enjoyed such a fulfilling and exciting journey. I have learned a lot of lessons from him. These lessons have been very beneficial and will remain for the coming years. Above all, I thank him for letting me feel free to work on what was interesting to me. It has been an absolute joy to work and discussing over various global issues with him over the years.

I would like to convey my sincere thanks to the members of my doctoral studies committee (DSC), Prof. Hiranmaya Mishra, Prof. Partha Konar and Prof. Aveek Sarkar, for the fruitful academic discussions, advice which helped me a lot all along and review of my thesis. I have gained a lot of knowledge from the discussions during DSC reviews. My Special thanks to Prof. Aveek Sarkar for the encouragement, good spirit, advice and help whenever needed and, even more importantly, for his friendly gesture.

I must also thank all the faculty members of our theoretical physics group— Prof. Subhendra Mohanty, Prof. Namit Mahajan, Prof. Srubabati Goswami, Prof. Dilip Angom, Prof. Navinder Singh and Dr Ketan M. Patel, for all the support, encouragement and several valuable scientific discussions on various occasions. I have been benefited immensely from their constructive criticism and suggestions. I thank area chairman Prof. Hiranmaya Mishra for providing the necessary facilities

to pursue my research smoothly.

I sincerely thank all my collaborators and seniors, Dr Alekha C. Nayak, Dr Tripurari Srivastava, Dr Arvind Kumar Mishra, Dr Arun Pandey and Kuldeep J. Purohit, for all the help and scientific discussions. Especially my sincere regards and respect to Dr Alekha C. Nayak and Dr Tripurari Srivastava for their inspiration & guidance and for providing me support in all kinds of situations whenever needed during all these years.

The whole graduate experience would have been nothing without my academic siblings & partners in crime, Ramanuj Mitra, Sovan Saha, Sudipta Show, Sarika and Satyajeet. I would like to thank them for all the times we spent together in laughter & worry and the late-night food, tea and discussions. Especially for the past few months, the dinner we are sharing & eating together has been a memorable experience. During the pandemic days, the late-night walks and debates over various things with Prithish & Ramanuj were an immense joy. Thank you for keeping my journey vibrant and happy. I would like to mention some YouTube channels that have kept me entertained through all these years: TSP (S.S. Parihar, Badri, Abhinav), Jonna Jinton and casetoo (Aditya).

It would have been impossible to pass the five years without the joyful company of my dear batch mates, all the seniors and juniors in PRL. A special mention to my batch mates Abhijit, Vishal, Anshika, Hrushikesh, Deepak, Tanmay, Alka, Shivani, Sana, Ankit, Aravind, Vipin, Shanwlee, Sushant, Kamlesh, Milan, Himanshu, Subith, Madhusudhan, Biswajit, Neeraj, Abhay, Suraj and Hirdesh for all the enjoyment and parties we had together all along. I want to thank the sports group, Gurucharan, Debashis, Dharmendra, Kamran, Ashish, Kaustav, Priyank, Atif, Partha, Bharti, Saurabh, Amit, and others, at Navragpura hostel for keeping the hostel environment lively. I also would like to thank my esports teammates Santu, Soumya and Rahul. I thank my friends from graduation and school days, Dinesh, Sanwar, Ritesh, Hemant, and Dahiya, who always kept me cheerful.

I am thankful to the PRL administration, computer centre and library people for their academic and technical help. I would like to thank Dr Anil Bhardwaj (Director, PRL), Dr Nishtha Anilkumar (Head, Library), Mr Jigarbhai A Raval (Head, Computer Centre), Dr Bhushit Vaishnav (Head, Academic Services) and

Mr Anand D. Mehta for their assistance during all these years. I would also like to acknowledge the PRL Library and Vikram - 100 HPC Cluster. It has been an excellent experience to be a part of PRL family.

The acknowledgements will remain incomplete without my sincere gratitude to my family and close relatives for their support for 26 years and counting. My parents, grandparents and brother provided me with every opportunity to explore my passions and pursue that. And last but not least, I am immensely grateful to Venus for her endless support in the pursuit of my goals. I can't wait for what adventures may come. Their support, sacrifice and pride in my accomplishments and unconditional love sustained my endeavours, and I will always be thankful for that. I do not have any adequate words to express their contributions. I am also grateful to my mentors and teachers during undergrad and postgrad, Prof. Akhilesh Pandey and Rakesh Sir. Without them, I could not have fulfilled my dreams and achieved what I have achieved today.

My sincerest apologies to anyone left out. I am honoured and grateful to have shared a long road with all these people.

I would also like to thank all Referees for their suggestions that significantly improved the quality of the thesis.

I am very excited to continue my life as a researcher during the next phase of my career.

Thank you all.

Pravin,

Ahmedabad, 2022

Synopsis

Name:	Pravin Kumar Natwariya
Roll No.:	*17330022*
Degree for which submitted:	Doctor of Philosophy
Department:	Physics
Thesis Title:	21 cm Line Astronomy and Constraining New Physics
Thesis Supervisor:	Prof. Jitesh R. Bhatt
Month & year of submission:	May 2022

The 21 cm signal appears to be a treasure trove to provide an insight into the period when the first generation of luminous objects sprung up in the Universe—hereafter, we will refer to these objects as first stars. The 21 cm line has been actively used to trace the neutral hydrogen in Milky Way for more than seven decades since its first observation in 1951 [1]. The 21 cm line corresponds to the wavelength for hyperfine transition between 1S singlet and triplet states of a neutral hydrogen atom, and the corresponding frequency is 1420.4 MHz. Hydrogen is the predominating fraction of the total baryonic matter during cosmic dawn (CD). Therefore, it is convenient and advantageous to study physics during CD using the 21 cm signal. The transition probability for the hyperfine states is once in $\sim 10^7$ years in the absence of any external sources. The presence of any

exotic source of energy can significantly affect the hyperfine transition, thus spin temperature of the hydrogen gas. The spin temperature ($T_{\rm S}$) is characterized by the number density ratio in the 1S singlet and triplet states of the neutral hydrogen atom. In the cosmological scenarios, there are three processes that can affect the spin temperature: background radio radiation, Lyα radiation from the first stars and collisions of a hydrogen atom with another hydrogen atoms, residual electrons or protons. During CD era, the 21 cm signal is observed in the form of differential brightness temperature. If a light with initial brightness temperature ($T_{\rm R}$) passes through a medium having optical depth (τ_ν) & excitation temperature ($T_{\rm exc}$), there can be an absorption or emission by the medium resulting in a different final/emergent brightness temperature ($T'_{\rm R}$). The divergence of $T'_{\rm R}$ from the $T_{\rm R}$ is known as the differential brightness temperature— observed temperature by antennas. In our case, the medium is neutral hydrogen gas and the $T_{\rm exc}$ for the 21 cm line is $T_{\rm S}$. Therefore, we refer the observed antenna temperature by 21 cm differential brightness temperature [2, 3],

$$T_{21} = \frac{T_{\rm S} - T_{\rm R}}{1+z} \times (1 - e^{-\tau_\nu}) \,,$$

here, z is the redshift. Depending on spin and background radio radiation temperature, there can be three scenarios: $T_{\rm S} > T_{\rm R}$ ($T_{21} > 0$, emission signal), $T_{\rm S} = T_{\rm R}$ ($T_{21} = 0$, no signal), $T_{\rm S} < T_{\rm R}$ ($T_{21} < 0$, absorption signal).

Usually, in the ΛCDM model of cosmology, the contribution in the background radiation is assumed to be solely by the cosmic microwave background radiation (CMBR). Therefore, here, we will discuss the evolution of the global 21 cm signal when only CMBR is present as background radiation ($T_{\rm CMB}$). At the redshift of interest ($z \sim 17$), gas temperature ($T_{\rm gas}$) strongly couples to $T_{\rm S}$ due to Lyα radiation emitted from first stars by Wouthuysen-Field (WF) effect [2, 4]. During CD era, $T_{\rm gas}$ and $T_{\rm CMB}$ fall adiabatically as $\propto (1+z)^2$ & $(1+z)$, respectively. Therefore, $T_{\rm S} \sim T_{\rm gas} < T_{\rm CMB}$, and it implies a 21 cm absorptional signal during

CD era. The presence of any exotic source of energy can inject energy into the intergalactic medium (IGM) and heat the gas. Subsequently, it can modify the absorption amplitude in the global 21 cm signal. Therefore, the absorption feature in the 21 cm signal can provide a robust bound on such sources of energy injection into IGM. In the thesis, the following four works has been considered done by me: sterile neutrinos and primordial black holes as dark matter candidates and constrain their properties in the light of the global 21 cm signal. Another two works discussed in the thesis are related to the constraining strength of primordial magnetic fields that might have been generated in the very early Universe.

In 2018, the Experiment to Detect the Global Epoch of Reionization Signature (EDGES) collaboration reported an absorption profile for the 21 cm signal in the redshift range $15 - 20$ [5]. Recently, many articles have questioned the EDGES measurement; for example, see the Refs. [6–8]. In the light of these controversies, in the recent two articles (**A1** & **A2**), we do not consider the absorption amplitude reported by the EDGES collaboration. While in the older two articles (**B1** & **B2**), we have considered the absorption amplitude reported by the EDGES collaboration.

Work carried out for Doctorate Research

A. Dark Matter Models

About 85 per cent of the total matter content in the Universe is dominated by dark matter. In the last decade, many dark matter models, such as collisionless cold dark matter, fuzzy cold dark matter, warm dark matter, and self-interacting dark matter, have been proposed to explain various astrophysical observations. However, the nature of dark matter is still unknown. During my doctoral research, I consider sterile neutrinos and primordial black holes as dark matter candidates and constrain their properties using the absorption feature in 21 cm differential brightness temperature during CD era.

A1. Sterile Neutrino Dark Matter

In the warm dark matter models, one of the theoretically well-motivated candidates is KeV mass sterile neutrinos. Sterile neutrinos are radiatively unstable and can inject photon energy into the IGM. The injection of energy into the IGM can modify the temperature and ionization history of the Universe. Thus it can influence the absorption amplitude of the global 21 cm signal during the CD era. This leads to constraining the lifetime of sterile neutrinos and the mixing angle of sterile neutrinos with active neutrinos. Here, we take 21 cm differential brightness temperature such that it does not change, from its maximal value based on ΛCDM framework ($|T_{21}| \sim 220$ mK), by a factor of more than 1/4 (i.e. -150 mK) or 1/2 (i.e. -100 mK) at redshift 17.2 . This method can also be used for different values of T_{21}. We find that the lower bound on the sterile neutrino lifetime varies from 1.5×10^{28} sec to 1.7×10^{26} sec by varying sterile neutrino mass from 2 KeV to 50 KeV. While the upper bound on the mixing angle varies from 3.8×10^{-9} to 3.42×10^{-14} by varying sterile neutrino mass from 2 KeV to 50 KeV [9].

A2. Primordial Black Hole Dark Matter

Primordial black holes have attracted much interest in recent years and have been a part of intense studies for more than five decades. The idea of the black hole goes back to the 18th century. In 1784, John Michell proposed that there could be such supermassive bodies that light could not pass them, or all light emitted would return towards them [10–12]. As PBHs are massive, interact only gravitationally and are formed in the very early Universe, they can be considered as a potential candidate for non-particle dark matter. Recently, PBHs have gathered much attention in the scientific community after the black hole binary merger detection by Virgo and LIGO collaborations [13–15]. Hawking evaporation of PBHs can inject energy into the IGM and, therefore, can be constrained by the absorption feature in the global 21 cm signal. The mass and spin are fundamental properties

of a black hole, and they can substantially affect the evaporation rate of the black hole. In this work, we have derived an upper bound on the dark matter fraction in the form of the primordial black holes with a non-zero spin. It also implies a lower bound on PBHs mass, which is allowed to constitute the entire dark matter to 6.7×10^{17} g for extremal spinning PBHs [16].

B. Primordial Magnetic Fields

Observations suggest that the magnetic fields (MFs) are ubiquitous in the Universe— from the length scale of planets and stars to the cluster of galaxies [17–20]. Fermi and High Energy Stereoscopic System (HESS) gamma-ray observation suggests that even the IGM in voids could host a magnetic field with a strength of $\sim 10^{-16}$ G with typical coherent scale around a Mpc [21, 22]. It would be very difficult to explain the magnetic fields in the voids and high redshift galaxies with only late-time astrophysical processes without magnetic fields from the very early Universe— primordial magnetic fields (PMFs). The origin and evolution of PMFs are one of the outstanding problems of modern cosmology (Refs. [23, 24] and references cited therein).

The decaying PMFs can inject magnetic energy into the thermal energy of the IGM gas and heat it above the 6.7 K at $z = 17$. The EDGES collaboration reported an absorption profile for 21 cm signal with an amplitude of $T_{21} = -500^{+200}_{-500}$ mK in the redshift range $15 - 20$. This absorption is nearly two times smaller than predicted by theoretical models based on the ΛCDM framework. To explain the anomaly, one requires that either the gas temperature be less than 3.2 K when the background radiation is solely CMB or background radiation temperature be greater than 104 K in the presence of standard evolution of gas temperature. We have explored the upper bounds on the present-day strength of the PMFs in both scenarios by considering different models [25, 26].

B1. In the Light of Excess Radio Radiation

As discussed, one requires to enhance the background radio radiation above the CMB radiation to explain the EDGES anomaly. Although the contribution to the background radiation is assumed to be CMB radiation, the EDGES anomaly encouraged the development of alternative models in which radio background is enhanced. Recently, the Absolute Radiometer for Cosmology, Astrophysics and Diffuse Emission (ARCADE 2) collaboration detected the excess radiation in the frequency range $3-10$ GHz [27]. The enhanced radiation is several times larger than the observed radio counts due to the known Galactic and extragalactic radio processes and sources, such as star-forming galaxies, AGN-driven sources—quasars and radio galaxies, etc. [28, 29]. The presence of early excess radiation can not be completely ruled out. Nevertheless, several theoretical models can explain this excess radio radiation at the time of CD. For example, accreting first intermediate-mass BHs in the redshift range $16-30$ can produce radio radiation. In other scenarios, the excess radiation can be explained by axion-photon conversion or radiative decays of standard model neutrino induced by intergalactic MFs. The enhancement in the radio radiation is also supported by the first station of the Long Wavelength Array (LWA 1) in the frequency range $40-80$ MHz [30]. For excess radiation fraction to be LWA 1 limit, we report the upper bounds on the present-day PMFs strength, B_0 on the scale of 1 Mpc. The following summarises our results for $T_{21} = -500$ mK (EDGES best fit result): $B_0 \lesssim 3.7$ nG for spectral index $n_B = -2.99$. While for $n_B = -1$, we get $B_0 \lesssim 1.1 \times 10^{-3}$ nG. We also discuss the effects of first stars on IGM gas evolution and the allowed value of B_0. By decreasing excess radiation fraction below the LWA 1 limit, we get a more stringent bound on B_0 [25].

B2. In the Light of Baryon-Dark Matter Interaction

One of the alternatives to explain the EDGES anomaly is by cooling the gas below 3.2 K. Since the dark matter is colder than the gas, adequate cooling of the gas can be obtained by introducing the baryon-dark matter interaction beyond the ΛCDM

model. A non-standard Coulomb interaction between dark-matter and baryon: $\sigma = \hat{\sigma} v^{-4}$ can be considered to explain the EDGES signal, where v is the relative velocity between the dark matter and baryon. If one invokes cooling of gas beyond the standard scenario in the presence of baryon dark matter interaction, discussed above, this bound on the strength of PMFs may change by transferring energy of the gas to the dark matter using drag between gas and dark matter. This transfer of energy depends on the dark matter mass and cross-section. Therefore, one can constraint the dark matter mass and cross-section also to get the 21 cm absorption signal. We find that in the presence of such an interaction, the upper bound on the strength of PMFs can significantly be altered. Considering upper bound on $\hat{\sigma} - m_d$ by Planck 2015 and EDGES upper constraint on T_{21} (-300 mK) at $z = 17$, we found upper bound on the present-day strength of PMFs: $B_0 = 3.48 \times 10^{-6}$ G, while considering CMB-S4 forecast constraint we get $B_0 = 2.67 \times 10^{-6}$ G for the dark matter mass $\lesssim 10^{-2}$ GeV. Here, introduction of baryon-dark matter interaction relaxes the upper bound on B_0. We also discuss the bounds on $\hat{\sigma} - m_d$ by considering Planck 2018 upper bound on $B_0 \sim 10^{-9}$ G [26].

List of Acronyms

ΛCDM	Λ Cold Dark Matter
BBN	Big-Bang Nucleosynthesis
WMAP	Wilkinson Microwave Anisotropy Probe
COBE	COsmic Background Explorer
QCD	Quantum ChromoDynamic
EoR	Epoch of Reionization
IGM	InterGalactic Medium
JWST	James Webb Space Telescope
EDGES	Experiment to Detect the Global Epoch of Reionization Signature
ISM	InterStellar Medium
CMB	Cosmic Microwave Background
SIDM	Self-Interacting Dark Matter
WDM	Warm Dark Matter
THESEUS	Transient High Energy Sky and Early Universe Surveyor
NuSTAR	Nuclear Spectroscopic Telescope Array
CMBR	Cosmic Microwave Background Radiation
LIGO	Laser Interferometer Gravitational-Wave Observatory
PBH	Primordial Black Hole
AGN	Active Galactic Nuclei
LUX	Large Underground Xenon

PandaX	Particle and astrophysical Xenon
CRESST	Cryogenic Rare Event Search with Superconducting Thermometers
PICO	**PI**CASSO and **CO**UPP
PICASSO	Project in CAnada to Search for Super-symmetric Objects
FIRAS	Far Infrared Absolute Spectrophotometer
COUPP	Chicagoland Observatory for Underground Particle Physics
AMEGO	All-sky Medium Energy Gamma-ray Observatory
PMFs	Primordial Magnetic Fields
MHD	MagnetoHydroDynamics
ARCADE	Absolute Radiometer for Cosmology, Astrophysics and Diffuse Emission
LWA	Long Wavelength Array
HESS	High Energy Stereoscopic System

Contents

Declaration iii

Certificate v

List of publications included in the thesis vii

List of publications not included in the thesis ix

Acknowledgement xvii

Synopsis xxi

List of Acronyms xxix

List of Figures xxxv

List of Tables xlv

1 Introduction 1

1.1 Evolution of our Universe 3
1.1.1 Big-Bang nucleosynthesis 5
1.1.2 Recombination and photon decoupling 7
1.1.3 Through the dark ages to the present day . . 8
1.2 21 cm line as a probe during end of darkness 9
1.2.1 21 cm differential brightness temperature . . . 12
1.2.2 Evolution of the global 21 cm signal 15
1.3 21 cm line as a probe of new physics 17
1.3.1 Sterile neutrino dark matter — Chapter 2 . . 20
1.3.2 Primordial black hole dark matter — Chapter 3 20
1.3.3 Primordial magnetic fields — Chapter 4 & 5 . 21

2 Sterile Neutrino Dark Matter 23
2.1 Sterile neutrinos as dark matter 25
2.2 Existing bounds on sterile neutrinos 28
2.3 Radiative decay of sterile neutrinos 29
2.4 Impact on the thermal and ionization history 30
2.5 Bounds on the sterile neutrinos 33
2.6 Summary 40
2.7 Additional study 41
2.7.1 Bounds in light of varying T_{21} and redshift . . 41

3 Primordial Black Hole Dark Matter 45
3.1 Primordial black holes as dark matter 47

3.1.1 Signature of Primordial Black Holes 48
3.2 Existing bounds on Primordial Black Holes 49
3.3 Impact on the thermal and ionization history 49
3.4 Results and Discussion 52
3.5 Conclusions 59
3.6 Additional study 60
3.6.1 Bounds in light of varying T_{21} and redshift . . 60

4 PMFs & Excess Radio Background 63
4.1 Generation of primordial magnetic fields 64
4.2 Existing bounds on primordial magnetic fields 66
4.3 Evolution of PMFs after recombination 66
4.4 Background excess radio radiation 67
4.4.1 Excess radiation during the cosmic dawn . . . 69
4.4.2 Phenomenological model for excess radiation . 70
4.5 Impact on the thermal and ionization history due to primordial magnetic fields 71
4.6 Impact on the thermal and ionization history due to background radiation 73
4.7 Result and discussion 74
4.8 Conclusions 87

5 PMFs & Baryon-Dark matter Interaction 89

5.1 Baryon-dark matter interaction in presence of magnetic fields 91
5.2 Results and Discussion 93
5.2.1 Correlation between dark matter mass and baryon-dark matter cross section 96
5.2.2 Effect of primordial magnetic fields on the global 21 cm signal 99
5.3 Conclusions 101

6 Summary and Future outlook **103**
6.1 Summary 103
6.1.1 Bounds on dark matter candidates 105
6.1.2 Primordial Magnetic Fields 107
6.2 Future work 108

A Appendix **111**
A.1 Spin temperature of hydrogen 111
A.2 Emergent brightness temperature 113
A.3 Optical depth of hydrogen medium 113

References **117**

List of Figures

1.1 The graphic represents the evolution of precision cosmology over three decades— comparison between CMB temperature maps reported by each satellite. Left to right: Cosmic Background Explorer (COBE)[a]— launched in 1989, WMAP— launched in 2001 and Planck— launched in 2009. *Image credits: NASA/JPL-Caltech/ESA, https://www.nasa.gov/mission_pages/planck*. 2

1.2 The evolution of the Universe from it's beginning. *Image credits: European Space Agency (ESA)*[b]. 3

1.3 A schematic diagram for hyperfine transition in ground state of neutral hydrogen atom. 10

1.4 A schematic diagram for the change in brightness temperature of a light when it passes through a medium. 12

1.5 The figures represents the evolution of fluctuation in the 21 cm signal (above) and global 21 cm signal (below) when the background radiation is CMBR[c]. *Image credits: Pritchard & Loeb, Rep. Prog. Phys., 75, 086901, (2012)* [3, 31]. 16

1.6 The CMB observations can only probe the thin outer shell ($z \sim 1100$), and the observation of large scale structures can probe a small fraction of volume near the centre. We expect that the future advanced technology for the 21 cm signal observation will be able to probe the entire pink region. In the thesis, we focus on the 21 cm signal from the redshift 30 to 15. *Image credits: With the permission of Josh Dillon* [32]; *originally reproduced from Tegmark & Zaldarriaga (2009)* [33]. 18

2.1 The gas temperature evolution with redshift in the presence of decaying sterile neutrinos. The red dashed line represents the CMB temperature evolution. The black solid line depicts the $T_{\rm gas}$ when there is no sterile neutrino decay. The shaded region corresponds to EDGES absorption signal, i.e. $15 \leq z \leq 20$. In these figures, we keep mass of sterile neutrino fix to 10 KeV and vary lifetime. In figure (2.1b), we plot evolution of 21 cm differential brightness temperature as a function of redshift for the cases represented in figure (2.1a). 34

2.2 The figure caption is same as in figure (2.1), except here, we consider τ_{ν_s} constant to 6×10^{26} sec and vary mass of sterile neutrino. . . . 35

2.3 The figure caption is same as in figure (2.1), except here, we keep $f_{\rm abs}(z, m_{\nu_s}) = 1/2$ and vary lifetime of sterile neutrino. 35

2.4 The figure represents lower projected bounds on the lifetime of sterile neutrinos as a function of mass of sterile neutrinos by keeping 21 cm differential brightness temperature, $T_{21} \simeq -150$ and -100 mK. The dotted (dashed) line represents the case when energy transfer from CMB photons to gas is included (excluded) [34]. . . . 38

2.5 The figure represents upper projected bounds on the mixing angle of sterile neutrinos with active neutrinos as a function of mass of sterile neutrinos by keeping 21 cm differential brightness temperature, $T_{21} \simeq -150$ and -100 mK. The dotted (dashed) line represents the case when energy transfer from CMB photons to gas is included (excluded) [34]. The shaded regions are excluded for corresponding observations. The x-ray constraint on mixing angle (cyan shaded region) has been taken from the Ref. [35]. The red shaded region depicts the upper bounds on $\sin^2(\theta)$ from NuSTAR observations [36, 37]. Here, we have also plotted the recently reported bounds (after publication of our article) on $\sin^2(\theta)$ by NuSTAR— represented by NuSTAR 22 [37] and by Swift-XRT— represented by Swift-XRT 22 [38]. The grey shaded region is excluded by XMM-Newton [39]. . 39

2.6 Plot (2.6a), shows lower projected bounds on the lifetime of sterile neutrinos as a function of mass, while plot (2.6b), shows upper projected bounds on the mixing angle of sterile neutrinos with active neutrinos as a function of mass of sterile neutrinos for varying 21 cm differential brightness temperature (T_{21}) at $z = 17$. In figure (2.6b), the shaded regions are excluded for corresponding observations. The cyan shaded region represents the x-ray constraint [35]. The red shaded region depicts the upper bounds on $\sin^2(\theta)$ from NuSTAR observations [36, 37]. Here, we have also included the recently reported bounds (after publication of our article) on $\sin^2(\theta)$ by NuSTAR— represented by NuSTAR 22 [37] and by Swift-XRT— represented by Swift-XRT 22 [38]. The grey shaded region is excluded by XMM-Newton [39]. 42

2.7 Plot (2.7a), shows lower projected bounds on the lifetime of sterile neutrinos, while plot (2.7b), shows upper projected bounds on the mixing angle of sterile neutrinos with active neutrinos by keeping T_{21} to -150 mK for different values of redshift. 43

2.8 Plot (2.7a), shows lower projected bounds on the lifetime of sterile neutrinos, while plot (2.7b), shows upper projected bounds on the mixing angle of sterile neutrinos with active neutrinos by keeping T_{21} such that it does not change more than a factor of 1/4 from the minimum possible amplitude based on ΛCDM model for corresponding values of redshift. 44

3.1 The gas temperature evolution with redshift for evaporating primordial black hole. The red dashed lines represent the CMB temperature evolution. The black dashed lines depicts the $T_{\rm gas}$ when there is no PBHs. The shaded region corresponds to the redshift $15 \leq z \leq 20$ (EDGES observed signal). In this figure, we consider PBHs mass and $f_{\rm PBH}$ to 1×10^{15} g and 10^{-7}, respectively, and vary the spin of PBHs. 53

3.2 The caption is the same as in Figure (3.1), except here, we keep $M_{\rm PBH} = 1 \times 10^{15}$ g and $a_* = 0.5$ constant and vary $f_{\rm PBH}$. 53

3.3 The caption is the same as in Figure (3.1), except here, we vary the mass of PBHs and keep spin and $f_{\rm PBH}$ to 0.5 and 10^{-7}, respectively. 54

3.4 56

3.4 The projected upper bounds on the dark fraction of matter in the form PBHs ($f_{\rm PBH} = \Omega_{\rm PBH}/\Omega_{\rm DM}$) as a function of PBHs mass for different values of a_*. The shaded regions are excluded from our analysis for $f_{\rm PBH}$ when $a_* = 0$ (dotted black line), 0.5 (dot-dashed black line), 0.9 (dashed black line) and 0.9999 (solid black line). The dashed blue curve depicts the upper constraint on $f_{\rm PBH}$ by observations of the diffuse Isotropic Gamma-Ray Background (IGRB) for $a_* = 0.9$ [40]. The double-dot-dashed blue curve represents the upper constraint on $f_{\rm PBH}$ from Diffuse Supernova Neutrino Background (DSNB) searches at Super-Kamiokande, while the solid blue line represents the INTErnational Gamma-Ray Astrophysical Laboratory (INTEGRAL) observation of 511 KeV γ-ray lines at Galactic centre constraint on $f_{\rm PBH}$ for $a_* = 0.9$ [41]. The double-dot-dashed magenta (red) line represents the AMEGO forecast for $a_* = 0$ ($a_* = 0.9999$) [42]. Near future, AMEGO collaboration will be able to probe the parameter-space above the magenta (red) double-dot-dashed curve for $a_* = 0$ ($a_* = 0.9999$). The solid green line stands for 95% confidence level bound from INTEGRAL observation of Galactic gamma-ray flux for non-spinning PBHs [43]. Solid cyan curve depicts the upper bound from observing the 511 KeV γ-ray lines at the Galactic centre by assuming all the PBHs within a 3 Kpc radius of the Galactic centre for non-spinning PBHs [44]. The magenta solid line represents the Planck constraint [45]. The red solid line depicts the dwarf galaxy Leo T constraint [46] and the green dashed line shows the COMPTEL bound [47] for non-spinning PBHs. 57

3.5 The plots represent the upper projected bounds on the fraction of dark matter in the form of primordial black holes ($f_{\rm PBH}$) as a function of mass of PBHs ($M_{\rm PBH}$) for varying 21 cm differential brightness temperature (T_{21}) at $z = 17$. Figure (3.5c) represents the case when spin of PBHs: $a_* = 0$, while, figure (3.5d) represents the case with $a_* = 0.9$ 60

3.6 Figure (3.6a) represents upper projected bounds on $f_{\rm PBH}$ when $T_{21} \simeq -150$ mK for different values of redshift (z). Figure (3.6b) represents upper bounds on $f_{\rm PBH}$ when T_{21} does not change more than a factor of 1/4 from the minimum possible amplitude based on ΛCDM model for corresponding values of redshift ($T_{21}^{\rm Min}(z = 15) \simeq -238$ mK, $T_{21}^{\rm Min}(z = 17) \simeq -221.2$ mK and $T_{21}^{\rm Min}(z = 19) \simeq -207$ mK). Here, the cosmological parameters are: $h = 0.674$, $\Omega_{\rm M} = 0.315$, $\Omega_{\rm b} = 0.049$ [48]. Both figures obtained for $a_* = 0$. . . . 61

4.1 The gas temperature evolution with redshift. The solid blue lines represent the case when there is no x-ray, VDKZ18 or magnetic heating. VDKZ18 corresponds to the heat transfer from the background radiation to gas mediated by Lyα. The shaded region represents the EDGES observation redshift range, $15 \leq z \leq 20$. In this figure, we consider only VDKZ18 and x-ray heating with excess radiation (A_r). 75

4.2 The caption is same as in figure (4.1), except here, we include different combination of VDKZ18, x-ray and magnetic heating, and spectral index is fixed to -2.99 76

4.3 The caption is same as in figure (4.1), except here, we vary the spectral index and plot magnetic heating of the gas. 76

4.4 This figure shows the gas (solid lines) and spin (dashed lines) temperature evolution, The shaded region corresponds to the redshift $15 \leq z \leq 20$ — the redshift range for EDGES reported signal. . . . 80

4.5 This figure shows the 21 cm differential brightness temperature with redshift for same cases in plot (4.4). 80

4.6 In this figure, we study upper bounds on present-day magnetic field strength (B_0) with excess radiation fraction (A_r) for different values of the spectral index, n_B. The green-yellow and red-grey colour schemes represent the cases when $T_{21}|_{z=17.2} \simeq -500$ mK and -300 mK, respectively. For $T_{21}|_{z=17.2} \simeq -300$ mK case the value of n_B written with blue coloured text , while for -500 mK case it is written with black coloured text. Here, we consider $T_{\rm S} \simeq T_{\rm gas}$ and do not take into account the x-ray and VDKZ18 effects. 81

4.7 The caption is same as in figure (4.6), except here, we consider the effects of VDKZ18 and x-ray heating on the gas due to first stars after $z \lesssim 35$ and consider finite Lyα coupling. 82

4.8 In this figure, we study upper bounds on the present-day magnetic field strength (B_0) with spectral index (n_B) for different values of excess radiation fraction (A_r). The green-yellow and red-grey colour schemes represent the cases when $T_{21}|_{z=17.2} \simeq -500$ mK and -300 mK, respectively. For $T_{21}|_{z=17.2} \simeq -300$ mK case the value of n_B written with blue coloured text , while for -500 mK case it is written with black coloured text. The red dashed line depicts the Planck 2015 upper constraint on the present-day magnetic field strength [49, 50]. Here, we consider $T_{\rm S} \simeq T_{\rm gas}$ and do not take into account the x-ray and VDKZ18 effects. 85

4.9 The caption is same as in figure (4.8), except here, we consider the heating effects of VDKZ18 and x-ray on IGM gas due to first stars after $z \lesssim 35$ and consider finite Lyα coupling. The colour-bars are common for both plots. 86

5.1 This figure shows the temperature evolutions of baryon and dark matter in the presence of PMFs and baryon-dark matter interaction. Blue line corresponds to temperature evolution of gas in the absence of both magnetic heating and baryon-dark matter interaction. The red (green) solid lines represents the variation of the gas temperature and the dotted red (green) line shows the variation of the dark matter temperature in presence of PMFs and the baryon-dark matter interaction. In this plot we vary the strength of PMFs, and keep $\hat{\sigma}$ & dark matter mass constant to 10^{-41} cm^2 & 10^{-1} GeV, respectively. In all figures, notation for the mass of dark matter is written with m_d. While in the text, it is written as $M_{\rm DM}$. 94

5.2 The caption is same as in figure (5.1), except here, we only vary the strength of baryon-dark matter cross-section, and keep B_0 & dark matter mass constant to 10^{-6} G & 10^{-1} GeV, respectively. 95

5.3 The caption is same as in figure (5.1), except here, we only vary the dark matter mass, and keep B_0 & $\hat{\sigma}$ constant to 10^{-6} G & 10^{-41} cm^2, respectively. 95

5.4 The figure shows the minimal cross-section required to get $T_{21} \simeq -500$ mK (solid lines) and $T_{21} \simeq -300$ mK (dashed line) at $z = 17$ as a function of mass for different strengths of PMFs. Here, we assume no x-ray heating of gas, and spin temperature is completely coupled to gas temperature, i.e. $T_{\rm gas} \simeq T_S$. The solid (dashed) magenta, black, blue and red line correspond to $B_0 = 3.48 \times 10^{-6}$ G, 2.67×10^{-6} G, 10^{-6} G and 10^{-9} G respectively. The CMB-S4 (forecast) and Planck 2015 constraints on $\hat{\sigma}$ and $M_{\rm DM}$ with 95% C.L. have been taken from the Refs. [51, 52]. The green and gold regions are excluded by Planck 2015 and CMB-S4 forecast respectively. (1 GeV$^{-2} = 3.89 \times 10^{-28}$ cm^2) 97

5.5 21 cm differential brightness temperature (assuming infinite Lyα coupling) vs redshift when their is no x-ray heating. The dotted black (orange) colour represents standard ΛCDM (EDGES) predictions for the global T_{21} signal. Green, red and blue solid curves correspond to $B_0 = 1 \times 10^{-6}$, 1.35×10^{-6} and 1.65×10^{-6} G respectively. Here, $M_{\rm DM} = 10^{-1}$ GeV and $\hat{\sigma} = 6.22 \times 10^{-15}$ GeV^{-2}. 99

5.6 T_{21} plot with redshift when x-ray heating and finite Lyα coupling are considered [51]. Black, blue, green and red solid curves correspond to $B_0 = 2 \times 10^{-6}$, 1×10^{-6}, 8×10^{-7} and 6×10^{-7} G respectively. The magenta dashed line is corresponds to the EDGES upper bound on T_{21} : -300 mK. The values of $M_{\rm DM}$ and $\hat{\sigma}$ are same as considered in figure (5.5). 100

List of Tables

1.1 Approximate time scale, redshift and temperature for various events in the Universe. *Table credit: Daniel Baumann, "Lecture notes on cosmology: Part III Mathematical Tripos."* 6

"It might seem limited to impose our human perception to try to deduce the grandest cosmic code. But we are the product of the universe and I think it can be argued that the entire cosmic code is imprinted in us. Just as our genes carry the memory of our biological ancestors, our logic carries the memory of our cosmological ancestry. We are not just imposing human-centric notions on a cosmos independent of us. We are progeny of the cosmos and our ability to understand it is an inheritance."

Janna Levin, *How the Universe Got its Spots (2002)*

1

Introduction

In the 21st century, our knowledge of the Universe has proliferated— thanks to the tremendous progress of observational instruments in the last three decades. Especially the precision cosmology has grown remarkably in the past three decades as a result of an ample amount of high-quality Cosmic Microwave Background (CMB) data, in addition to the data and comprehensive studies of supernovae, stars and nearby galaxies. It is the greatest triumph of precision cosmology that we now know the age of our Universe, and it is only the tip of the iceberg. As another example, we know that observable/baryonic matter in the Universe is only about 5 percent and the leftover energy component consists the dark matter ($\sim$ 26 percent) and dark energy ($\sim$ 69 percent) based on the ΛCDM model of cosmology— the standard model of cosmology [48]. Here, Λ represents the dark energy, and CDM represents the cold dark matter. The ΛCDM model, together with the cosmo-

[a] http://lambda.gsfc.nasa.gov/product/cobe/

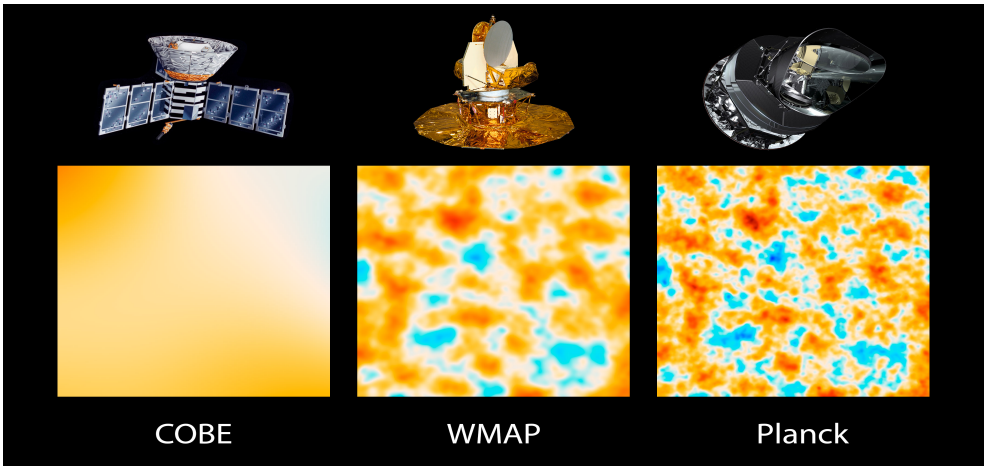

Figure 1.1: The graphic represents the evolution of precision cosmology over three decades— comparison between CMB temperature maps reported by each satellite. Left to right: Cosmic Background Explorer (COBE)[a]— launched in 1989, WMAP— launched in 2001 and Planck— launched in 2009. *Image credits: NASA/JPL-Caltech/ESA, https://www.nasa.gov/mission_pages/planck.*

logical inflation, can provide a complete picture of the evolution of our Universe from the beginning. The CMB data from Wilkinson Microwave Anisotropy Probe (WMAP)[b] played a crucial role in establishing the ΛCDM model. It is also supported by the Planck[c] observations [48, 53]. The ΛCDM model is widely accepted now, and there are various good reasons to believe this model: N-body simulations of structure formation based on the ΛCDM framework can explain the observed large scale structure of the Universe [54], it can also explain the CMB anisotropies & polarization [48, 53, 55–57] and accelerating expansion of the Universe caused by cosmological constant Λ [48, 58, 59][d]. In addition to this, the predictions for the helium and deuterium fractions by the standard Big-Bang Nucleosynthesis (BBN) for ΛCDM cosmology agree very well with observations.

[b] https://map.gsfc.nasa.gov/

[c] https://www.esa.int/Science_Exploration/Space_Science/Planck

[d] Saul Perlmutter with Brian P. Schmidt and Adam G. Riess received the Nobel Prize in Physics for 2011 "for the discovery of the accelerating expansion of the Universe through observations of distant supernovae."

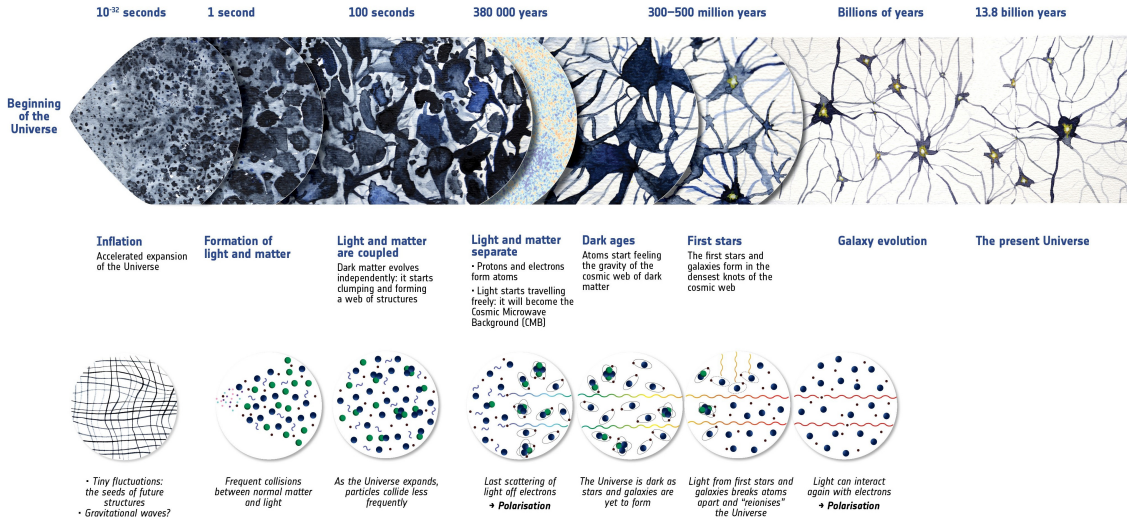

Figure 1.2: The evolution of the Universe from it's beginning. *Image credits: European Space Agency (ESA)*[e].

1.1 Evolution of our Universe

Before going into 21 cm cosmology, we briefly review cosmic history from the beginning of our Universe to the present day. The figure (1.2), shows a schematic picture of the evolution of our Universe from the beginning. The best current widely agreed model of the origin and evolution of our Universe is the Big-Bang model. According to this model, our Universe came into existence with a Big-Bang about 13.8 billion years ago [48]. Observations of CMB also support this theory [48, 60][f]. According to our best present-day understanding, the early Universe had an exponential expansion after the Big-Bang— it is known as the inflationary epoch[g] [61, 62]. There are several reasons to believe the inflation model: It can solve the three technical problems of the Big-Bang model— the horizon problem, flatness problem and the magnetic monopole problem [61, 62]:

[e] https://www.esa.int/

[f] Results from the COBE were honoured with the Nobel Prize in Physics 2006.

[g] Alan H. Guth, Andrei D. Linde and Alexei A. Starobinsky received 2014 KAVLI prize in Astrophysics "for pioneering the theory of cosmic inflation."

- The Big-Bang model fails to explain why causally disconnected regions appear homogeneous. The observation shows that the CMB temperature is uniform up to a scale of $\Delta T/T \approx 10^{-5}$ even when observed in opposite directions. Here, ΔT is the temperature difference between the two regions of the sky, and T is the average temperature over the whole sky. Assuming the standard Big-Bang model, opposite directions were so far separated that they always have been acausal. Then, why does CMB appear so uniform? It is known as the horizon problem.

- The second one is the flatness problem: The present-day total energy density of the Universe is equal to the critical energy density of the Universe. Any departure from the critical density will result in the curvature of the Universe. The observation shows dimensionless curvature energy density of the Universe $\Omega_k = 0.001 \pm 0.002$ [48]. It implies a flat Universe. A slight deviation of total energy density from critical energy density would have resulted in extreme effects on the flatness of the Universe over the cosmic time. Therefore, a flat universe like ours requires extreme fine-tuning conditions in the beginning. It is known as the flatness problem.

- The Grand Unified Theories (GUT) predict the existence of magnetic monopoles as at a very high temperature as the electromagnetic, weak and strong forces are not fundamental forces. Therefore, there can exist many stable magnetic monopoles in the Universe. No monopoles have been observed yet. It is known as the monopole problem.

These problems of the Big-Bang model can be circumvented by introducing the cosmic inflation model [61, 62]. Additionally, the inflation can give an idea of the origin of the observed structures in the Universe. The quantum fluctuations, prior to inflation, embedded in the initial energy density might have grown to astronomical scales over the cosmic time. Later, the dense regions might have condensed into structures like stars, galaxies and clusters of galaxies. The inflation epoch ends

when inflation potential steepens, and the inflation field acquires kinetic energy. Then inflation sector energy creates the standard model particles. This process is known as reheating. As the Universe expands continuously, it cools down. Then, Baryogenesis (excess of baryons over antibaryons)[h], electroweak phase transition (100 GeV) and QCD phase transition (150 MeV) takes place. The table (1.1), represents the time scale, redshift and temperature for various events in the Universe. The decoupling and freeze-out of various species can be understood by comparing the rate of interaction (Γ) and Hubble expansion (H). If $t_\Gamma \ll t_H$, then particle interactions dominates over expansion. Here, $t_* \equiv 1/*$ is the time scale for corresponding rate ($* \equiv \Gamma$ or H). Therefore, local thermal equilibrium can be reached. As Universe cools down, the value of t_Γ increases faster than t_H. At $t_\Gamma \sim t_H$ particles starts to decouple from thermal equilibrium. Different species decouple at different times as t_Γ varies from species to species. If the mass (m) of particles becomes larger than their temperature (T), the distribution function is exponentially suppressed, $\propto e^{-m/T}$ and particles freeze out. For example, the cross-section for weak interaction is $\sigma \sim G_F^2 T^2$; $G_F = 1.17 \times 10^{-5}$ GeV^{-2} is Fermi constant. It implies $\Gamma/H \sim (T/\text{MeV})^3$. For example, the neutrinos interact through weak interaction only and they decouple around $T \sim 1$ MeV from primordial plasma.

1.1.1 Big-Bang nucleosynthesis

When plasma cools down below $\sim$ 100 KeV, around three minutes after the beginning of the Universe, Big-Bang nucleosynthesis takes place. In this phase, light elements were formed. The neutrons and protons start to form deuterium via the process,

$$n + p \leftrightarrow D + \gamma\,. \tag{1.1}$$

[h]The exact time and mechanism for Baryogenesis are not exactly known yet.

Event	time	redshift	Temperature
Inflation	10^{-36} sec	-	-
Baryogenesis	?	?	?
Electroweak phase transition	20 ps	10^{15}	100 GeV
QCD phase transition	20 μs	10^{12}	150 MeV
Dark matter freeze-out	?	?	?
Neutrino Decoupling	1 sec	6×10^9	1 MeV
Electron-positron annihilation	6 sec	2×10^9	500 KeV
Big-Bang nucleosynthesis	3 minute	4×10^8	100 KeV
Matter-radiation equality	60 Kyr	3400	0.75 eV
Recombination	$260-380$ Kyr	$1400 - 1100$	$0.33 - 0.26$ eV
Photon decoupling	~ 380 Kyr	~ 1100	~ 0.27 eV
First stars formation	~ 100 Myr	~ 30	~ 7 meV
Reionization	~ 400 Myr	~ 11	~ 2.6 meV
Dark energy-matter equality	9 Gyr	0.4	0.33 meV
Present	13.8 Gyr	0	0.24 meV

Table 1.1: Approximate time scale, redshift and temperature for various events in the Universe. *Table credit: Daniel Baumann, "Lecture notes on cosmology: Part III Mathematical Tripos."*

Now, these formed nuclei can form the heavier nuclei via the process,

$$D + p \leftrightarrow \mathrm{He}^3 + \gamma \qquad \text{and} \qquad D + \mathrm{He}^3 \leftrightarrow \mathrm{He}^4 + p\,. \tag{1.2}$$

The number density ratio of these elements can be found easily. For example: in equation (1.1), $\mu_n + \mu_p = \mu_D$ as $\mu_\gamma = 0$. Here, μ is the chemical potential for the corresponding species. It implies the number densities ratio to be,

$$\left[\frac{n_D}{n_n\, n_p}\right]_{\mathrm{eq}} = \frac{3}{4}\left[\frac{m_D}{m_n\, m_p}\,\frac{2\,\pi}{T}\right]^{3/2} e^{-(m_D - m_n - m_p)/T}\,, \tag{1.3}$$

here, T is the plasma temperature. m_D, m_n and m_p are masses of deuterium, neutron and proton, respectively.

1.1.2 Recombination and photon decoupling

Within the ΛCDM cosmology, free electrons and protons cool sufficiently after $\sim 3 \times 10^5$ years of Big-Bang to form neutral hydrogen atoms. Recombination occurs around redshift 1100. During this epoch, electrons and protons combine to form hydrogen atoms via the process,

$$e^- + p \leftrightarrow \mathrm{H} + \gamma\,. \tag{1.4}$$

When the plasma temperature was above 1 eV, there were still free electrons and protons in the plasma. Photons remain tightly coupled to electrons due to Compton scattering, and electrons were coupled to protons due to Coulomb scattering. In turn, there was only a small density of neutral hydrogen atoms. When the plasma temperature decreased sufficiently, electrons and protons combined and formed hydrogen atoms. Subsequently, the free electron density fell rapidly. As the number density of free electrons decreased adequately, the mean free path of photons increased sharply; and photons decoupled from plasma. As discussed in

the end of section (1.1), one can estimate the photon decoupling redshift by relation, $t_{\Gamma_\gamma}(z_{\rm dec}) \sim H(z_{\rm dec})$. Here, $\Gamma_\gamma(z_{\rm dec}) = n_e(z_{\rm dec})\,\sigma_T$ is the photon interaction rate or photon mean free path at the time of decoupling, $z_{\rm dec}$ is the redshift of photon decoupling from plasma and σ_T is Thomson cross-section. The electron number density (n_e) can be found by using the Saha equation for the process in equation (1.4). After solving the relation, we can find $z_{\rm dec} \sim 1100$ or corresponding time to 380,000 yr after Big-Bang. We can also estimate that the free electron fraction in the plasma remains only about one percent— the plasma becomes mostly transparent for photons. This time is known as the surface of last-scattering. After decoupling, these photons stream freely and are known as CMB radiation (CMBR).

1.1.3 Through the dark ages to the present day

After photon decoupling from baryonic matter, there were no luminous objects— this epoch is known as the dark ages. The Universe was predominantly neutral during this era. This period of darkness ensued until the first luminous object was not formed in the Universe for about a hundred million years after the Big-Bang. During this era, overdensity was growing in the dark matter perturbations already. Later, these overdensities reached a critical value and collapsed to form dark matter halos— a gravitationally bound structure [63]. The first generation of luminous objects sprung up around redshift 30 inside dark matter halos— this period is known as the Cosmic Dawn. As of now, it is not clear that these objects were either quasars or stars. As the first stars formed in very different circumstances, they probably were very different from our nearby stars. After the formation of the first luminous objects, their radiation start to ionize the gas in the Universe. This era is known as the epoch of reionization (EoR). Three-year WMAP observations of CMB suggest that reionization starts around redshift 11 and ends by ~ 7 [56]. Planck observations suggest instantaneous reionization with mid-point

redshift of reionization 7.68 ± 0.79 [48]. Supernovae observations suggest that the Universe enters into an accelerated expansion phase around redshift ~ 0.5 [59]. This accelerating expansion can not be explained only by matter in the Universe. To explain, one requires the existence of dark energy [59, 64]. Then, we reach the present-day after 13.8 billion years from the Big-Bang.

The first complexity in the physics, after the dark ages, emerged with the event of the formation of the first luminous objects. As of now, this era is not observed due to the lack of our instrumental capability. The recently launched James Webb Space Telescope (JWST)[i] will be able to probe the Universe back to redshift ~ 20. One of the best pre-eminent and promising methods to probe the cosmic dawn era is the observation of the redshifted radiation from the hyperfine transition in the ground state of the neutral hydrogen atom. The low-frequency radio telescopes, sensitive to a frequency of as low as 40 MHz, can help to explore this era.

1.2 21 cm line as a probe during end of darkness

The 21 cm signal appears to be a treasure trove to provide an insight into the period when the first luminous objects were formed; hereafter we will refer these objects as first stars. The 21 cm line has been actively used to trace the neutral hydrogen in Milky Way for more than seven decades since its first observation in 1951 [1]. It was first suggested by H. C. van de Hulst in 1945 that a 21 cm line might be observable in the galactic radiation spectrum [65]. However, probing the neutral hydrogen during and pre cosmic dawn via the 21 cm signal is different. These periods are observed in the form of absorption/emission by the neutral hydrogen medium relative to the CMBR or background radiation at a reference wavelength of 21 cm. It is referred as the 21 cm differential brightness temperature— we will discuss it later.

The 21 cm line corresponds to the wavelength for hyperfine transition between

[i] https://jwst.nasa.gov/

1S singlet and triplet states of the neutral hydrogen atom. The corresponding frequency for the 21 cm line is 1420.4 MHz. For a transition at redshift z, the frequency can be mapped for a present-day observed frequency as $1420.4/(1+z)$. Hydrogen is the dominating fraction in the Inter-Galactic-Medium (IGM) during cosmic dawn. Therefore, it is convenient and advantageous to study IGM using the 21 cm signal. The transition probability for the hyperfine state is once in $\sim 10^7$ years in the absence of any external sources. The presence of any exotic source of energy can significantly affect the hyperfine transition, thus spin temperature of the hydrogen gas. The spin temperature (T_S) is characterized by the number density ratio in 1S singlet and triplet states of the neutral hydrogen atom,

$$\frac{n_{\rm T}}{n_{\rm S}} = \frac{g_{\rm T}}{g_{\rm S}} \times \exp\left[-\frac{2\pi\nu_{\rm TS}}{T_S}\right], \ \nu_{\rm TS} = 1420.4 \text{ MHz} \simeq 1/(21 \text{ cm}) \,, \tag{1.5}$$

here, $n_{\rm T}$ and $n_{\rm S}$ are the population of triplet and singlet states, respectively. Hyperfine splitting suppresses the singlet and lifts the triplet state. $g_{\rm T} = 3$ and $g_{\rm S} = 1$ are the statistical or spin degeneracies of triplet and singlet states, respectively. In the cosmological scenarios, there are three processes that can affect the spin temperature: background radio radiation, Lyα radiation from the first stars and

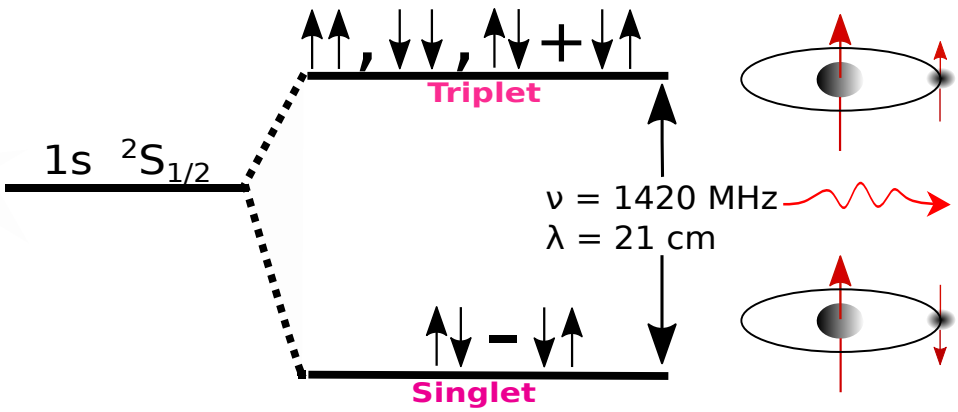

Figure 1.3: A schematic diagram for hyperfine transition in ground state of neutral hydrogen atom.

collisions of a hydrogen atom with another hydrogen atoms, residual electrons or protons. In the presence of all these three effect, we can write the rate of change in the population density of singlet state,

$$\frac{dn_{\rm S}}{dt} = -n_{\rm S}(P^{\rm R}_{\rm ST} + P^{\alpha}_{\rm ST} + P^{\rm C}_{\rm ST}) + n_{\rm T}(P^{\rm R}_{\rm TS} + P^{\alpha}_{\rm TS} + P^{\rm C}_{\rm TS})\,, \tag{1.6}$$

here, $P_{\rm ST}$ and $P_{\rm TS}$ are excitation and de-excitation coefficients, respectively. R, α and C superscripts represent the excitation/de-excitation due to background radio radiation[j], Lyα radiation from first stars and collisions, respectively. In the detailed balance between the population of 1S singlet and triplet states, by solving the equation (1.6)— see appendix A.1, one can find the spin temperature as [2, 3],

$$T_{\rm S}^{-1} = \frac{T_{\rm R}^{-1} + x_\alpha\, T_\alpha^{-1} + x_c\, T_{\rm gas}^{-1}}{1 + x_\alpha + x_c}\,, \tag{1.7}$$

here, T_α and $T_{\rm R}$ is the colour temperature of Lyα radiation from first stars and background radio radiation temperature, respectively. $T_{\rm gas}$ is the gas temperature. It refers to the temperature of either neutral species, ions, electrons or protons— all remain in thermal equilibrium. Before the first luminous objects formation, there was no Lyα radiation implying x_α & $T_\alpha = 0$. After the first luminous objects formation, their Lyα photons started repeatedly scatter with the gas, and brought the Lyα radiation into a local thermal equilibrium with the gas. Therefore, during the cosmic dawn era the colour temperature can be taken as gas temperature, $T_\alpha \simeq T_{\rm gas}$ [2, 3, 66]. $x_\alpha = P^{\alpha}_{\rm TS}/P^{\rm R}_{\rm TS}$ is the Lyα coupling coefficient due to Wouthuysen-Field effect [2, 4]. Here, $P^{\rm R}_{\rm TS} = (1 + T_R/T_{\rm TS})\, A_{10}$, $T_{\rm TS} = 2\,\pi\,\nu_{\rm TS} = 0.068$ K and $A_{10} = 2.85 \times 10^{-15}$ sec^{-1} is the Einstein coefficient for spontaneous emission from triplet to singlet state. For the all presented scenarios in the thesis: $T_{\rm R} \gtrsim 49$ K $\gg T_{\rm TS}$ at required redshift $z \sim 17$. Thus, one can approximate $P^{\rm R}_{\rm TS} \simeq A_{10} \times (T_R/T_{\rm TS})$. $P^{\alpha}_{\rm TS} = 4\,P_\alpha/27$ and P_α is the rate of scattering of Lyα photons [3]. $x_c = P^{\rm C}_{\rm TS}/P^{\rm R}_{\rm TS}$

[j] $P^{\rm R}_{\rm TS}$ includes both the induced emission due to background radio radiation and spontaneous emission— equation (A.4).

is the collisional coupling coefficient due to scattering between hydrogen atoms or scattering of hydrogen atoms with other species such as electrons and protons. Hence, the Lyα and collisional coupling coefficients [3],

$$x_\alpha = \frac{P^\alpha_{\rm TS}}{P^{\rm R}_{\rm TS}} = \frac{4\,P_\alpha}{27\,A_{10}} \times \frac{T_{\rm TS}}{T_R}\,, \tag{1.8}$$

$$x_c = \frac{P^{\rm C}_{\rm TS}}{P^{\rm R}_{\rm TS}} = \frac{P^{\rm C}_{\rm TS}}{A_{10}} \times \frac{T_{\rm TS}}{T_R}\,. \tag{1.9}$$

Here, the de-excitation coefficient due to collisions in gas: $P^{\rm C}_{\rm TS} = n_{\rm HI}\,k^{\rm HH}_{10} + n_e\,k^{\rm He}_{10} + n_p\,k^{{\rm H}p}_{10}$. $n_{\rm HI}$, n_e and n_p are the number density of neutral hydrogen, electrons and protons in the medium, respectively. $k^{\rm HH}_{10}$ is the rate of scattering between hydrogen atoms. $k^{\rm He}_{10}$ is the rate of scattering between hydrogen atoms and electrons. $k^{{\rm H}p}_{10}$ is the rate of scattering between hydrogen atoms and protons. For a more detailed review, see the review article by Pritchard and Loeb [3].

1.2.1 21 cm differential brightness temperature

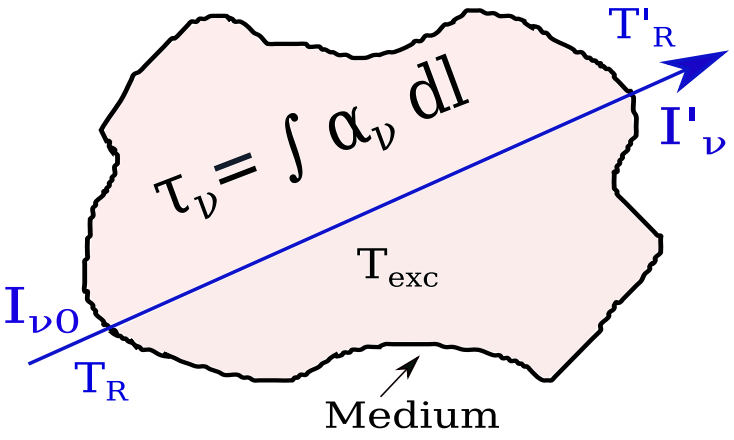

Figure 1.4: A schematic diagram for the change in brightness temperature of a light when it passes through a medium.

As discussed above, the 21 cm signal is observed in the form of differential brightness temperature during the cosmic dawn era. If a light with initial intensity ($I_{\nu 0}$) & brightness temperature ($T_{\rm R}$) passes through a medium having optical depth (τ_ν) & excitation temperature ($T_{\rm exc}$), there can be an absorption or emission by the medium resulting in a different final/emergent intensity (I'_ν) and brightness temperature ($T'_{\rm R}$). The divergence of the emergent brightness temperature ($T'_{\rm R}$) from the initial brightness temperature ($T_{\rm R}$) is known as the differential brightness temperature (observed temperature by antennas),

$$\delta T_B = T'_{\rm R} - T_{\rm R}\,. \tag{1.10}$$

In observation, we measure the specific intensity of radiation at some frequency. As discussed above, the initial frequency ν of light at redshift z changes with time due to the expansion of the Universe. For present-day, it will modify to $\nu/(1+z)$. Accordingly, the frequency of 1420.4 MHz of a light originated in the redshift range $z = 15 - 10$ will suppress to $\mathcal{O}(10^5$ Hz). While the CMB peak occurs around a frequency of $\mathcal{O}(10^8$ Hz)— this is much higher than the 21 cm line. Therefore, we can approximate the blackbody spectrum as the Rayleigh-Jeans limit. In this limit the observed specific intensity of radiation at a frequency ν,

$$I_\nu = \frac{4\,\pi\,\nu^3}{\exp(2\,\pi\,\nu/T) - 1} \quad \xrightarrow{2\pi\nu/T \ll 1} \quad I_\nu \equiv 2\,\nu^2\,T\,, \tag{1.11}$$

T is the brightness temperature of the blackbody. The emergent brightness temperature, $T'_{\rm R}$ in equation (1.10), is a combination of $T_{\rm R}$ and $T_{\rm exc}$. We can find $T'_{\rm R}$ by solving the equation of radiative transfer. If a light passes through a medium— figure (1.4), the change in its intensity (dI_ν) due to the absorption or emission with travelled distance (dl),

$$\frac{dI_\nu}{dl} = j_\nu - \alpha_\nu I_\nu\,, \tag{1.12}$$

where, j_ν is emission of light by spontaneous, stimulated emission, etc. α_ν is the absorption coefficient of medium at frequency ν. Here, we follow the review articles by Pritchard et al. [3] and Furlanetto et al. [67]. Writing equation (1.12) as,

$$\frac{dI_\nu}{d\tau_\nu} = S_\nu - I_\nu \,, \tag{1.13}$$

here, $d\tau_\nu = \alpha_\nu \, dl$ and $S_\nu = j_\nu/\alpha_\nu$. Therefore,

$$\tau_\nu = \int \alpha_\nu \; dl \,, \tag{1.14}$$

is the optical depth. Optical depth is a function of the absorption of light by the medium with travelled distance in the medium. By solving the equation (1.12) and using equation (1.11), we can find the $T'_{\rm R}$— see the appendix A.2,

$$T'_{\rm R} = T_{\rm exc}\,(1 - e^{-\tau_\nu}) + T_{\rm R}\, e^{-\tau_\nu} \,. \tag{1.15}$$

The differential brightness temperature, by equation (1.10), $\delta T_B = (T_{\rm exc} - T_{\rm R}) \times (1 - e^{-\tau_\nu})$. For the expending Universe, the temperature of radiation is $\propto (1 + z)$. Thus, the redshifted differential brightness temperature for present-day,

$$\delta T_B = \frac{T_{\rm exc} - T_{\rm R}}{1 + z} \times (1 - e^{-\tau_\nu}) \,. \tag{1.16}$$

In our case, the medium is hydrogen gas and the $T_{\rm exc}$ for the 21 cm line is $T_{\rm S}$— defined in equation (1.7). The τ_ν is $\ll 1$ for neutral hydrogen gas— optically thin. Hereafter, we will write δT_B as T_{21} for the 21 cm line. Therefore, the 21 cm differential brightness temperature [3],

$$T_{21} \simeq \frac{T_{\rm S} - T_{\rm R}}{1 + z} \times \tau_\nu \,. \tag{1.17}$$

The optical depth can be found by solving the equation (1.14) for a hydrogen

medium and a line profile— see appendix A.3,

$$\tau_\nu \simeq 27\, x_{\rm HI}\, (1+z) \left(\frac{\rm mK}{T_{\rm S}}\right) \left(\frac{0.15}{\Omega_{\rm m}\, h^2}\, \frac{1+z}{10}\right)^{1/2} \left(\frac{\Omega_{\rm b}\, h^2}{0.023}\right) , \tag{1.18}$$

here, $x_{\rm HI} = n_{\rm HI}/n_{\rm H}$ is the fraction of neutral hydrogen in the Universe, and $n_{\rm H}$ is the total number density of hydrogen. $\Omega_{\rm m} = \rho_{\rm M}/\rho_{\rm cr}$ and $\Omega_{\rm b} = \rho_{\rm b}/\rho_{\rm cr}$ are the dimensionless energy density parameters for total matter and baryons in the Universe, respectively. $\rho_{\rm M}$ and $\rho_{\rm b}$ are the energy density for total matter and baryons, respectively. $\rho_{\rm cr} = 3\, H^2/(8\,\pi\, G_{\rm N})$ is the critical energy density and $G_{\rm N}$ is the gravitational constant. $h = H_0/(100\ {\rm Km\ sec^{-1}\, Mpc^{-1}})$ and H_0 is the present-day value of Hubble parameter. Substituting the value of τ_ν from equation (1.18) into equation (1.17), we get the final expression for the global 21 cm differential brightness temperature [3, 68–71],

$$T_{21} \simeq 27\, x_{\rm HI} \left(1 - \frac{T_{\rm R}}{T_{\rm S}}\right) \left(\frac{0.15}{\Omega_{\rm m}\, h^2}\, \frac{1+z}{10}\right)^{1/2} \left(\frac{\Omega_{\rm b}\, h^2}{0.023}\right)\ {\rm mK}\,. \tag{1.19}$$

Depending on the ratio $T_{\rm R}/T_{\rm S}$, there can be three scenarios for 21 cm signal: If $T_S = T_R$ then $T_{21} = 0$ and there will not be any signal; for the case when $T_S > T_R$, emission spectra can be observed, and when $T_S < T_R$, it leaves an imprint of absorption spectra.

1.2.2 Evolution of the global 21 cm signal

Usually, in the ΛCDM model of cosmology, the contribution in the background radiation is assumed to be solely by the CMB radiation, $T_{\rm R} \equiv T_{\rm CMB}$; $T_{\rm CMB}$ is the CMBR temperature. Therefore, in this subsection, we discuss the evolution of the global 21 cm signal when only CMBR is present as background radiation.

At the end of recombination, the baryon number density of the Universe is dom-

[k] The position and amplitude of the second dip from the left (between redshift $30 - 15$) may modify depending on models of first-stars formation or x-ray heating of the gas.

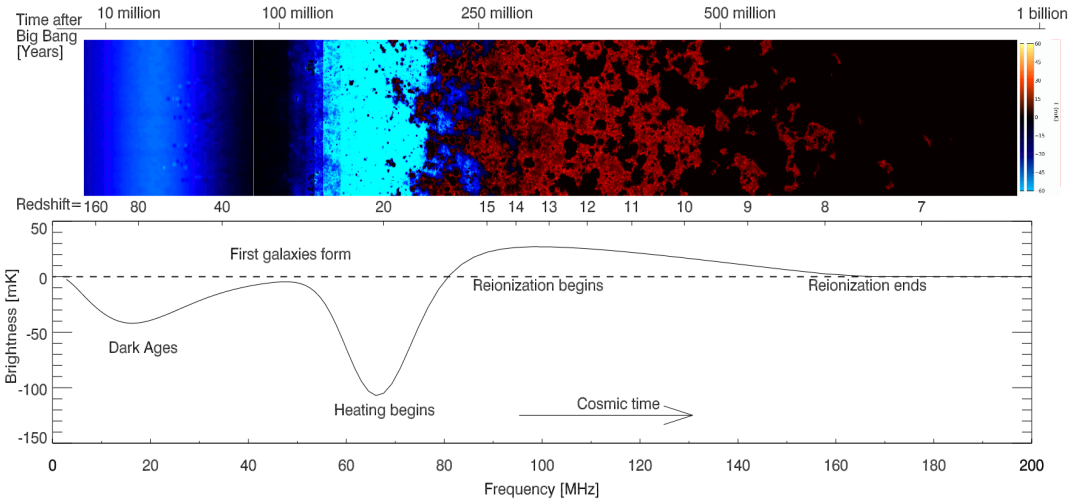

Figure 1.5: The figures represents the evolution of fluctuation in the 21 cm signal (above) and global 21 cm signal (below) when the background radiation is CMBR[k]. *Image credits: Pritchard & Loeb, Rep. Prog. Phys., 75, 086901, (2012)* [3, 31].

inated mainly by the neutral hydrogen, a small fraction of helium, residual free electrons and protons. After recombination ($z \sim 1100$) down to $z \sim 200$, the residual free electrons undergo Compton scattering and maintain thermal equilibrium between electrons and CMBR. The free electrons remain in thermal equilibrium with other gas components implying $T_{\rm gas} \sim T_{\rm CMB}$ [72]. Using equations (1.7) and (1.19), we can find that $T_{21} = 0$, and the 21 cm signal is not present during this era. From $z \sim 200$ until 40, the number density of free electrons decreases significantly and this makes the Compton scattering insufficient. As a result, the gas decouples from CMBR, and its temperature falls adiabatically: $T_{\rm gas} \propto (1+z)^2$. The gas temperature falls below CMBR implying an early 21 cm absorption signal— known as the collisional absorption signal [3]. During this period, collisions among the gas components dominate, i.e. $x_c \gg 1$, which implies $T_{\rm S} \sim T_{\rm gas}$ — equation (1.7). Nevertheless, this signal is not observed yet due to the poor sensitivity of present-day available radio antennas as the sensitivity of antennas falls dramatically below

$\sim$ 50 MHz. After $z \sim 40$ to the formation of the first star[l], number density and temperature of the gas are very small, hence, $x_c \to 0$. Therefore, $T_{21} \sim 0$ and no signal is present there [3, 73]. After the first star formation, gas temperature couples again to the spin temperature due to Lyα radiation emitted from the first stars by Wouthuysen-Field (WF) effect [2, 4, 66]. Therefore, $x_\alpha \gg 1, x_c$ and absorption spectra can be seen— equations (1.7 and 1.19). After $z \sim 15$, the gas temperature starts to rise due to x-ray radiation emitted from the first stars[m]. Consequently, the temperature of gas rises above CMB temperature and the emission spectra can be seen. As the reionization ends, neutral hydrogen fraction becomes very small and no signal is observed. The small fraction of neutral hydrogen were left only in dense regions of collapsed structures. These regions can be analysed by 21 cm forest— an analogy to Lyα forest.

1.3 21 cm line as a probe of new physics

As shown in the figure (1.6), the 21 cm signal can probe a large volume of the history of our Universe— pink region. Currently, we are not able to probe the high redshift Universe ($z \gtrsim 30$) as the sensitivity of presently available radio antennas becomes very low below $\sim$ 50 MHz. We expect that the future advanced technology for the 21 cm signal observation will be able to probe the Universe above the redshift 25. In the thesis, we focus on the 21 cm signal between the redshift range of 30 to 15.

After $z \sim 200$ gas temperature falls adiabatically and reaches to $\simeq 7$ K at $z = 17.2$, while the CMB temperature reaches to $\simeq 49.6$ K. From the equation (1.19), this implies a value of absorptional amplitude of T_{21} to ~ -220 mK in absence of any heating effects on the IGM gas due to first stars. Here, to calculate T_{21}, we have taken $x_{\rm HI}$ to unity. The $x_{\rm HI}$ can be written as $1 - x_e$. In our case, at

[l]The redshift of first stars formation is not well known and it could be around 35 to 25.

[m]It is also not very clear when x-ray heating begins to dominate the temperature of the gas. We use the fiducial models for x-ray heating considered in references [51, 74–76].

$z \sim 17$ the ionization fraction, $x_e \lesssim \mathcal{O}(10^{-3})$ implying $x_{\rm HI} \simeq 1$. Here, $x_e = n_e/n_{\rm H}$ is the ionization fraction and n_e is the number density of residual free electrons. The presence of any exotic source of energy can inject energy into IGM and heat the gas. This in turn can modify the absorption amplitude in the global 21 cm signal. This feature can provide a robust bound on the properties of such sources of energy injection into IGM. In the thesis, the following four works has been

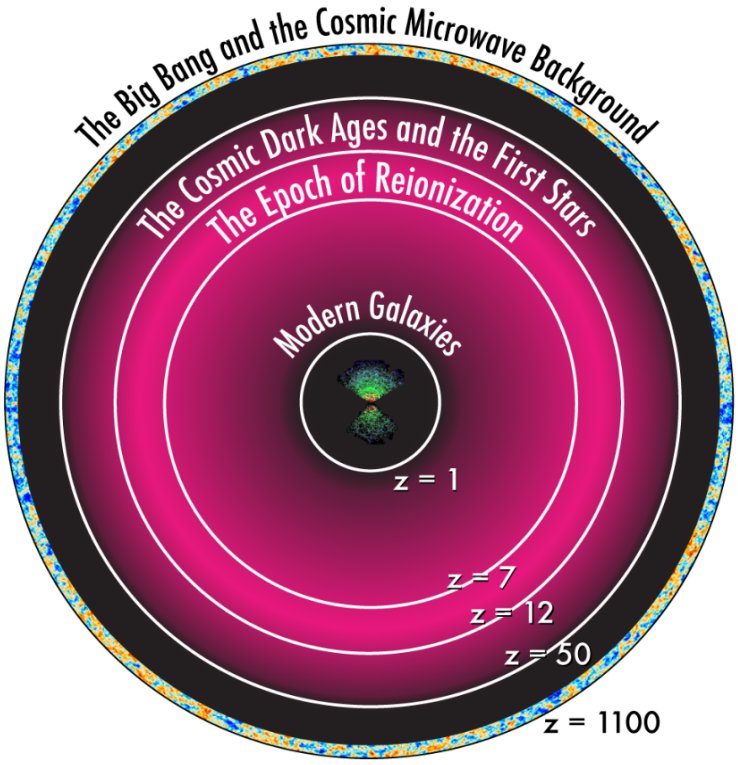

Figure 1.6: The CMB observations can only probe the thin outer shell ($z \sim 1100$), and the observation of large scale structures can probe a small fraction of volume near the centre. We expect that the future advanced technology for the 21 cm signal observation will be able to probe the entire pink region. In the thesis, we focus on the 21 cm signal from the redshift 30 to 15. *Image credits: With the permission of Josh Dillon* [32]; *originally reproduced from Tegmark & Zaldarriaga (2009)* [33].

considered: sterile neutrinos and primordial black holes as dark matter candidates and constrain their properties in the light of the global 21 cm signal. Another two works discussed in the thesis are related to the constraining strength of primordial magnetic fields that might have been generated in the early Universe.

In 2018, the Experiment to Detect the Global Epoch of Reionization Signature (EDGES)[n] collaboration reported an absorption profile for the 21 cm signal in the redshift range $15 - 20$ [5]. The EDGES collaboration reported T_{21} to be -500^{+200}_{-500} mK in the redshift range $15-20$ centred at 78 ± 1 MHz and in symmetric "U" shaped form. This absorption amplitude is nearly two times smaller than predicted by theoretical models based on ΛCDM framework (~ -220 mK). It is argued that to explain the EDGES observation, for the best fitting amplitude at the centre of the "U" profile, either the cosmic background radiation temperature $T_{\rm CMB} \gtrsim 104$ K for the standard $T_{\rm gas}$ evolution or $T_{\rm gas} \lesssim 3.2$ K in the absence of any non-standard evolution of the $T_{\rm CMB}$ [5]. Recently, many articles have questioned the EDGES measurement [6–8, 77, 78]. For example, in Ref. [77], the authors have questioned the fitting parameters for the foreground emission and data. There is a possibility that the absorption feature in the EDGES observation can be a ground screen artifact [7]. The absorption amplitude may modify depending on the modelling of the foreground [8, 78]. In a recent article [6], authors claimed that the EDGES observation might not be of an astrophysical origin. We revisit the EDGES observation and controversies over it in the chapter (6) also. In the light of these controversies, in the recent two articles (1.3.1 & 1.3.2), we do not consider the absorption amplitude reported by the EDGES collaboration. In these articles, we take 21 cm differential brightness temperature such that it does not change, from its standard theoretical value (~ -220 mK), by a factor of more than 1/4 (i.e. -150 mK) or 1/2 (i.e. -100 mK) at redshift 17.2. While in the older two articles (1.3.3), we have considered the absorption amplitude reported by the

[n] https://www.haystack.mit.edu/astronomy/astronomy-projects/edges-experiment-to-detect-the-global-eor-signature/

EDGES collaboration.

1.3.1 Sterile neutrino dark matter — Chapter 2

In the warm dark matter models, one of the theoretically well-motivated candidates is KeV mass sterile neutrinos. Sterile neutrinos are radiatively unstable and can inject photon energy into the IGM. The injection of energy into the IGM can modify the temperature and ionization history of the IGM gas thus absorption amplitude of 21 cm signal during cosmic dawn era. Therefore one can constraint the lifetime of sterile neutrinos and the mixing angle of sterile neutrinos with active neutrinos.

The article has been published as: Pravin Kumar Natwariya and Alekha C. Nayak, "Bounds on sterile neutrino lifetime and mixing angle with active neutrinos by global 21 cm signal", *Physics Letters B* 827 (2022) 136955.

1.3.2 Primordial black hole dark matter — Chapter 3

Primordial black holes (PBHs) have attracted much interest in recent years and have been a part of intense studies for more than five decades. As PBHs are massive, interact only gravitationally and are formed in the very early Universe, they can be considered as a potential candidate for non-particle dark matter. Hawking evaporation of PBHs can inject energy into the IGM and therefore be constrained by the absorption feature in the global 21 cm signal. The mass and spin are fundamental properties of a black hole, and they can substantially affect the evaporation rate of the black hole. In this work, we derive an upper bound on the dark matter fraction in the form of the primordial black holes with a non-zero spin.

The article has been published as: Pravin Kumar Natwariya, Alekha C. Nayak and Tripurari Srivastava, "Constraining spinning primordial black holes with global 21-cm signal", *Mon Not R Astron Soc* 510, 4236–4241 (2022).

1.3.3 Primordial magnetic fields — Chapter 4 & 5

Observations suggest that the magnetic fields (MFs) are ubiquitous in the Universe– from the length scale of planets and stars to the cluster of galaxies. The origin and evolution of PMFs are one of the outstanding problems of cosmology. Decaying PMFs can inject magnetic energy into thermal energy of the IGM and heat the gas. As briefly mentioned earlier, one requires to cool the IGM gas during cosmic dawn below the standard evolution or increase the radio background at required redshift to explain the EDGES observation. Here, we explore the upper bounds on the present-day strength of the PMFs in both the scenarios by considering different models. The articles have been published as:

- Pravin Kumar Natwariya, "Constraint on Primordial Magnetic Fields In the Light of ARCADE 2 and EDGES Observations", *Eur. Phys. J. C* 81 (2021) 5, 394.
- Jitesh R. Bhatt, Pravin Kumar Natwariya, Alekha C. Nayak and Arun Kumar Pandey, "Baryon-Dark matter interaction in presence of magnetic fields in light of EDGES signal", *Eur. Phys. J. C* 80 (2020) 4, 334.

Chapter 6 summarises the main results of the thesis. We also discuss possibilities of further extensions and future scopes of the results obtained in the thesis.

"Would you tell me, please, which way I ought to go from here?' 'That depends a good deal on where you want to get to,' said the Cat"

Lewis Carroll, *Alice in Wonderland*

"It is the nature of all greatness not to be exact"

Edmund Burke, *speech "On American Taxation"*

2

Sterile Neutrino Dark Matter

Despite the searching for decades, the nature of dark matter is still unknown. It is one of the biggest mysteries in particle physics and cosmology. Although ΛCDM model of cosmology is highly successful in explaining Big-Bang nucleosynthesis, CMB anisotropies and large scale structures of the Universe, it faces challenges at a smaller length scale, $\lesssim 1$ Mpc (for a detailed review see [79] and references therein). These problems include the missing satellite or dwarf galaxy problem [80, 81], the too-big-to-fail problem [82, 83] and the core-cusp problem [84]. In the simulations, the cold dark matter scenario clusters hierarchically and predicts a large number of satellite galaxies. However, the observations show less number of satellite galaxies [80, 81]. For example, the Milky Way size halo simulations show around 500 satellites, while observations show a far less number of satellite galaxies [81, 85]. Subsequently, the missing satellite creates a new problem also: The simulation of Galactic size haloes predicts a larger number of big satellites

that are so massive that there is no way not to host visible stars. Therefore, these massive satellites should be visible. In contrast, the observations show no such satellites consistent with the simulations [82, 83, 86]. N-body simulations of cold dark matter also show the cuspy profile for dark matter density at the halo centre, while the observation of rotation curves suggest the flat profile [84]. In the light of these problems, alternatives to the cold dark matter model have been proposed, for e.g. self-interacting dark matter [87–90], fuzzy cold dark matter [91, 92], warm dark matter (WDM) [93–97], etc. The difference between cold, warm and hot dark matter can be characterized in the form of their thermal velocities, $v = \sqrt{(3\,T/m)}$. Here, v, T and m are the speed, temperature and mass of the particle, respectively. One can see that a larger speed implies a higher temperature for a fixed mass of particles. Roughly, if their speed is less than ten percent of the light speed ($v \lesssim 0.1$), they can be considered cold dark matter candidates. If v is $\gtrsim 0.1$, they can be considered hot dark matter candidates [98]. The WDM lies in between the hot and warm dark matter. The WDM behaves similar to CDM on large length scales. This scale can be characterized in the form of "free-streaming length"— the other important concept to differentiate between hot, cold or warm dark matter. Typically, the free-streaming length can be estimated by how far a particle has travelled from beginning to matter-radiation equality [99],

$$\lambda_{\rm fs} = \int_0^{t_{\rm eq}} \frac{v}{a}\, dt\,, \tag{2.1}$$

here, $t_{\rm eq}$ is the matter-radiation equality time. For a length scale larger than $\lambda_{\rm fs}$, WDM behaves as CDM— i.e. it makes structures hierarchically above $\lambda_{\rm fs}$. While below the length scale $\lambda_{\rm fs}$, there is a possibility that WDM may create structures "top-down"— i.e. small structures may emerge via the fragmentations of large structures [95, 98, 99]. The free-streaming length can be found as [99],

$$\lambda_{\rm fs} \sim 0.4 \left(\frac{m_{\rm WDM}}{\rm KeV}\right)^{-4/3} \left(\frac{\Omega_{\rm WDM}\, h^2}{0.135}\right)^{1/3} {\rm Mpc}/h\,, \tag{2.2}$$

here, $m_{\rm WDM}$ is the mass of WDM particle and $\Omega_{\rm WDM}$ is the dimensionless energy density parameter for WDM. The free-streaming scale is inversely proportional to mass of particle. It implies that the size of formed-first-structures will increase for a smaller particle mass— the numbers of small-length-scale structures will suppress. For example, if one considers the mass of the WDM particle to be 10 KeV, then the free-streaming scale will be $\sim 2 \times 10^1$ Kpc. Therefore, one can overcome the missing satellite problem by considering an adequate mass of WDM. In the hot dark matter scenario, the free-streaming length typically is so large that density fluctuations below cluster scale would get washed up, and formed-first-structures would have been the size of superclusters. Later, their fragments might have formed the clusters, then galaxies. While the observation shows that galaxies formed first, then emerged as clusters and then superclusters due to their mutual gravitational attraction [98]. As discussed above, the nature of dark matter has significant effects on structure formation. The WDM can also solve the angular momentum problem— galaxies have smaller specific angular momenta in CDM simulation compared to observations [100, 101]. Additionally, by including the baryonic feedback with WDM can address the too-big-to-fail and core-cusp problems also [102–104]. The two popular candidates for WDM are sterile neutrinos and gravitinos. The presence of sterile neutrino warm dark matter having KeV mass can also explain the recently observed unexpected and unidentified emission line around 3.5 KeV in x-ray spectra of nearby galaxies and clusters [97, 105–108]. In this chapter, we consider sterile neutrino and study its lifetime and mixing angle with active neutrinos [9].

2.1 Sterile neutrinos as dark matter

Sterile neutrino with KeV mass is one of the exciting and well-motivated candidates for WDM (Ref. [35, 109, 110] and Refs. therein). The standard model of particle physics considers the neutrinos as massless. However, experiments and theoretical

models questioned the standard model of particle physics over the past years. One well-studied example is neutrino oscillation [111–114]. To explain the observations of neutrino oscillations, one has to extend the standard model to introduce the massive neutrinos (for more details, see the reviews [115, 116])[a]. There are three flavours of active neutrinos— electron, muon and tau neutrino, but absolute value of their masses are not very well known. Nevertheless, the square mass difference between different flavours has been constrained by various oscillation experiments, such as solar, atmospheric, reactor and accelerator (see the Ref. [121] and reviews [122, 123]). In the standard model of particle physics, all particles get their mass via Higgs Mechanism, but neutrinos remain massless. One of the mechanisms via which neutrinos can get their mass is the Seesaw mechanism. As of now, active neutrinos have been observed with only left-handed chirality [124]. To give mass to neutrinos, we also require the right-handed counterpart of active neutrinos. The right-handed neutrinos can have mass from a few eV to GUT scale [124]. In the Seesaw mechanism, sterile neutrino naturally appears as an eigenstate of the neutrino mass matrix. Introducing a new Yukawa interaction with new Weyl fermions N^β [123],

$$\mathcal{L}_{\rm Y} \supset -y^{\alpha\beta}(i\,\sigma^2\,H^*)\,L^\alpha N^\beta + h.c.\,, \tag{2.3}$$

here, α and β are summed over e, μ, τ and 1, 2, ..., n , respectively; n is the number of fields of N^β. $i\,\sigma^2\,H^*$ and $L^\alpha = (\nu^\alpha,\, e^\alpha)^T$ are $SU(2)_L$ doublet and carry opposite hypercharges: +1/2 and -1/2, respectively. Therefore, their combination is total singlet, implying N^β to be total singlet also [123]. When Higgs field (H) acquires vacuum expectation value (v), the neutrino mass term can be written as,

$$\mathcal{L}_{\rm mass} \supset -M_D^{\alpha\beta}\,\nu^\alpha\,N^\beta + h.c.\,, \tag{2.4}$$

[a]Takaaki Kajita with Arthur B. McDonald received the Nobel Prize in Physics for 2015 "for the discovery of neutrino oscillations, which shows that neutrinos have mass" [117–120].

the Dirac mass term $M_D^{\alpha\beta} \equiv y^{\alpha\beta}\, v/\sqrt{2}$. Since N^β does not have any strong, electromagnetic or weak coupling, it is called the sterile; and it can be considered a dark matter candidate. ν^α has weak coupling with standard model particles, and it is called active neutrino. As sterile neutrinos are singlet, in principle we can write a Majorana mass term for N^β: $\mathcal{L}_{\rm mass} = -(1/2)\, M_M^{\alpha\beta}\, N^\alpha\, N^\beta + h.c.$. From equation (2.4),

$$\mathcal{L}_{\rm mass} \supset -\frac{1}{2}\, n^T\, M\, n \equiv -\frac{1}{2}\, n^T \begin{bmatrix} 0 & M_D \\ M_D^T & M_M \end{bmatrix} n + h.c.\,, \tag{2.5}$$

here, $n = (\nu^e ... \nu^\tau,\, N^1 ... N^n)^T$, $M_D = M_D^{\alpha\beta}$ and $M_M = M_M^{\alpha\beta}$. Assuming $||M_M|| \gg ||M_D||$, as M_M is not protected by any symmetry and M_D can not be larger than electroweak scale because it will require Yukawa coupling $\gg 1$, the eigenvalues of mass matrix: $m_1^\nu = \mathcal{O}\,(M_D^2/M_M)$ and $m^N = \mathcal{O}(M_M)$. We get the light neutrino mass to $m^\nu \sim 0.1$ eV by taking $||M_D|| \sim 100$ GeV and $||M_M|| \sim 10^{14}$ GeV. The sterile neutrinos are stable— have a larger lifetime compared to the age of the Universe. Therefore, they can make an excellent candidate for the warm dark matter if they also have mass in the KeV range [122].

One of the minimal extensions of the standard model of particle physics, where neutrino mass and KeV sterile neutrinos in the context of dark matter are widely explored via the Seesaw mechanism, is the Neutrino Minimal Standard Model (νMSM) [122–125]. In this model, we can lower one of the eigenvalues of M_M to get KeV scale sterile neutrino while keeping others super-heavy. In the basis (ν_a, ν_s, N); N represents the heavier sterile states, the mass matrix [123],

$$M = \begin{pmatrix} 0 & 0 & 0 & M_s^1 & M_D^{11} & M_D^{12} \\ 0 & 0 & 0 & M_s^2 & M_D^{21} & M_D^{22} \\ 0 & 0 & 0 & M_s^3 & M_D^{31} & M_D^{32} \\ M_s^1 & M_s^2 & M_s^3 & \mu_s & 0 & 0 \\ M_D^{11} & M_D^{21} & M_D^{31} & 0 & M_M^1 & 0 \\ M_D^{12} & M_D^{22} & M_D^{32} & 0 & 0 & M_M^2 \end{pmatrix} \tag{2.6}$$

here, ν_s and ν_a are sterile and active neutrinos, respectively. Applying the Seesaw mechanism, we can find the mass of neutrinos: $M_\nu \simeq -M_D\, M_M^{-1}\, M_D^T - M_s\, \mu_s^{-1}\, M_s^T$; and the mass of light sterile neutrino: $m_s \simeq \mu_s$.

The νMSM model is a minimal extension of the standard model of particle physics— with only three additional sterile neutrinos up to the Planck scale. One having KeV scale mass— can account for dark matter. The other two heavier sterile neutrinos can account for the observed light neutrino masses by the Seesaw mechanism. They can also explain the baryon asymmetry in the Universe through oscillation-induced leptogenesis if they are nearly degenerate in the mass range 150 MeV−100 GeV [109, 125]. More details about KeV sterile neutrino models can be found in the review article by A. Merle [126].

2.2 Existing bounds on sterile neutrinos

The possibility of KeV mass range sterile neutrinos as a WDM candidate can be explored and constrained by the observation of large scale structures in the Universe [94]. There are several model-dependent mechanisms that can produce sterile neutrinos in the early Universe [35, 127, 128]. In recent years, various techniques have been proposed to probe the unexplored sterile neutrino dark matter parameter space, for example, by mapping of x-ray intensity at different redshift [129], by observing KeV energy photons using instruments onboard Transient High Energy Sky and Early Universe Surveyor (THESEUS) mission (for the details of instruments sensitivity of THESEUS, see the Ref. [130]), by exploring the imprints of sterile neutrino on solar neutrino fluxes [131], by testing the hypothesis of decaying-sterile-neutrino [132, 133], etc. The lower bound on the mass of sterile neutrinos can be obtained by the Pauli exclusion principle [35, 123]. These bounds depends on momentum distribution and the dwarf galaxy used for astronomical data [35, 123]. The authors of the ref. [134], finds the lower bound on the mass of non-resonantly produced sterile neutrino to be > 1.7 KeV when all the

dark matter is composed of sterile neutrinos. Additionally, the parameter space of sterile neutrino dark matter has been constrained by various observations and theoretical studies. The observations from Nuclear Spectroscopic Telescope Array (NuSTAR)[b] did not find any sign of anomalous x-ray lines for sterile neutrino mass range $10 - 40$ KeV. The future updated version of NuSTAR will be able to probe for sterile neutrino mass range $6 - 10$ KeV [36]. In the context of EDGES signal, authors of the reference [135], put a constraint on the Dodelson-Widrow sterile neutrinos mass to 63^{+19}_{-35} KeV. The WMAP, Lyα forest and x-ray observations constrain the sterile neutrino mass in the range from ~ 2 KeV to ~ 50 KeV [136–140]. The authors of the Refs. [141, 142] compare the observed satellite galaxy with conferred from WDM simulations of Galaxy-sized halo and constrain the mass of sterile neutrino $\gtrsim 2$ KeV. Further, individual bounds on the sterile neutrino parameter space can be found in the Refs. [39, 143–151].

2.3 Radiative decay of sterile neutrinos

Sterile neutrinos with KeV mass can decay to active neutrinos via two channels: $\nu_s \to \nu_a \, \nu_a \, \bar{\nu}_a$ and $\nu_s \to \nu_a \, \gamma$. In this work, we study the effect of radiative decay of sterile neutrinos on the thermal and ionization history of the Universe, and constrain the sterile neutrino decay time and mixing angle with active neutrinos. The decay of sterile neutrino to active neutrino via the radiative process can inject the photon energy into IGM and modify the absorption amplitude of the 21 cm signal during cosmic dawn. Hence, we can constrain the sterile neutrino decay time and mixing angle with the active neutrino using the 21 cm absorption signal. In this process, half of the total energy of a sterile neutrino ($m_{\nu_s}/2$) is carried away by a photon and remaining by an active neutrino. The decay width of sterile neutrino

[b] https://heasarc.gsfc.nasa.gov/docs/nustar/index.html

for radiative process can be written as ([35, 152] and reference cited therein),

$$\Gamma_{\nu_s} = \Gamma_{\nu_s \to \nu_a \gamma} = \frac{9\ \alpha\ G_F^2}{1024\,\pi^4}\ \sin^2(2\,\theta)\, m_{\nu_s}^5\,, \tag{2.7}$$

here, $\theta \equiv \sum_{i=e,\,\mu,\,\tau} |\theta_i|^2$ is the total mixing angle between sterile and active neutrinos. In equation (2.7), G_F and α are the Fermi and fine structure constant, respectively. m_{ν_s} stands for the mass of the sterile neutrino. The mixing angle $\theta \lll 1$, therefore $\sin^2(2\,\theta) \simeq 4\ \sin^2(\theta)$. We can write the decay width as [35, 152],

$$\Gamma_{\nu_s} = \tau_{\nu_s}^{-1} \simeq 5.52 \times 10^{-22}\ \sin^2(\theta)\ \left[\frac{m_{\nu_s}}{\mathrm{KeV}}\right]^5\ \left[\frac{1}{\mathrm{sec}}\right]\,, \tag{2.8}$$

here, τ_{ν_s} is the lifetime or decay time of sterile neutrinos. For sterile neutrinos to be dark matter candidate, their lifetime must be larger than age of the Universe, 4.4×10^{17} sec. Using this fact and equation (2.8), one can estimate the upper bound on the total mixing angle.

2.4 Impact on the thermal and ionization history

Evolution of the ionization fraction with redshift in the presence of energy injection by decaying sterile neutrinos [153–159],

$$\begin{aligned}\frac{dx_e}{dz} = \frac{\mathcal{P}}{H\,(1+z)} \times \left[\, n_{\mathrm{H}} x_e^2\, \alpha_B(T_{\mathrm{gas}}) - (1-x_e)\, \beta_B(T_{\mathrm{gas}})\, e^{-E_\alpha/T_{\mathrm{gas}}}\right] \\ - \frac{1}{H\,(1+z)} \left(\frac{1}{E_0} - \frac{1-\mathcal{P}}{E_\alpha}\right) \frac{(1-x_e)\ \mathcal{E}}{3\, n_{\mathrm{H}}}\,,\end{aligned} \tag{2.9}$$

where $x_e = n_e/n_{\mathrm{H}}$ is the ionization fraction, n_e is the free electron number density and n_{H} is the total hydrogen number density in the Universe. α_B and β_B are the case-B recombination coefficient and photo-ionization rate, respectively [153, 154, 156]. $E_0 = 13.6$ eV and $E_\alpha = (3/4)\, E_0$ are ground state binding energy and Lyα transition energy for the hydrogen atom, respectively. $\mathcal{P}$ is the Peebles coefficient

[156, 157, 160],

$$\mathcal{P} = \frac{1 + K_{\rm H}\,\Lambda_{\rm H}\,n_{\rm H}\,(1 - x_e)}{1 + K_{\rm H}\,(\Lambda_{\rm H} + \beta_{\rm H})\,n_{\rm H}\,(1 - x_e)}\,, \tag{2.10}$$

here, $K_{\rm H} = \pi^2/(E_\alpha^3\,H)$ and $\Lambda_{\rm H} = 8.22/\text{sec}$ account for the redshifting of Lyα photon due to expansion of the Universe and the 2S-1S level two photon decay rate of the hydrogen atom, respectively [161]. The last term in equation (2.9), describes the additional effect of sterile neutrinos decay on the ionization fraction. $\mathcal{E} \equiv \mathcal{E}(z, m_{\nu_s})$ is the energy deposition rate per unit volume into IGM gas due to decaying sterile neutrinos. It can be written as [156, 157, 162],

$$\mathcal{E}(z, m_{\nu_s}) = \mathcal{F}_S\; f_{\rm abs}(z, m_{\nu_s})\;\times\;\frac{\rho_{\nu_s,{\rm o}}}{\tau_{\nu_s}}\,(1+z)^3 \tag{2.11}$$

here, τ_{ν_s} is the lifetime of sterile neutrino to decay in a active neutrino and a photon. $\mathcal{F}_S$ is the fraction of the sterile neutrinos that are decaying. We consider that all sterile neutrinos are decaying, i.e. $\mathcal{F}_S = 1$. $\rho_{\nu_s,0} = m_{\nu_s}\,n_{\nu_s,0}$ is the present day energy density of sterile neutrino. $n_{\nu_s,0}$ is the present day number density of sterile neutrinos. For the present work, we consider that all the dark-matter is composed of sterile neutrinos, $\rho_{\nu_s,0} \equiv \rho_{\rm DM,0}$, and $\rho_{\rm DM,0}$ is the present day dark-matter energy density [35, 128, 162, 163]. $f_{\rm abs}(z, m_{\nu_s})$ is the energy deposition efficiency into IGM by decaying sterile neutrinos. The energy deposition happens due to only radiative decay of sterile neutrino as active neutrinos interact very weakly with matter. Therefore, we consider only radiative decay of sterile neutrinos. $f_{\rm abs}(z, m_{\nu_s})$ depends on the redshift and mass of sterile neutrino [162]. The mass of decaying particles enters only through $f_{\rm abs}(z, m_{\nu_s})$. In the presence of energy deposition into IGM, the gas temperature evolution with redshift [153–157, 159],

$$\begin{aligned}\frac{dT_{\rm gas}}{dz} = 2\frac{T_{\rm gas}}{(1+z)} + \frac{\Gamma_C}{(1+z)\,H}\,(T_{\rm gas} - T_{\rm CMB}) \\ - \frac{2}{3\,H\,(1+z)}\times\frac{(1+2\,x_e)\;\mathcal{E}}{3\,n_{\rm tot}}\,,\end{aligned} \tag{2.12}$$

here, $n_{\rm tot} = n_{\rm H}\,(1 + f_{\rm He} + x_e)$ is the total number density of gas, $f_{\rm He} = n_{\rm He}/n_{\rm H}$ is the helium fraction, $n_{\rm He}$ is the helium number density. The first term in this equation comes due to the expansion of the Universe. The matter temperature falls with redshift adiabatically: $\propto (1+z)^2$ when Compton scattering (second term) becomes insufficient ($z \lesssim 200$) and $\tau_{\nu_s} \to \infty$. The Compton scattering rate is defined as,

$$\Gamma_C = \frac{8\,\sigma_T\,a_r T_{\rm CMB}^4\,x_e}{3\,(1+f_{\rm He}+x_e)\,m_e}\,, \tag{2.13}$$

where, σ_T, a_r and m_e are the Thomson scattering cross-section, Stefan-Boltzmann radiation constant and mass of electron, respectively. Above the redshift $z \sim 200$, the gas remains in thermal equilibrium with photons due to Compton scattering as $\Gamma_C \gg H$. At $z = 200$, one can find that $\Gamma_C \approx 1.4 \times 10^{-14}$ sec^{-1} when $\mathcal{E} = 0$, while, $H = 3.6 \times 10^{-15}$ sec^{-1}. As $\Gamma_C \propto (1+z)^4$ and $H \propto (1+z)^{3/2}$ for matter dominated era, the Compton scattering rate will dominate over H as one increase z above 200. Therefore, the gas and CMB share same temperature above $z \sim 200$ — as second term dominates over the first term. Below $z \sim 200$, the Compton scattering rate becomes smaller compared to H resulting in an adiabatic evolution of the gas when there is no last term present in equation (2.12). The last term corresponds to the energy deposition into IGM due to radiative decay of sterile neutrinos. Following the Refs. [156, 157, 164, 165], we consider the 'SSCK' approximation— in which $(1-x_e)/3$ fraction of deposited energy goes into ionization, nearly same amount goes into excitation, and remaining $(1+2x_e)/3$ fraction goes into IGM heating. We also discuss the projected bounds on sterile neutrinos after the inclusion of the process of gas heating in the cosmic dawn era by CMBR using Ref. [34], in subsequent discussion we call this process VDKZ18. Here, the energy transfer between gas and CMBR is mediated by Lyα photons from the first stars. The authors claim that it can increase the gas temperature by the order of ($\sim 10\%$) at $z \sim 17$. Here, it is to be noted that we do not include the x-ray heating of the gas due to the uncertainty of known physics of the first stars. For a fix value of

T_{21} at a redshift, if we include the x-ray heating of the gas, the projected bounds becomes stronger. Including the heating due to VDKZ18 effect, equation (2.12) will modify as,

$$\frac{dT_{\rm gas}}{dz} = \left.\frac{dT_{\rm gas}}{dz}\right|_{\rm [eq.(2.12)]} - \frac{\Gamma_R}{(1+z)\,(1+f_{\rm He}+X_e)}\,, \tag{2.14}$$

where, $dT_{\rm gas}/dz\big|_{\rm [eq.(2.12)]}$ represents the temperature evolution in equation (2.12), and heating rate due to energy transfer from CMB photons to the thermal energy of gas by Lyα photons,

$$\Gamma_R = x_{\rm HI}\,\frac{A_{10}}{2\,H}\,x_R\left[\frac{T_R}{T_S}-1\right]\,T_{10}\,, \tag{2.15}$$

here, $A_{10} = 2.86\times10^{-15}$ sec^{-1} is the Einstein coefficient for spontaneous-emission from triplet state to singlet state. $x_R = 1/\tau_{21}\times[1-\exp(-\tau_{21})]$ and $\tau_{21} = 8.1\times 10^{-2}\,x_{\rm HI}\,[(1+z)/20]^{1.5}\,(10\ {\rm K}/T_S)$ is the 21 cm optical depth. $T_{10} = 2\pi\nu_{10} = 0.0682$ K and $x_{\rm HI}\simeq 1-x_e$ is the neutral hydrogen fraction in the Universe.

2.5 Bounds on the sterile neutrinos

As described in the (1.3), we get an absorption profile in the 21 cm signal around redshift $z\sim 17$ with an amplitude of $T_{21}\sim -220$ mK in the theoretical models based on ΛCDM framework of cosmology. We take 21 cm differential brightness temperature such that it does not change, from its standard value (~ -220 mK), by more than about a factor of 1/4 (i.e. -150 mK) or 1/2 (i.e. -100 mK) at redshift 17.2 . We solve the coupled equations (2.9) and (2.12) for different mass and lifetime of sterile neutrino to get $x_{\rm HI}$ and $T_{\rm gas}$ at redshift $z = 17.2$. To get any absorption signal in redshift range $15-20$, the gas temperature should be less than CMB temperature in shaded region. By requiring $T_{21}\simeq -150$ mK or -100 mK at z=17.2, we can put the projected constraints on the lifetime of sterile neutrinos.

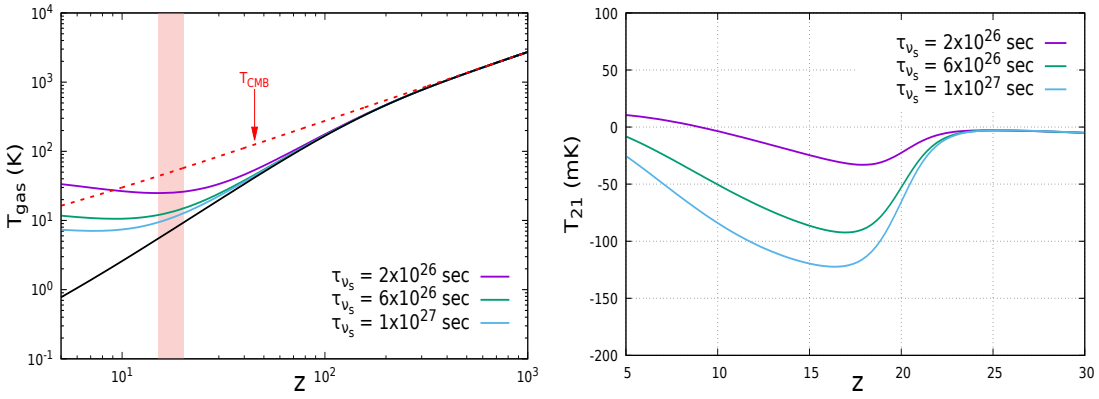

(a) (b)

Figure 2.1: The gas temperature evolution with redshift in the presence of decaying sterile neutrinos. The red dashed line represents the CMB temperature evolution. The black solid line depicts the $T_{\rm gas}$ when there is no sterile neutrino decay. The shaded region corresponds to EDGES absorption signal, i.e. $15 \leq z \leq 20$. In these figures, we keep mass of sterile neutrino fix to 10 KeV and vary lifetime. In figure (2.1b), we plot evolution of 21 cm differential brightness temperature as a function of redshift for the cases represented in figure (2.1a).

Subsequently, using equation (2.8), we can also put projected constraints on the mixing angle of sterile neutrinos with active neutrinos.

In the figures (2.1a), (2.2a) and (2.3a), we plot the gas temperature evolution as a function of redshift for different mass and lifetime of sterile neutrino. The red dashed line in all plots represents the CMB temperature evolution with redshift. The black solid line represents the gas temperature evolution when there is no effect of decaying sterile neutrino on the IGM gas. The shaded pink region corresponds to redshift range $15 \leq z \leq 20$. We obtain these results by considering $f_{\rm abs}(z, m_{\nu_s})$ from Ref. [162]. In figures (2.1b), (2.2b) and (2.3b), we plot the evolution of the 21 cm differential brightness temperature as a function of redshift for the scenarios discussed in figures (2.1a), (2.2a) and (2.3a), respectively. We consider the *tanh* parametrization model for the Wouthuysen-Field coupling coefficient (x_α) to get

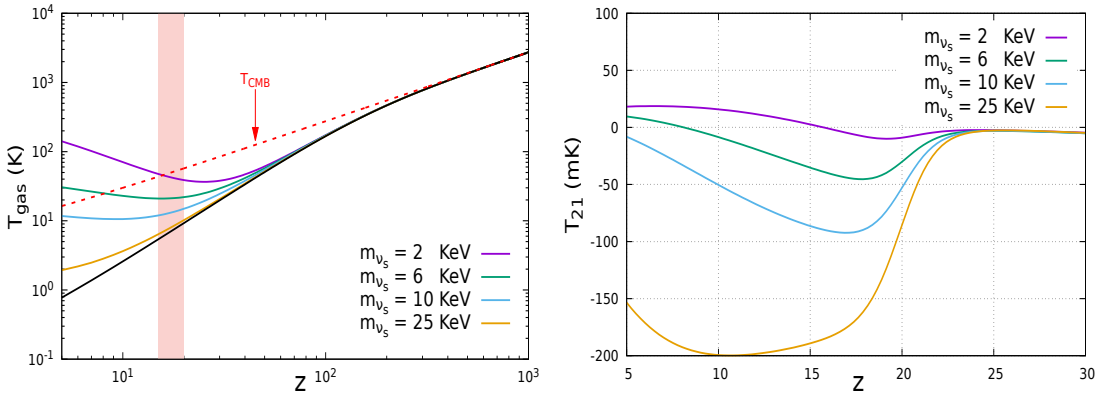

(a) (b)

Figure 2.2: The figure caption is same as in figure (2.1), except here, we consider τ_{ν_s} constant to 6×10^{26} sec and vary mass of sterile neutrino.

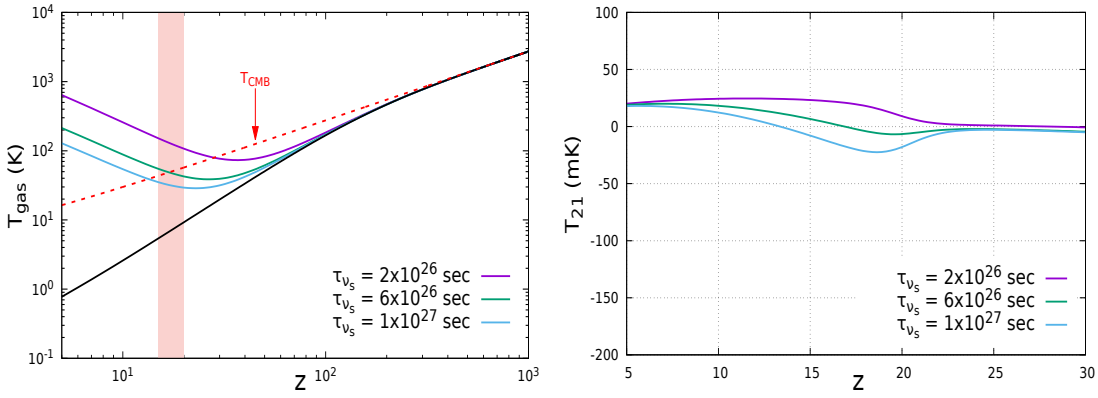

(a) (b)

Figure 2.3: The figure caption is same as in figure (2.1), except here, we keep $f_{\rm abs}(z, m_{\nu_s}) = 1/2$ and vary lifetime of sterile neutrino.

T_{21} profiles [51, 74, 75]. In the shaded region of the figures, the spin temperature can be approximated as gas temperature. Therefore, when the gas temperature is lower than CMB temperature, we get the absorption profile, i.e. $T_{21} < 0$. When the gas temperature rises above the CMB temperature, T_{21} becomes positive, and we see an emission profile. In all figures (2.1b), (2.2b) and (2.3b), above the redshift $z \gtrsim 25$, x_α, $x_c < 1$, therefore, the spin temperature is dominated by CMB temperature, i.e. $T_{21} \approx 0$. To get the absorption profile at $z \sim 17$, one has to keep $T_{\rm gas} < T_{\rm CMB}$.

In figure (2.1a), we keep the mass of sterile neutrino (m_{ν_s}) fix to 10 KeV. The violet solid line depicts the gas temperature evolution when lifetime of sterile neutrino is 2×10^{26} sec. As we increase the lifetime of sterile neutrino from 2×10^{26} sec to 1×10^{27} sec, the gas temperature decreases— shown by green and cyan curves. It happens because by increasing the τ_{ν_s}, the radiative decay of sterile neutrinos decreases and the number of photons injected into IGM also decreases. Therefore, we get less heating of IGM by increasing the τ_{ν_s}, and it results in a smaller amplitude (larger dip) of T_{21} shown by figure (2.1b).

In plot (2.2a), lifetime of sterile neutrino is fixed to 6×10^{26} sec and the values of m_{ν_s} varies from 2 KeV (violet solid line) to 25 KeV (yellow solid line). If one increases the sterile neutrino mass from 2 KeV (violet line) to 6 KeV (green line), the heating of IGM decreases significantly in the shaded region. It happens because $\rho_{\nu_s} = m_{\nu_s} n_{\nu_s}$, n_{ν_s} is the number density of sterile neutrinos. Therefore at a particular redshift, when one increases m_{ν_s} the number density of sterile neutrino decreases, and we get less photon injunction, produced from decaying sterile neutrinos, into the IGM. Hence, one gets less heating of IGM when the mass of sterile neutrino increases, and it results in a smaller amplitude (larger dip) of T_{21} shown by figure (2.2b).

If one considers the immediate and complete absorption of the photon energy into IGM, then energy deposition efficiency, $f_{\rm abs} = 1/2$ — half of the total energy of sterile neutrino will be carried away by active neutrino [162, 166]. The mass

of the sterile neutrino in the equations (2.9) and (2.12), enters through only $f_{\rm abs}$. Therefore, the energy deposition rate, equation (2.11), will depend only on the lifetime of sterile neutrinos. This case has been depicted in figure (2.3a) for the different values of τ_{ν_s}. In this case, as expected, the heating of IGM increases more compared to the cases in figure (2.1a). The corresponding profiles for 21 cm signal are shown in figure (2.3b). In figure (2.3a), the gas temperature for $\tau_{\nu_s} = 2\times10^{26}$ sec is higher than the CMB temperature in the shaded region– (violet line). Therefore, we get a emission profile for T_{21} in figure (2.3b) for $\tau_{\nu_s} = 2 \times 10^{26}$ sec. For $\tau_{\nu_s} = 6 \times 10^{26}$ sec, at redshift ~ 17, the gas temperature is comparable to the CMB temperature, therefore we do not see any absorption/emission in the 21 cm signal. Above the redshift ~ 17, temperature of gas is lower than CMB, therefore, we see a small absorption in the profile. Below the redshift ~ 17, the temperature of the gas is higher than CMB, therefore, we see a emission profile. For the case with $\tau_{\nu_s} = 1 \times 10^{27}$ sec, in the shaded region, temperature of the gas is smaller than the CMB (cyan line), therefore, we get an absorption profile for the 21 cm signal— figure (2.3b).

In figure (2.4), we plot the lower projected constraints on lifetime as a function of m_{ν_s} by requiring T_{21} such that it does not suppress the standard theoretical value of $T_{21}(z = 17.2) \approx -220$ mK more than about a factor of 1/4 or 1/2. Considering $T_{21} < -150$ mK, will further strengthen our projected bounds. The red coloured curves depict the lower projected constraints on τ_{ν_s} when $T_{21} \simeq -150$ mK, while the black coloured curves represent the lower projected constraint on τ_{ν_s} when $T_{21} \simeq -100$ mK. To get the dashed line, we do not take into account the VDKZ18 heating of the gas. For the dotted line we consider VDKZ18 heating of the gas. Inclusion of VDKZ18, gives more stringent projected constraint on τ_{ν_s} as gas temperature rises due to the energy transfer from CMB photons mediated by Lyα photons. In figure (2.5), we obtained the upper projected constraint on mixing angle of sterile neutrinos with active neutrinos as a function of mass. For reference, we have also plotted the x-ray constraint on mixing angle as function

of m_{ν_s}. The constraint is obtained by assuming solely radiative decay of sterile neutrinos. x-ray constraint comes from the fact that no such x-rays have been seen in observations [35]. The red and black coloured curves depict the upper projected constraint on mixing angle when $T_{21} \simeq -150$ mK and -100 mK, respectively. To get the dashed curves, we do not take into account the VDKZ18 heating of the gas. For the dotted line we have included the VDKZ18 heating of the gas. Here, it is to noted that these bounds do not depend on dark-matter clustering. Therefore, the bounds are free of astrophysical parameters such as density profile or mass function of dark-matter halos, etc. To obtain these bounds, we do not consider any non-standard cooling mechanism to cool the IGM or any source of radio photons. The results in figure (2.5) are comparable with the x-ray constraint for the higher mass of sterile neutrinos, while we get more stronger bounds for lower mass.

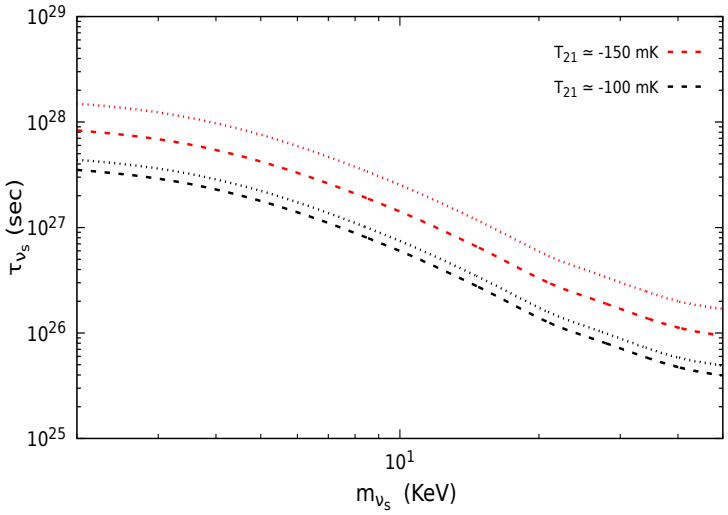

Figure 2.4: The figure represents lower projected bounds on the lifetime of sterile neutrinos as a function of mass of sterile neutrinos by keeping 21 cm differential brightness temperature, $T_{21} \simeq -150$ and -100 mK. The dotted (dashed) line represents the case when energy transfer from CMB photons to gas is included (excluded) [34].

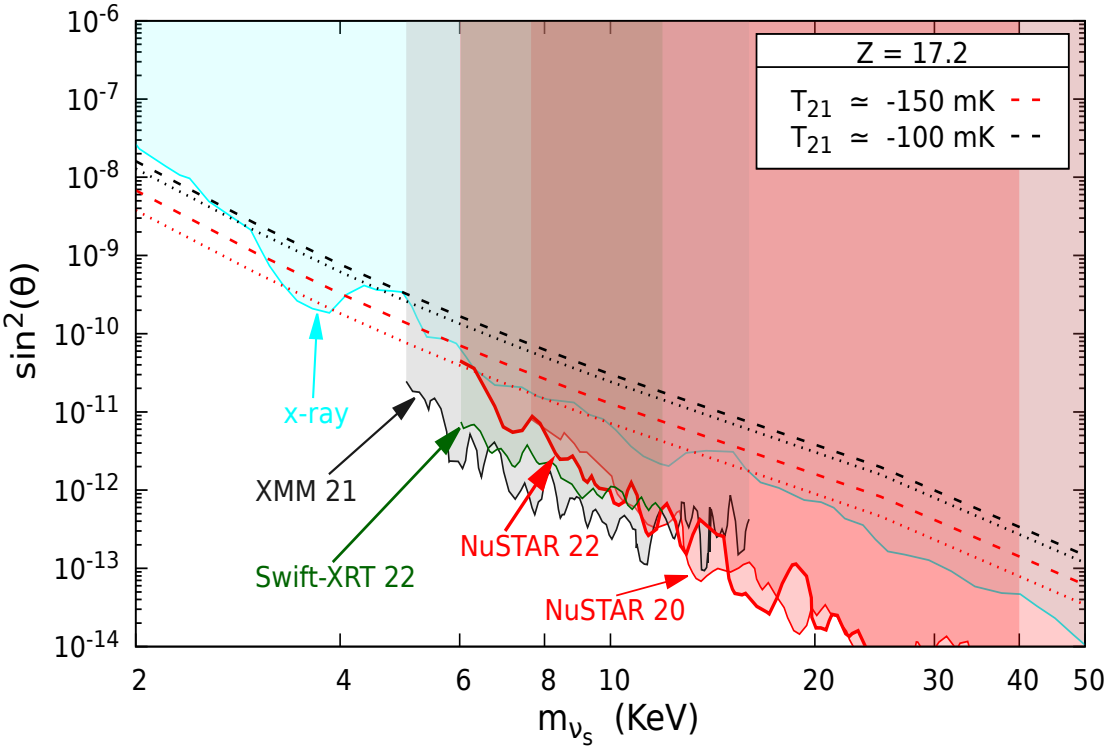

Figure 2.5: The figure represents upper projected bounds on the mixing angle of sterile neutrinos with active neutrinos as a function of mass of sterile neutrinos by keeping 21 cm differential brightness temperature, $T_{21} \simeq -150$ and -100 mK. The dotted (dashed) line represents the case when energy transfer from CMB photons to gas is included (excluded) [34]. The shaded regions are excluded for corresponding observations. The x-ray constraint on mixing angle (cyan shaded region) has been taken from the Ref. [35]. The red shaded region depicts the upper bounds on $\sin^2(\theta)$ from NuSTAR observations [36, 37]. Here, we have also plotted the recently reported bounds (after publication of our article) on $\sin^2(\theta)$ by NuSTAR— represented by NuSTAR 22 [37] and by Swift-XRT— represented by Swift-XRT 22 [38]. The grey shaded region is excluded by XMM-Newton [39].

2.6 Summary

We have constrained the sterile neutrino dark matter lifetime and mixing angle with active neutrino as a function of sterile neutrino mass, such that energy injection from radiative decay of sterile neutrino does not change the standard 21 cm absorption signal (~ -220 mK) more than about a factor of 1/4 (-150 mK) or 1/2 (-100 mK) at the redshift, $z = 17.2$. We have considered the two scenarios to get the bounds: First, IGM evolution without the heat transfer from the background radiation to gas mediated by Lyα photons (VDKZ18 effect). Next, we have considered the VDKZ18 effect on the IGM gas. The following summarises our results for $T_{21} = -150$ mK:

In the first scenario, the lower bound on the sterile neutrino lifetime varies from 8.3×10^{27} sec to 9.4×10^{25} sec by varying sterile neutrino mass from 2 KeV to 50 KeV. The lifetime of sterile neutrino decrease when one increases the mass of the sterile neutrino. It happens because $\rho_{\nu_s} = m_{\nu_s} n_{\nu_s}$. At a particular redshift, when one increases m_{ν_s}, the n_{ν_s} decreases. Consecutively, one gets less radiative decay of sterile neutrinos. Therefore, we get more window to increase the gas temperature, i.e. we can decrease the lifetime of sterile neutrinos. The upper bound on the mixing angle ($\sin^2\theta$) varies from 6.8×10^{-9} to 6.1×10^{-14} by varying sterile neutrino mass from 2 KeV to 50 KeV.

In the second scenario, the lower bound on the sterile neutrino lifetime varies from 1.5×10^{28} sec to 1.7×10^{26} sec by varying sterile neutrino mass from 2 KeV to 50 KeV. While the upper bound on the mixing angle varies from 3.8×10^{-9} to 3.42×10^{-14} by varying sterile neutrino mass from 2 KeV to 50 KeV.

We have also plotted the x-ray constraint to rule out some parameter space for mixing angle of the sterile neutrinos with active neutrinos [35]. Although we have considered that sterile neutrinos account for all the dark matter in the Universe, sterile-neutrino may account for only a fraction of the dark matter abundance. In this scenario, the bounds on the sterile neutrino lifetime and mixing angle with

active neutrino may modify.

2.7 Additional study

2.7.1 Bounds in light of varying T_{21} and redshift

We have also studied the projected constraints on τ_{ν_s} and $\sin^2(\theta)$ by varying the absorption amplitude of T_{21} between 0 mK (no signal) to -200 mK at $z = 17$. If we increase the value of T_{21} above 0, it gives a emission signal instead of an absorption signal. Therefore, we restrict the maximum value of T_{21} to 0. Also, we do not take the values of T_{21} below ~ -200 mK, as the sterile neutrino term in the temperature evolution equation becomes insignificant compared to adiabatic and Compton scattering term. In the ΛCDM model without invoking any new physics, we get $T_{21}(z = 17) = -220.215$ for the cosmological parameters $\Omega_{\rm m} = 0.31$, $\Omega_{\rm b} = 0.048$ and $h = 0.68$. For the demonstration purpose of this, we take $m_{\nu_s} = 2$ KeV. After inclusion of physics of decaying sterile neutrinos, we get $T_{21}(z = 17) = -220.213$ mK for $\tau_{\nu_s} = 4 \times 10^{32}$ sec. If we increase the value of T_{21} only by 9.7×10^{-2} percent (from $T_{21} = -220.213$ mK to -220 mK), the value of τ_{ν_s} changes significantly from 4×10^{32} sec to 3.78×10^{30} sec— decreases by more than a factor of hundred. Therefore, we do not consider bounds on the τ_{ν_s} and $\sin^2(\theta)$ near the maximal absorptional value of T_{21}; and vary the value of T_{21} from -200 to 0 mK.

In figure (2.6a), we have plotted the lower projected bounds on the lifetime of sterile neutrinos as a function of mass for various values of T_{21} at $z = 17$. In figure (2.6b), we have plotted the upper projected bounds on the mixing angle of sterile neutrinos with active neutrinos as a function of mass for various values of T_{21} at $z = 17$. NuSTAR 22 bound is reported in July 2022 [37] and Swift-XRT 22 is reported in August 22 [38]. The observational bounds indicate that the decay of sterile neutrinos will not significantly impact the thermal history of the

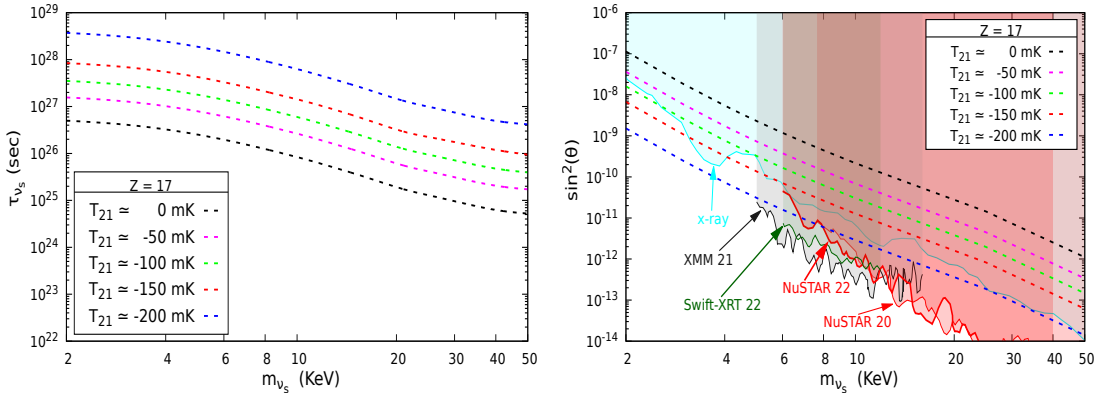

(a) (b)

Figure 2.6: Plot (2.6a), shows lower projected bounds on the lifetime of sterile neutrinos as a function of mass, while plot (2.6b), shows upper projected bounds on the mixing angle of sterile neutrinos with active neutrinos as a function of mass of sterile neutrinos for varying 21 cm differential brightness temperature (T_{21}) at $z = 17$. In figure (2.6b), the shaded regions are excluded for corresponding observations. The cyan shaded region represents the x-ray constraint [35]. The red shaded region depicts the upper bounds on $\sin^2(\theta)$ from NuSTAR observations [36, 37]. Here, we have also included the recently reported bounds (after publication of our article) on $\sin^2(\theta)$ by NuSTAR— represented by NuSTAR 22 [37] and by Swift-XRT— represented by Swift-XRT 22 [38]. The grey shaded region is excluded by XMM-Newton [39].

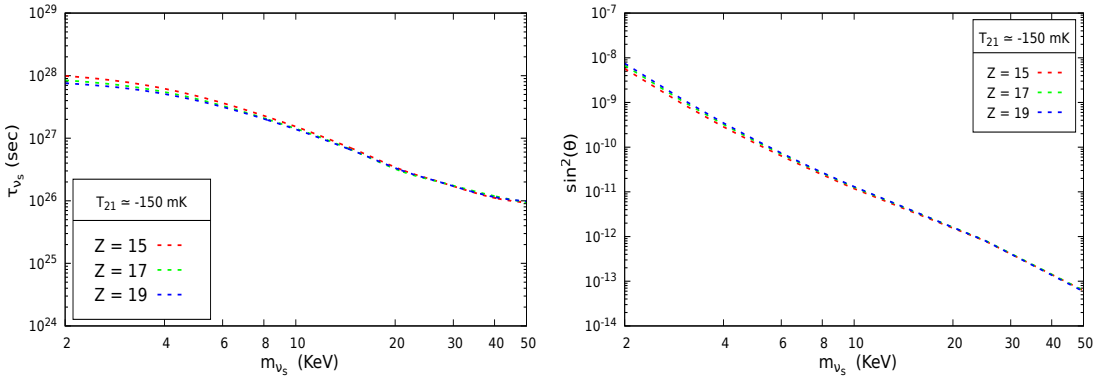

(a) (b)

Figure 2.7: Plot (2.7a), shows lower projected bounds on the lifetime of sterile neutrinos, while plot (2.7b), shows upper projected bounds on the mixing angle of sterile neutrinos with active neutrinos by keeping T_{21} to -150 mK for different values of redshift.

Universe as the parameter space is excluded more stringently by observations for a higher mass of sterile neutrinos. For example, XMM 21 excludes the values of $\sin^2(\theta) \gtrsim 2 \times 10^{-12}$ for $m_{\nu_s} \simeq 6$ KeV. If one wants to exclude this parameter space using 21-cm signal, it requires to consider $T_{21} < -200$ mK— i.e. no significant modification in the thermal and ionization history of the Universe.

For further analysis with variation of redshift values, we have also added the plots for the case with different values of redshift keeping the value of T_{21} constant— presented in figure (2.7). Here, we vary redshift between 15 to 19. As it is shown in figure (4.4), for fiducial models for Lyα coupling and x-ray heating, we can not take the spin temperature to be gas temperature above $z \sim 17$ and also x-ray starts to dominate below $z \sim 17$. Therefore, we restrict ourselves about redshift 17 and take a range from 15 to 19. Here, we do not see significant variation in the projected bounds of lifetime and mixing angle with variation of the values of redshift.

In figure (2.8), we vary both the value of redshift and T_{21}, and plot the lower

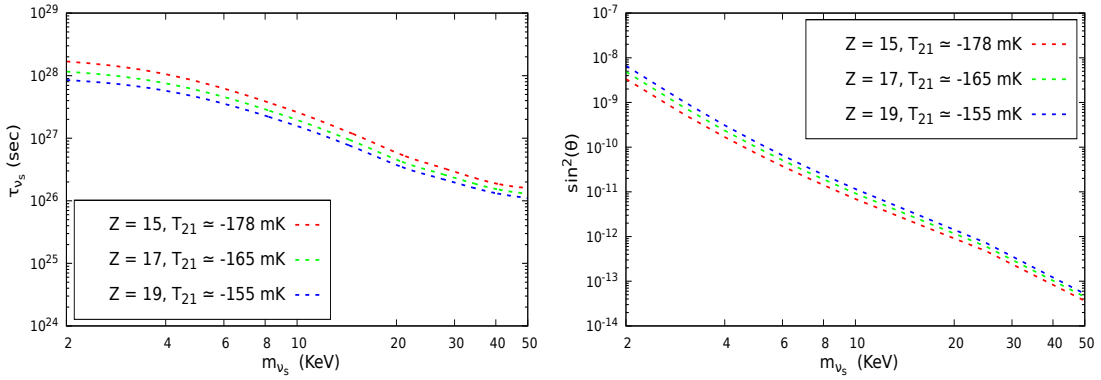

(a) (b)

Figure 2.8: Plot (2.7a), shows lower projected bounds on the lifetime of sterile neutrinos, while plot (2.7b), shows upper projected bounds on the mixing angle of sterile neutrinos with active neutrinos by keeping T_{21} such that it does not change more than a factor of 1/4 from the minimum possible amplitude based on ΛCDM model for corresponding values of redshift.

projected bounds on τ_{ν_s} in figure (2.8a) and upper projected bounds on $\sin^2(\theta)$ in figure (2.8b). Here, we choose the value of T_{21}, such that, it does not change more than a factor of 1/4 from the minimum possible amplitude based on ΛCDM model. For the cosmological parameters, given above, we get the minimum possible amplitude of $T_{21}^{\rm Min}$ to be -236.7 mK at $z = 15$, -220.2 mK at $z = 17$ and -206.1 mK at $z = 19$.

"The universe doesn't allow perfection."

Stephen Hawking, *A Brief History of Time*

3

Primordial Black Hole Dark Matter

Primordial black holes have attracted much interest in recent years and have been a part of intense studies for more than five decades. The idea of the black hole goes back to the 18th century. In 1784, John Michell proposed that there could be such supermassive bodies that light could not pass them, or all light emitted would return towards them [10–12]. Later, in 1915 Albert Einstein developed the general theory of relativity. In 1916, Karl Schwarzschild found the solution of black holes by solving the Einstein field equations for a point mass [167]. Subsequently, in 1963, Roy Kerr found the solution of rotating black holes [168]. In 1965, the more general solution of a rotating and charged black hole was found [169]. There is a possibility that a colossal number of black holes might have been formed in the very early Universe— known as primordial black holes (PBHs). PBHs can be created by various mechanisms. It was first suggested by Zeldovich and Novikov that the presence of initial inhomogeneities in the Universe can form PBHs [170]. There is

a possibility that for many regions in the space, gravitational energy of the initial density fluctuations can exceed the kinetic energy. These regions would have a gravitational collapse instead of the expanding with Universe creating collapsed objects with a minimum mass of $\sim 10^{-5}$ g [171–173]. There are various mechanisms that can produce inhomogeneities in the early Universe. For example, such density fluctuations can be generated due to the vacuum strings produced during the grand unification phase transition [174]. Indeed, these fluctuations were present in the very early Universe, as evident from observations of structures in the Universe. The other explanations of PBHs formation include the collapse of cosmic string loops, collisions of bubbles, etc. The cosmic string loops can disappear in two ways: First, they can shrink into scalar and gauge particles. Second, some loops with specific initial shapes may disappear by collapsing in size below their Schwarzschild radius and form black holes [175–178]. In the article [179], the authors consider the formation of PBHs due to collapsing cosmic strings and argue that PBHs can significantly contribute to the dark matter density if their relic mass is larger than $10^3\, m_{\rm pl}$, here $m_{\rm pl}$ is the Planck mass. In another scenario, the collapse of the cusps neighbourhood of cosmic strings loops can also form a large number of spinning PBHs [180]. The collisions between the bubbles during various phase transitions in the Universe can also give rise to the formation of PBHs [181–183]. PBHs can also be produced in various inflation models [184–186].

Depending on the formation time (t), PBHs can have a wide range of masses (in most of the cases roughly order of the Hubble horizon mass at the formation time) [187, 188],

$$M_{\rm PBH} \sim 10^{15} \left[\frac{t}{10^{-23}\,{\rm sec}}\right] {\rm g}. \tag{3.1}$$

For example, PBHs with mass 10^{15} g might have formed at $t \sim 10^{-23}$ after big-bang. In another example, PBHs formed during the QCD phase transition ($t \sim 10^{-5}$ sec) might have a mass comparable to a solar mass [189]. PBHs formed

around neutrino decoupling ($t \sim 1$ sec) can have a mass about 10^5 $M_\odot$.

3.1 Primordial black holes as dark matter

In the last decades, many particle-dark matter models have been proposed to explain the various astrophysical observations, as discussed in chapter (2). The laboratory experiments for direct detection of dark matter have not observed any signature yet, for example, DarkSide-50, LUX, XENON1T, PandaX-II, CRESST, PICO, etc. [190–195]. In this situation, it is desirable to look for alternative scenarios where dark matter may not be an elementary particle. As PBHs are massive, interact only gravitationally and are formed in the very early Universe, they can be considered as a potential candidate for non-particle dark matter. Recently, PBHs have gathered much attention in the scientific community after the black hole binary merger detection by Virgo and LIGO collaborations, and these events suggest that PBHs may constitute a fraction of dark matter [13–15, 196–198]. PBHs having a mass below $\sim 10^{22}$ g can explain all the dark matter in the Universe as they are not ruled out by microlensing constraints [199]. We will discuss other constraints on dark matter fractions in the form of PBHs with mass below $\sim 10^{22}$ g later in the sections (3.2) and (3.4). One can explain the existence of dark matter in the form of PBHs without considering physics beyond the standard model (BSM) of particle physics by considering standard model Higgs fluctuations during inflation as instability can occur in Higgs potential at a scale $\mathcal{O}(10^{11}$ GeV) [200]. In the article [184], authors consider the double inflation model to explain the formation of PBHs between two inflations and argue that PBHs can be accounted for dark matter in the Universe. PBHs as missing matter or dark matter in the context of galaxy formation has been explored in old literature also [201, 202]. Authors of the Ref. [185], consider the formation of PBH dark matter due to the mild-waterfall phase of hybrid inflation and discuss how the tail of the mass distribution of PBHs can explain the origin for the supermassive black holes

observed at galactic centres. These massive back holes can also provide the seed for present-day observed structures [185, 203]. A fraction/all of dark matter in the form of PBHs can produce the r-process nucleosynthesis— a process that is responsible for producing about half of the heavier nuclei than iron, in the mass range $10^{-14}\,\mathrm{M}_\odot < M_{\rm PBH} < 10^{-8}\,\mathrm{M}_\odot$ [204]. Black holes can lose their mass by the emission of energetic particles due to Hawking evaporation [205]. For non-rotating and non-charged black holes formed in the very early Universe, their evaporation time scale can be given by [187],

$$\tau(M_{\rm PBH}) \sim \left[\frac{M_{\rm PBH}}{10^{15}\,\mathrm{g}}\right]^3 \mathrm{Gyr}. \tag{3.2}$$

Therefore, PBHs having mass larger than 10^{15} g can survive the Hawking evaporation and account for present-day dark matter density [206].

3.1.1 Signature of Primordial Black Holes

It is possible that a fraction of PBHs can grow to intermediate-mass black holes and explain the ultraluminous x-ray sources reported in various observations [185, 207–209]. There are several hints that indicate the presence of PBHs, such as dynamics and star clusters of ultra-faint-dwarf-galaxies, correlations between x-ray and infrared cosmic backgrounds, etc. (for a detailed review, see Ref. [210]). The presence of evaporating PBHs can explain the galactic/extra-galactic γ-ray background radiation [211–214], short-duration γ-ray bursts [215, 216], and reionization by injection of energetic photons and $e^{\pm}$ radiations into IGM [217, 218]. The emission of nucleons by evaporating PBHs can explain the observed baryon number density if more baryons are produced compared to antibaryons— in a baryon-symmetric Universe [213]. Clustering between PBHs can provide the seeds for galaxy formation. PBHs evaporation can explain the observed point-like γ-ray sources [217]. The presence of massive PBHs can also serve as seeds for active galactic nuclei (AGN) [217].

3.2 Existing bounds on Primordial Black Holes

The fraction of dark matter in the form of PBHs ($f_{\rm PBH} \equiv \Omega_{\rm PBH}/\Omega_{\rm DM}$) is constrained from various astrophysical observations and theoretical predictions. Here, $\Omega_{\rm PBH}$ and $\Omega_{\rm DM}$ are the dimensionless density parameters for PBHs and dark matter, respectively. PBHs with mass smaller than $\sim \mathcal{O}(10^{15}$ g) may have evaporated as of now and can be constrained from the impact on big bang nucleosynthesis by evaporated particles, background radiation etc. Higher mass PBHs can be constrained by the effect on large-scale structures, gravitational wave and lensing, and impact on thermal and ionization history of the IGM (for details, see the recent reviews [187, 219, 220] and the references cited therein). In the context of the 21 cm signal, the upper bound on the $f_{\rm PBH}$ can be found in Refs. [221–228]. Angular momentum is a fundamental property of a black hole, and it can modify the Hawking evaporation drastically [40, 229–231]. In the case of rotating PBHs, authors of the Refs. [41, 232] have reported the various types of bound on $f_{\rm PBH}$ as a function of PBHs mass and spin. Future collaboration, All-sky Medium Energy Gamma-ray Observatory (AMEGO)[a] will be able to constrain some parameter space for the rotating PBHs [42]. We discuss more bounds on the fraction of PBH dark matter in the result and discussion section (3.4). In this chapter, we consider the rotating PBHs and constrain dark matter fraction in the form of PBHs as a function of their mass for various values of angular momentum in the light of global 21 cm signal [16].

3.3 Impact on the thermal and ionization history

During the cosmic dawn era, the evolution of the gas temperature and ionization fraction of the Universe are well-known [153, 154]. The addition of any exotic source of energy during the cosmic dawn era can significantly impact the ionization

[a] https://asd.gsfc.nasa.gov/amego/index.html

and thermal history of the Universe. Therefore, we can constrain the properties of such exotic sources from the observations during the cosmic dawn era. Evaporating PBHs can heat the gas and modify the free electron fraction in the IGM [46, 232]. Rotating PBHs can emit more particles into IGM and substantially affect the IGM evolution compared to non-rotating PBHs [214, 229, 233]. Therefore, it is important to study the properties of spinning PBHs. Black holes can get their spin depending on generation mechanisms, merger or accretion [234–244]. PBHs with higher mass can have a lifetime larger/comparable than the age of the Universe. Therefore, they have enough time to accrete mass and spin up [245]. In the present work, we consider the Hawking emission of PBHs into background radiations (photons and electron/positron) and provide the projected constraints on the fraction of dark matter in the form of PBHs ($f_{\rm PBH}$) as a function of mass and spin. We analyse projected bounds on spinning PBHs such that 21 cm differential brightness temperature does not change by more than a factor of 1/4 from the ΛCDM model prediction ($|T_{21}| \sim 220$ mK).

A rotating black hole with angular momentum $J_{\rm PBH}$ and having mass $M_{\rm PBH}$ can be defined with a rotation parameter, $a_* = J_{\rm PBH}/(G_{\rm N}\, M_{\rm PBH}^2)$ [233], where $G_{\rm N}$ is the gravitational constant. Rotating black hole with higher spin ($a_* \to 1$) injects more energy into IGM and evaporates faster than non-rotating ones [40, 229–231]. Therefore, we expect that the bounds on $f_{\rm PBH}$ to be more stringent compared to non-rotating PBHs. The energy injection per unit volume per unit time due to $e^{\pm}$ and photons into IGM, for monochromatic mass distribution of PBHs, can be written as [232, 246],

$$\Gamma^{e^{\pm}}_{\rm PBH}(z, a_*) = 2 \int \left[f_c^e(E - m_e, z)\, (E - m_e) \left(\frac{d^2 N_e}{dt\, dE} \right) \right] n_{\rm PBH}\, dE\,, \tag{3.3}$$

$$\Gamma^{\gamma}_{\rm PBH}(z, a_*) = \int \left[f_c^{\gamma}(E, z)\, E \left(\frac{d^2 N_\gamma}{dt\, dE} \right) \right] n_{\rm PBH}\, dE\,. \tag{3.4}$$

Energy injection into IGM happens by three processes: heating, ionization, and excitation of the gas [247–249]. f_c^i represents the energy deposition efficiency

into IGM. Here, c stands for above-mentioned three channels and $i \equiv$ (electron/positron, photon) stands for different types of injected particles. The factor of 2 in equation (3.3) accounts for the total contribution of electrons and positrons. $n_{\rm PBH} = f_{\rm PBH}\,(\rho_{\rm DM}/M_{\rm PBH})$ is the number density of the PBHs, and $\rho_{\rm DM}$ is the dark matter energy density. $d^2N^i/(dt\,dE) \equiv d^2N^i/(dt\,dE)\left(E, M_{\rm PBH}, a_*\right)$ represents the number of i particles emitted by black hole per unit time per unit energy [232, 233, 250, 251],

$$\frac{d^2N^i}{dt\,dE} = \frac{1}{2\,\pi}\sum_{\rm dof}\frac{\Gamma_i(E, M_{\rm PBH}, a_*)}{e^{E'/T_{\rm PBH}} \pm 1}\,, \tag{3.5}$$

here, Γ_i is the greybody factor— defines the probability of emitted particle i from black hole to overcome its gravitational potential well. dof represents the degree of freedom [251]. Moreover, E is the total energy of emitted particle i and $E' = E - n\Omega$. While, n is the axial quantum number and Ω is the angular velocity at black hole horizon. We use the `BlackHawk` code[b] to calculate the spectra due to photons, electrons and positrons; we take both the primary and secondary Hawking evaporation spectra into account— i.e. emitted final particle j per unit time and per unit energy [251, 252]

$$\frac{d^2N^j}{dt\,dE} = \sum_i \frac{d^2N^i}{dt\,dE''}\,\frac{dN^i_j}{dE}\,dE''\,, \tag{3.6}$$

here, dN^i_j is the hadronization table accounts for the transformation of the primary spectra into secondary spectra [251–253].

In the presence of Hawking radiation, the thermal evolution of the gas can be written as[157, 254],

$$\frac{dT_{\rm gas}}{dz} = 2\,\frac{T_{\rm gas}}{1+z} + \frac{\Gamma_c}{(1+z)\,H}(T_{\rm gas} - T_{\rm CMB}) - \frac{2\;\Gamma_{\rm PBH}}{3\,n_{\rm tot}(1+z)\,H}\,, \tag{3.7}$$

[b] https://blackhawk.hepforge.org/

here, $\Gamma_{\rm PBH} = \Gamma^{e^\pm}_{\rm PBH} + \Gamma^{\gamma}_{\rm PBH}$ is the total energy injection per unit time and per unit volume into IGM. We consider the following numerical values of the cosmological parameters: $h = 0.674$, $\Omega_{\rm M} = 0.315$, $\Omega_{\rm b} = 0.049$ and $T_{\rm CMB}|_{z=0} = 2.725$ K [48, 255]. To compute the energy deposition efficiency, thermal and ionization history of the Universe, we use `DarkHistory`[c] package with necessary modifications [249].

3.4 Results and Discussion

We take 21 cm differential brightness temperature such that it does not change, from its ΛCDM value ($\sim$ 220 mK), by more than a factor of 1/4 at redshift 17.2 . We solve the coupled equations (3.7) and (2.9— replacing $\mathcal{E}$ with $\Gamma_{\rm PBH}$) for different mass, spin and fraction of PBH dark matter to get $x_{\rm HI}$ and $T_{\rm gas}$ at redshift $z = 17.2$. To get any absorption signal in redshift range $15 - 20$, the gas temperature should be less than CMB temperature in shaded region— redshift range from 15 to 20. By requiring $T_{21} \simeq -150$ mK at z=17.2, we constrain the parameter space of PBH dark matter. In the present chapter, we do not consider x-ray heating of the gas due to the uncertainty in the physics of the first stars— as we discussed earlier. For a fix value of T_{21} at a redshift, if one includes the x-ray heating of gas, our projected upper constraints on PBH dark matter fraction becomes stronger. Here, it is to be noted that the gas temperature may increase due to the energy transfer from the background radiation to the thermal motions of the gas mediated by Lyα radiation from the first stars [34]. However, again due to the uncertainty in physics of the first star formation, we do not include this effect also. The inclusion of this effect will also further strengthen our projected upper bounds on $f_{\rm PBH}$— similar to discussed in chapter (2).

In order to understand how spin, fraction and mass of PBH dark matter can affect the thermal evolution of the gas, we plot the figures (3.1), (3.2) and (3.3), respectively. The shaded region corresponds redshift range, $15 - 20$. The red

[c] https://darkhistory.readthedocs.io/en/master/

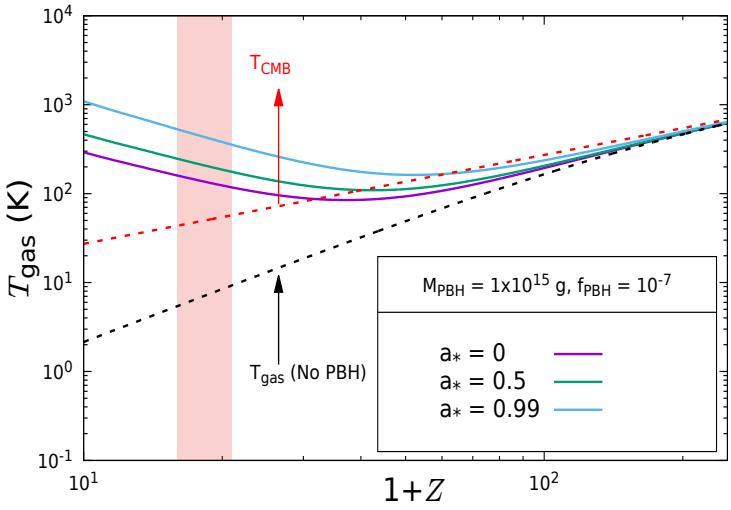

Figure 3.1: The gas temperature evolution with redshift for evaporating primordial black hole. The red dashed lines represent the CMB temperature evolution. The black dashed lines depicts the $T_{\rm gas}$ when there is no PBHs. The shaded region corresponds to the redshift $15 \leq z \leq 20$ (EDGES observed signal). In this figure, we consider PBHs mass and $f_{\rm PBH}$ to 1×10^{15} g and 10^{-7}, respectively, and vary the spin of PBHs.

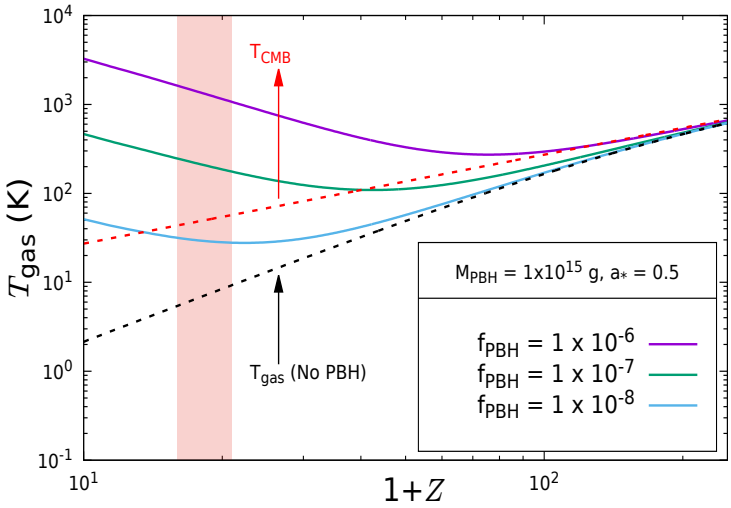

Figure 3.2: The caption is the same as in Figure (3.1), except here, we keep $M_{\rm PBH} = 1 \times 10^{15}$ g and $a_* = 0.5$ constant and vary $f_{\rm PBH}$.

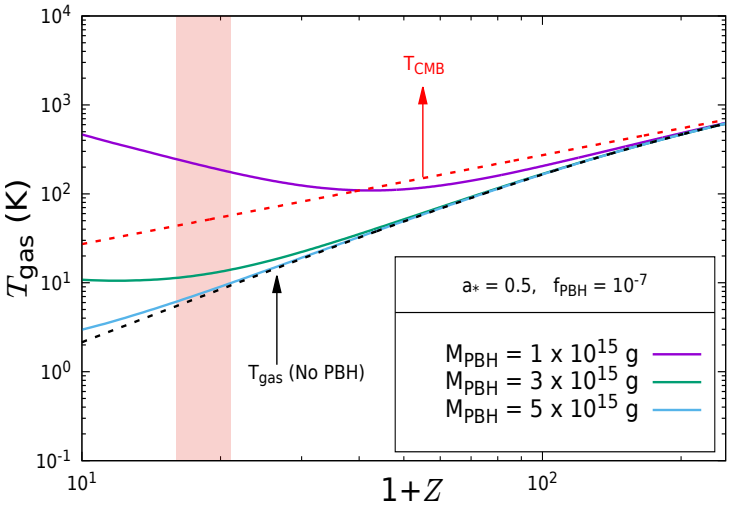

Figure 3.3: The caption is the same as in Figure (3.1), except here, we vary the mass of PBHs and keep spin and $f_{\rm PBH}$ to 0.5 and 10^{-7}, respectively.

dashed curves in all plots depict the CMB temperature evolution, while the black dashed line represents the gas temperature when there are no evaporating PBHs. In Figure (3.1), we keep mass to 1×10^{15} g and $f_{\rm PBH} = 10^{-7}$, and vary the spin of PBHs. As expected, when we increase the spin of PBHs, the gas temperature rises significantly in the shaded region. The solid violet curve represents the case when the spin of PBHs is 0. Increasing the spin to 0.5 (solid green line), the gas temperature increases. Further increasing a_* to 0.99 (solid cyan line), the gas temperature rises further. In Figure (3.2), we keep $M_{\rm PBH} = 1 \times 10^{15}$ g, spin to 0.5 and vary $f_{\rm PBH}$. In this plot, as we increase the $f_{\rm PBH}$ from 10^{-8} (solid cyan line) to 10^{-6} (solid violet line), the IGM heating rises rapidly. If the gas temperature becomes larger than the CMB temperature in the shaded region, it can erase the 21 cm absorption signal; instead, it may give an emission signal. Therefore, at desired redshift (in our scenario $z = 17.2$), one has to keep $T_{\rm gas} < T_{\rm CMB}$ to get an absorption signal. Increasing $f_{\rm PBH}$, for a given mass, the number density of PBHs increases resulting in more energy injection into IGM by Hawking evaporation of PBHs. Therefore, $f_{\rm PBH}$ plays a significant role in deciding whether one gets an

absorption profile or emission. In Figure (3.3), we vary the mass of PBHs and keep spin and $f_{\rm PBH}$ constants to 0.5 and 10^{-7}, respectively. In this plot, as we increase the mass of PBHs from 1×10^{15} g (solid violet line) to 5×10^{15} g (solid cyan line), the gas temperature decreases. It happens for two reasons: (i) Increasing the mass of PBHs leads to a decrease in the total power contributions from Hawking evaporation of PBHs [250]. (ii) Ignoring the integral dependency in equations (3.3) and (3.4), $\Gamma^{e^{\pm}}_{\rm PBH}$ and $\Gamma^{\gamma}_{\rm PBH}$ are proportional to $n_{\rm PBH} = f_{\rm PBH}\,(\rho_{\rm DM}/M_{\rm PBH})$. For a fixed dark-matter energy density and $f_{\rm PBH}$, the number density of PBHs increases by decreasing the black hole mass. Thus, energy injection into IGM per unit volume and time ($\Gamma_{\rm PBH}$) increases, and one gets more heating of the gas.

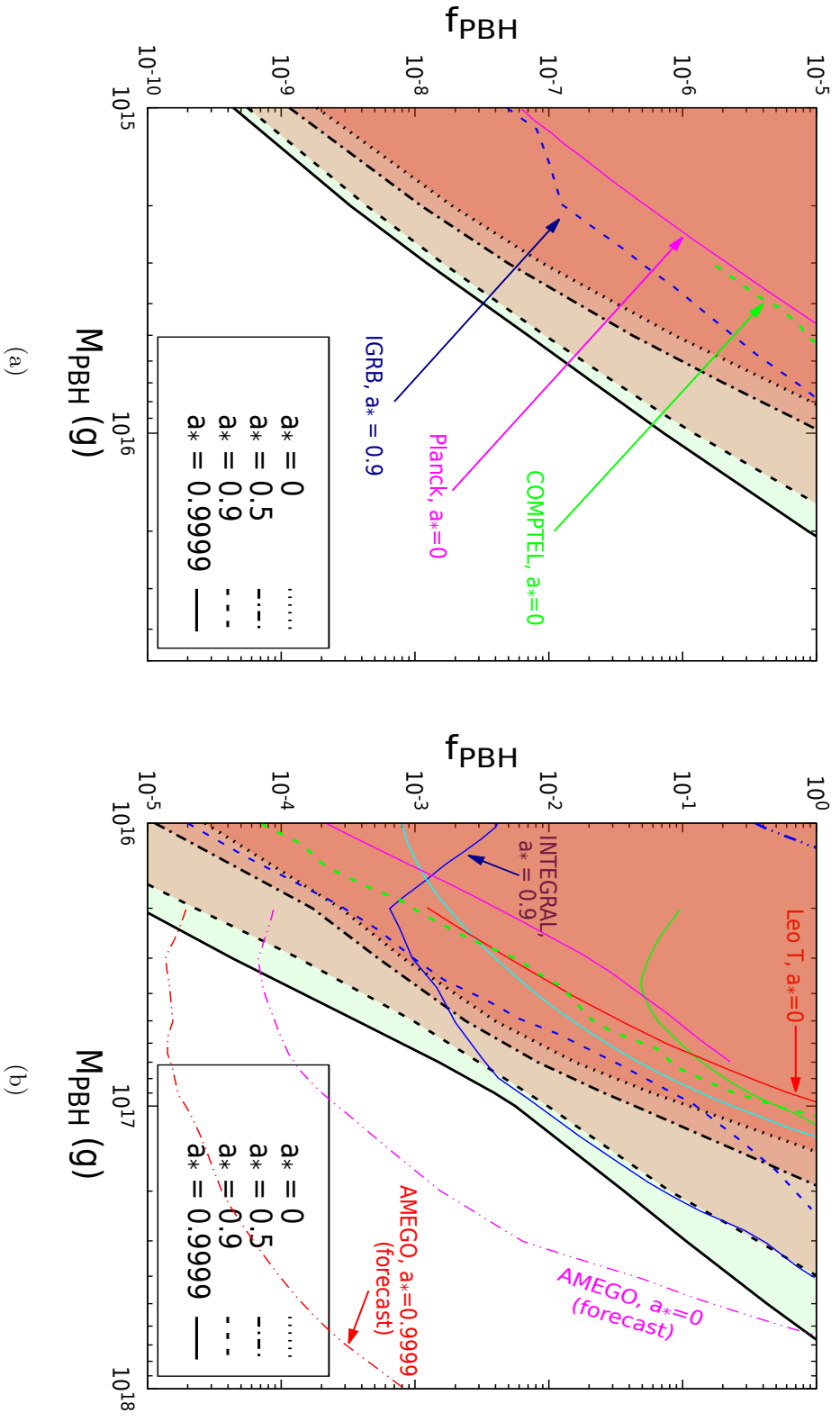
(a)
f_{PBH}
M_{PBH} (g)
IGRB, a* = 0.9
Planck, a*=0
COMPTEL, a*=0
a* = 0
a* = 0.5
a* = 0.9
a* = 0.9999
(b)
f_{PBH}
M_{PBH} (g)
INTEGRAL, a* = 0.9
Leo T, a*=0
AMEGO, a*=0.9999 (forecast)
AMEGO, a*=0 (forecast)
a* = 0
a* = 0.5
a* = 0.9
a* = 0.9999

Figure 3.4 (previous page): The projected upper bounds on the dark fraction of matter in the form PBHs ($f_{\rm PBH} = \Omega_{\rm PBH}/\Omega_{\rm DM}$) as a function of PBHs mass for different values of a_*. The shaded regions are excluded from our analysis for $f_{\rm PBH}$ when $a_* = 0$ (dotted black line), 0.5 (dot-dashed black line), 0.9 (dashed black line) and 0.9999 (solid black line). The dashed blue curve depicts the upper constraint on $f_{\rm PBH}$ by observations of the diffuse Isotropic Gamma-Ray Background (IGRB) for $a_* = 0.9$ [40]. The double-dot-dashed blue curve represents the upper constraint on $f_{\rm PBH}$ from Diffuse Supernova Neutrino Background (DSNB) searches at Super-Kamiokande, while the solid blue line represents the INTErnational Gamma-Ray Astrophysical Laboratory (INTEGRAL) observation of 511 KeV γ-ray lines at Galactic centre constraint on $f_{\rm PBH}$ for $a_* = 0.9$ [41]. The double-dot-dashed magenta (red) line represents the AMEGO forecast for $a_* = 0$ ($a_* = 0.9999$) [42]. Near future, AMEGO collaboration will be able to probe the parameter-space above the magenta (red) double-dot-dashed curve for $a_* = 0$ ($a_* = 0.9999$). The solid green line stands for 95% confidence level bound from INTEGRAL observation of Galactic gamma-ray flux for non-spinning PBHs [43]. Solid cyan curve depicts the upper bound from observing the 511 KeV γ-ray lines at the Galactic centre by assuming all the PBHs within a 3 Kpc radius of the Galactic centre for non-spinning PBHs [44]. The magenta solid line represents the Planck constraint [45]. The red solid line depicts the dwarf galaxy Leo T constraint [46] and the green dashed line shows the COMPTEL bound [47] for non-spinning PBHs.

In Figure (3.4), we plot the upper projected bounds on the fraction of dark matter in the form of PBHs as a function of PBHs mass for different spins. Here, we have considered that 21 cm differential brightness temperature, T_{21}, remains -150 mK at redshift $z = 17.2$. We vary the mass of PBHs from 10^{15} g to 10^{18} g. The shaded regions in both the plots are excluded for the corresponding PBH spins. The dashed blue curve represents the upper constraint on $f_{\rm PBH}$ by observations

of the diffuse Isotropic Gamma-Ray Background (IGRB) [40]. The double-dot-dashed blue curve represents the upper constraint on $f_{\rm PBH}$ from Diffuse Supernova Neutrino Background (DSNB) searches at Super-Kamiokande, while the solid blue line represents the INTErnational Gamma-Ray Astrophysical Laboratory (INTEGRAL) observation of 511 KeV γ-ray line at Galactic centre constraint on $f_{\rm PBH}$ for $a_* = 0.9$ [41]. For $a_* = 0$, the observation at the Jiangmen Underground Neutrino Observatory (JUNO) will be able to place a 20 times stronger bound on the upper allowed value of $f_{\rm PBH}$ for $M_{\rm PBH} = 10^{15}$ g compared to Super-Kamiokande [41, 256]. The double-dot-dashed magenta (red) line represents the AMEGO forecast for $a_* = 0$ ($a_* = 0.9999$) [42]. In the near future, AMEGO collaboration will be able to probe the parameter-space above the magenta (red) double-dot-dashed curve for $a_* = 0$ ($a_* = 0.9999$). Solid green line stands for 95% confidence level bound from INTEGRAL observation of Galactic γ-ray flux for non-spinning PBHs [43]. The solid cyan curve depicts the upper bound from the observation of 511 KeV γ-ray lines at the Galactic centre by assuming all the PBHs within a 3 Kpc radius of the Galactic centre for non-spinning PBHs [44]. For the comparison, we have also plotted the bounds from Planck [45], Leo T [46] and COMPTEL [47] observations for non-spinning PBHs. In Figure (3.4a), $f_{\rm PBH}$ varies from 1×10^{-10} to 1×10^{-5}, while, in Figure (3.4b), it varies from 1×10^{-5} to its maximum allowed value 1 ($\Omega_{\rm PBH} = \Omega_{\rm DM}$). In Figure (3.4), as we increase the value of spin from 0 to its extremal value, 0.9999, the upper bounds become more stringent. This is due to an increment in evaporation of PBHs, and it results in more energy injection into the IGM [233, 257, 258]. As discussed earlier, increasing the mass of PBHs, energy injection into IGM decreases. Subsequently, one gets more window to increase the gas temperature or $f_{\rm PBH}$, and the upper bound becomes weaker. Therefore, in Figure (3.4), the upper bound on $f_{\rm PBH}$ weakens as we increase the mass. Our upper projected constraint on $f_{\rm PBH}$ for $a_* = 0.9$ is comparable to the INTEGRAL observation of 511 KeV γ-ray lines for PBHs mass larger than $\sim 8 \times 10^{16}$ and becomes stronger for smaller PBH masses. Also, compared to IGRB [40] and

DSNB [41], our projected bounds are stringent for the considered mass range of PBHs. We find the most robust lower projected constraint on the mass of PBHs, which is allowed to constitute the entire dark matter, to 1.5×10^{17} g, 1.9×10^{17} g, 3.9×10^{17} g and 6.7×10^{17} g for PBH spins 0, 0.5, 0.9 and 0.9999, respectively. The lower bound on $M_{\rm PBH}$ for $\Omega_{\rm PBH} = \Omega_{\rm DM}$, for extremal spinning PBHs is nearly four times larger than non-spinning PBHs.

3.5 Conclusions

Spinning primordial black holes can substantially affect the ionization and thermal history of the Universe. Subsequently, it can modify the 21 cm absorption signal in the cosmic dawn era by injecting energy due to Hawking evaporation. We study the upper projected bounds on the fraction of dark matter in the form of PBHs as a function of mass and spin, considering that the 21 cm differential brightness temperature does not change by more than a factor of 1/4 from the theoretical prediction based on the ΛCDM framework. Our projected constraints are stringent compared to DSNB, INTEGRAL observation of the 511 KeV line, IGRB, Planck, Leo T and COMPTEL. In the near future, AMEGO collaboration will be able to probe some parameter space in our considered mass range of PBHs. In the present work, we have considered the monochromatic mass distribution of PBHs. The allowed parameter space can also be explored for different PBHs mass distributions such as log-normal, power-law, critical collapse, etc. [251]. Here, it is to be noted that we have not considered heating of IGM gas due to x-ray from the first stars in the vague of known physics of the first stars. For a fix value of T_{21} at a redshift, if one includes the x-ray heating of the gas, the projected bounds becomes stronger.

3.6 Additional study

3.6.1 Bounds in light of varying T_{21} and redshift

We also study upper projected bounds on the fraction of the dark matter in the from of PBHs by varying the amplitude of 21 cm differential brightness temperature and redshift. In figure (3.5), we have plotted upper bounds on the fraction of dark matter in the form of primordial black holes as a function of mass for various values of T_{21} at $z = 17$. To understand that how bounds change on $f_{\rm PBH}$ with T_{21}, we consider two scenarios for the spin of PBHs: $a_* = 0$ (figure 3.5c) and $a_* = 0.9$ (figure 3.5d). In both of the plots, we notice that when we change the value of T_{21} from -200 mK to -150 mK the bound relaxes with a factor of ~ 4.3 . By changing the T_{21} from -150 mK to -100 mK bounds relax by a factor of ~ 2.3, and, going from -100 mK to -50 mK the bounds relax by a factor of ~ 2.25. By changing the T_{21} from -50 mK to 0, bounds relax by a factor of ~ 3.1 . This similar pattern

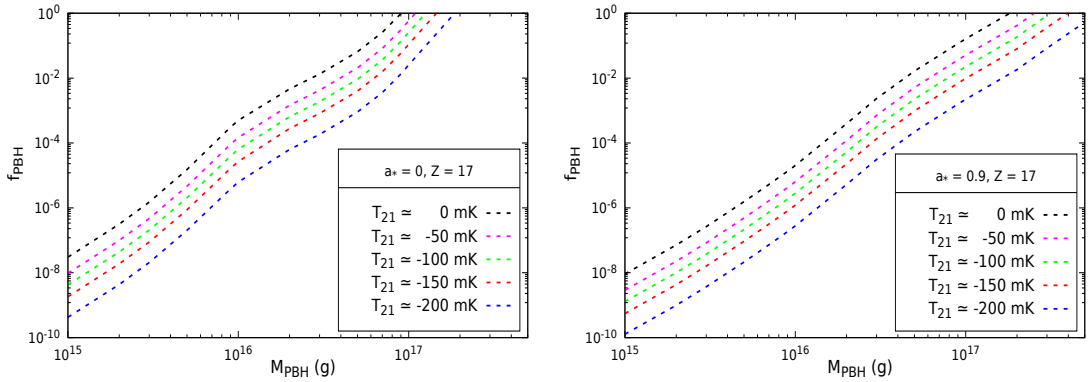

(c) (d)

Figure 3.5: The plots represent the upper projected bounds on the fraction of dark matter in the form of primordial black holes ($f_{\rm PBH}$) as a function of mass of PBHs ($M_{\rm PBH}$) for varying 21 cm differential brightness temperature (T_{21}) at $z = 17$. Figure (3.5c) represents the case when spin of PBHs: $a_* = 0$, while, figure (3.5d) represents the case with $a_* = 0.9$.

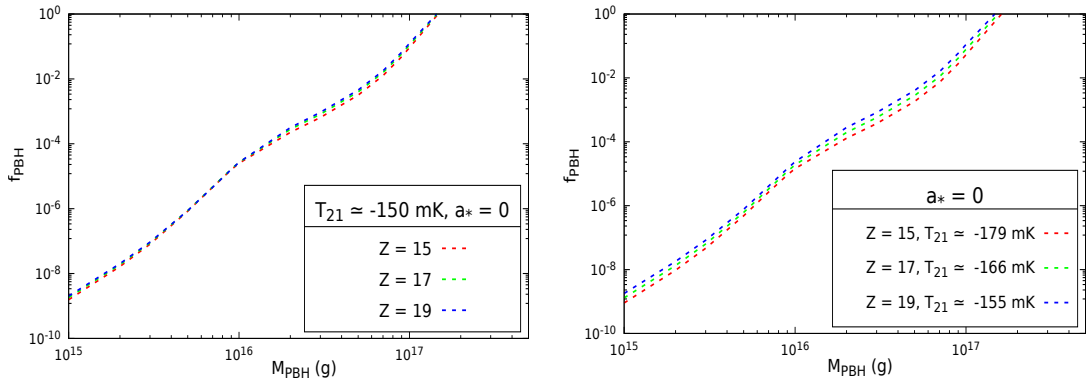

(a) (b)

Figure 3.6: Figure (3.6a) represents upper projected bounds on $f_{\rm PBH}$ when $T_{21} \simeq -150$ mK for different values of redshift (z). Figure (3.6b) represents upper bounds on $f_{\rm PBH}$ when T_{21} does not change more than a factor of 1/4 from the minimum possible amplitude based on ΛCDM model for corresponding values of redshift ($T_{21}^{\rm Min}(z = 15) \simeq -238$ mK, $T_{21}^{\rm Min}(z = 17) \simeq -221.2$ mK and $T_{21}^{\rm Min}(z = 19) \simeq -207$ mK). Here, the cosmological parameters are: $h = 0.674$, $\Omega_{\rm M} = 0.315$, $\Omega_{\rm b} = 0.049$ [48]. Both figures obtained for $a_* = 0$.

also occurs for the case of sterile neutrinos and the factors remain same. Therefore, we can also find the constraints on $f_{\rm PBH}$ for other values of spin when the bound on $f_{\rm PBH}$ is given for any value of $T_{21} \in \{0, -50, -100, -150, -200\}$ mK.

In figure (3.6a), similarly to sterile neutrino case, we see that bounds do not change significantly for a fix value of T_{21} at different values of redshift. In figure (3.6b), upper bounds on $f_{\rm PBH}$ are obtained such that T_{21} does not change more than a factor of 1/4 from the minimum possible amplitude based on ΛCDM model for corresponding values of redshift. In this chapter, we consider the following numerical values of the cosmological parameters: $h = 0.674$, $\Omega_{\rm M} = 0.315$, $\Omega_{\rm b} = 0.049$ and $T_{\rm CMB}|_{z=0} = 2.725$ K [48, 255]. Therefore, we get minimum possible value of T_{21} based on ΛCDM model to -238 mK at $z = 15$, -221.2 mK at $z = 17$ and -207 mK at $z = 19$.

"Astronomy and Pure Mathematics are the magnetic poles toward which the compass of my mind ever turns."

Carl Friedrich Gauss, *In Letter to Bolyai (30 Jun 1803)*

4

Primordial Magnetic Fields and Excess Radio Background

Observations suggest that the magnetic fields are ubiquitous in the Universe—from the length scale of planets and stars to the cluster of galaxies [17–20]. Fermi[a] and High Energy Stereoscopic System (HESS)[b] gamma-ray observation suggests that even voids could host magnetic fields with strength $\mathcal{O}(10^{-16}$ G) with a typical coherent scale of Mpc [21, 22]. Magnetic fields can also play a significant role in reionization, relic electron density and structure formation [259]. The presence of magnetic fields can substantially affect the evolution and dynamics of structures in the Universe as they can contribute to the total pressure against gravitational collapse. This could modify the total matter power spectrum on small scales,

[a] https://fermi.gsfc.nasa.gov/
[b] https://www.mpi-hd.mpg.de/hfm/HESS/

$\lesssim$ 1 Mpc [259–264]. The presence of magnetic fields during recombination can also have important consequences, such as it could have lead to the collapse of gas clouds after recombination, formation of first pre-galactic stars, quasars [265]. The Earth has a magnetic field of the order of $\mathcal{O}$(G), and it is sustained for years by some dynamo mechanism. Similarly, other astronomical objects near to Earth, such as Sun and other solar system planets, also show the presence of magnetic fields [266]. Our home galaxy Milky Way, other spiral galaxies and their interstellar medium (ISM) contain magnetic fields with the strength $\mathcal{O}(\mu\text{G})$ [261, 264, 266–268]. Moreover, galaxy clusters, intercluster medium, filaments, IGM, etc., also show the magnetic fields [19, 21, 269–271]. These magnetic fields are likely to be seeded by primordial magnetic fields (PMFs). These PMFs might have originated in the very early Universe, and subsequently amplified in the small scale structures by some mechanisms [21, 24].

4.1 Generation of primordial magnetic fields

The origin and evolution of PMFs is one of the outstanding problems of modern cosmology (Ref. [23, 24] and references cited therein). It would be very difficult to explain the magnetic fields in the voids and high redshift galaxies with only late-time astrophysical processes without magnetic fields from the very early Universe. Therefore, these magnetic fields indeed may have a primordial origin [21, 272–274]. There are several theoretical models that can generate the magnetic field in the early Universe with a large coherent scale. The two scenarios to generate PMFs that are vastly discussed in the literature are phase transitions in the early Universe and various models of inflation (for details, see the recent review [24]). In the Ref. [275], the authors discuss how the inflation model can generate large scale, $\sim \mathcal{O}$(Mpc), magnetic fields. The generated magnetic fields have a small strength. To amplify the field, one has to break the conformal invariance of the electromagnetic field. The authors consider three mechanisms to break the con-

formal invariance: Coupling of the photon to the axions, gravitational field and massless-charged-nonconformally invariant scalar field [275]. Authors of the Ref. [276], extend the inflation model by introducing the coupling between the Maxwell field and the scalar field (Φ) responsible for inflation ($\propto e^{\alpha\Phi}F_{\mu\nu}F^{\mu\nu}$), here, $F_{\mu\nu}$ is the electromagnetic field tensor. This scenario can generate magnetic fields with a present-day strength up to nG with the coherence scale of a few Mpc depending on the parameter α. A similar mechanism to generate the magnetic fields during inflation is based on the superstring cosmology [277, 278]. The Lagrangian, similar to considered by [276] with $\alpha = -1$, naturally arises from the effective action in low-energy string theory. Here, inflation is driven by the kinetic part of the dilaton scalar field— Φ'. Whereas in the article [276], it is driven by the false vacuum scalar field potential— which is too steep for producing the slow-roll inflation [272, 277]. In the article [279], authors argue that the back reaction of generated magnetic fields via inflation can spoil the inflation. Considering the backreaction, the authors put an upper bound on the present-day strength of magnetic fields to 10^{-32} G on the Mpc scale. This strength seems too small for galactic dynamos to amplify to explain the observed magnetic fields. In the recent article [280], it is shown that this issue can be circumvented for some parameter space. The authors find that magnetic fields with a present-day strength of $\sim 10^{-13}$ G with a scale of Mpc can be generated while keeping the backreactions under control. Magnetic fields can also arise during electroweak [281] and quantum-chromo-dynamics [282] phase transitions. Other mechanisms include cosmic strings [283, 284], primordial plasma vorticity [285], etc. In this chapter, we obtain the upper bounds on present-day strength of PMFs for various values of spectral index in the light of EDGES[c] observation and excess radio background observed by the ARCADE 2 & LWA 1 observation [25]. Here, we obtain the bounds on PMFs in both the presence and absence of heating effects due to first stars.

[c]Recently, the EDGES signal has been questioned in many articles. We discuss this point in chapter (6).

4.2 Existing bounds on primordial magnetic fields

The present-day strength, spectral index and coherence scale of PMFs depends on their generation mechanisms. Therefore, the constraints on PMFs can give a hint of the early Universe physics. Recently in the Ref. [286], authors show that PMFs can be used as a remedy to resolve the Hubble tension between different observations. The present-day amplitude of PMFs is constrained from the BBN, formation of structures and temperature anisotropies & polarization of CMB [259, 287, 288]. Authors of the Ref. [50], put an upper constraint to $\sim 10^{-10}$ G on 1 Mpc scale by considering $T_{\rm gas} \lesssim T_{\rm CMB}$ (i.e. $T_{21} \lesssim 0$) so that, PMFs can not erase the T_{21} absorptional signal in the redshift range $15 \lesssim z \lesssim 20$. Planck 2015 results put individual upper constraints of the $\mathcal{O}$(nG) for different cosmological scenarios on 1 Mpc scale [49]. The authors of the Ref. [289], in the context of EDGES observation, put an upper and lower constraint on the PMFs to be 6×10^{-3} nG and 5×10^{-4} nG respectively. Also, the lower bound on the present-day strength of PMFs found in Refs. [290–292]. Further, in the Ref. [21], authors put a lower bound on the strength of intergalactic magnetic fields of the order of 3×10^{-16} G using Fermi observations of TeV blazars. Authors of the reference [293], report upper bound of 2×10^{9} G at the end of BBN. Presence of PMFs can modify the present-day relic abundance of He^4 and other light elements. Therefore, magnetic fields can be constrained by observations of light element abundances [259, 294–297]. The authors of the Ref. [298], put an upper bound of 47 pG for scale-invariant PMFs by comparing CMB anisotropies, reported by the Wilkinson Microwave Anisotropy Probe (WMAP) and Planck, with calculated CMB anisotropies.

4.3 Evolution of PMFs after recombination

The generation of the magnetic fields in the early Universe for the various cosmological scenarios has been studied in the earlier literature (for example see Refs.

[272, 282, 290, 299, 300]). It is to be noted that decaying magnetic fields has been studied in several literatures. In these works, the authors consider the decay of the PMFs by ambipolar diffusion and turbulent decay [26, 50, 254, 259, 301]. Ambipolar diffusion of magnetic fields is important in neutral medium as it is inversely proportional to free-electron fraction (x_e) and $x_e \sim 10^{-4}$ after redshift $z \lesssim 100$ [160, 254, 259]. The presence of PMFs can induce the Lorentz force in the gas. The force exerts only on free electrons and ions leaving the neutral components unaffected. This can result in creating a velocity difference between charged and neutral components. The velocity difference can enhance the collision frequency in the gas, resulting in a dissipation of magnetic energy into the gas— known as the ambipolar diffusion of magnetic fields [302]. After the recombination ($z \sim 1100$), the radiative viscosity of fluid dramatically decreases, and velocity perturbations are no longer damped. Therefore, the tangled magnetic fields having length scale smaller than the magnetic Jeans length can dissipate via another mode— turbulent decay [254, 259, 303]. Magnetic heating of the gas due to the turbulent decay decreases with redshift but later when ionization fraction decreases, heating increases due to ambipolar diffusion [254, 259]. We further discuss about the ambipolar and turbulent decay in section (4.5). Decaying PMFs can inject magnetic energy into the thermal energy of the IGM and heat the gas above 6.7 K at $z = 17$, and even it can erase the EDGES absorption signal [50, 254, 259]. Still, the EDGES absorption signal can be explained by considering the possible early excess of radio radiation [304].

4.4 Background excess radio radiation

The Absolute Radiometer for Cosmology, Astrophysics and Diffuse Emission (ARCADE 2) collaboration[d], a double-nulled balloon-borne instrument with seven radiometers, measured the absolute sky temperature in a frequency range of 3 –

[d] https://asd.gsfc.nasa.gov/archive/arcade/

90 GHz. The observation reported excess radio radiation in a frequency range of $3 - 10$ GHz [27],

$$T(\nu) = T_0 + T_r \, (\nu/\nu_0)^{\beta} \,, \tag{4.1}$$

here, ARCADE 2 observation fitted the parameters as: $T_0 = 2.731 \pm 0.004$ K, $\beta = -2.6$, $T_r = 21.1 \pm 3.0$ K and $\nu_0 = 310$ MHz. By combining ARCADE 2 with the Low-frequency data [305–308] and Far Infrared Absolute Spectrophotometer (FIRAS) data [309], the parameters can be fitted as: $T_0 = 2.725 \pm 0.001$ K, $\beta = -2.599 \pm 0.036$, $T_r = 24.1 \pm 2.1$ K and $\nu_0 = 310$ MHz in a frequency range of 22 MHz$-$10 GHz [27]. This is measured at present-day ($z = 0$). The radiation temperature maps with redshift as: $\propto (1 + z)$, we can multiply $T(\nu)$ with $(1 + z)$ for past [304, 310–314],

$$T(z) = T_0 \, (1 + z) \left[1 + \frac{T_r}{T_0} \left(\frac{78}{310} \right)^{\beta} \times \left(\frac{\nu}{78 \text{ MHz}} \right)^{\beta} \right] . \tag{4.2}$$

This radiation is several times larger than the observed radio counts due to the known Galactic and extragalactic radio processes and sources, such as star-forming galaxies, AGN-driven sources— quasars and radio galaxies, etc. [28, 29]. The presence of early excess radiation can not be completely ruled out at the time of cosmic dawn. For example, in the redshift range $z \approx 30$ to 16, accretion onto the first intermediate-mass black holes can produce a radio radiation [315]. Accreting supermassive black holes [316] or supernovae [317] can also produce radio background due to synchrotron emission at the time of cosmic down by accelerated electrons in the presence of the magnetic field. The enhancement in the background radiation is also supported by the first station of the Long Wavelength Array (LWA 1)[e] in frequency range $40 - 80$ MHz. The excess observed by LWA 1 can also be fitted by the same model given by equation (4.1). After the inclusion of LWA

[e] https://leo.phys.unm.edu/ lwa/

1 data with ARCADE 2 [27] and Low-frequency data [305–308], the parameters change as: $T_0 = 2.722 \pm 0.022$ K, $\beta = -2.58 \pm 0.05$ and $T_r = 30.4 \pm 2.6$ K at $\nu_0 = 310$ MHz [30, 318]. For the observation of 21-cm signal, we can write: $\nu = 1420.4/(1+z)$ MHz. In the equation (4.2), the factor of $(\nu/78 \text{ MHz})^\beta$ can be defined as a fraction of excess radio background, A_r. Depending on the origin, A_r can have different values— we discuss about this more in next sections. Therefore, in the final analysis, we vary the value of excess radiation fraction.

4.4.1 Excess radiation during the cosmic dawn

In this work, we use the EDGES signal in the presence of excess radio radiation to constrain the strength of PMFs. Some of the processes which we have discussed responsible for the excess radio background can occur at earlier redshift ($z \sim 17$) [315–317]. Also, one of the interesting proposals in the Ref. [304] is to argue that such a possibility can exist at the time of cosmic dawn, and it can help to explain the EDGES signal. Here, authors show that the EDGES absorption signal can be explained by having only 10 percent of the observed radio background by ARCADE 2. In Ref. [319, 320], the authors claim that thermal emission from the axion quark nugget dark matter model can explain the EDGES signal, and it can also contribute a fraction of the radiation excess observed by ARCADE 2. At present, there exist several theoretical models to explain this excess at the time of cosmic dawn. The stimulated emission from Bose stars can give a large contribution to the radio background and explain the EDGES and ARCADE 2 observations [321]. The radio emission from accreting Pop III black holes can produce the EDGES like signal by increasing background radiation temperature [322]. In other scenarios, the EDGES anomaly can be explained by axion-photon conversion in the presence of intergalactic magnetic fields [323] or by radiative decays of standard model neutrino induced by magnetic fields [324]. Radio excess can also be explained by the cusp region of superconducting cosmic strings [325]. In ref. [326], authors

consider radiative decays of relic neutrino and show that it can potentially explain the ARCADE 2 excess together with the EDGES signal. Depending on the origin, the excess fraction of radio radiation can have a different value. We discuss the constraints on excess radiation later. Considering the above possibilities of having early excess radiation, we believe that it is important to analyze constraints on the primordial magnetic field in the presence of such radiation.

4.4.2 Phenomenological model for excess radiation

As discussed in subsection (4.4.1), the possibility of an excess radio radiation background over the CMBR can not be denied. For the excess radio background, we consider the phenomenological model following the Ref. [310–314]. Here, Authors consider a uniform redshift-independent synchrotron-like radiation, motivated by the ARCADE 2 and LWA 1 observations. This model can explain the EDGES anomaly in addition to enhancement of cosmic down power spectrum. Accordingly, from equation (4.2) and following the Refs. [310–314],

$$T_R = T_0\,(1+z)\left[1 + A_r\left(\frac{\nu_{\rm obs}}{78\ {\rm MHz}}\right)^{\beta}\right], \tag{4.3}$$

where, $T_0 = 2.725$ K is the present day CMB temperature and $\beta = -2.6$ is the spectral index. Here, A_r is the amplitude defined relative to the CMB at reference frequency of 78 MHz. For the 21 cm signal $\nu_{\rm obs}$ is $1420.4/(1+z)$ MHz. Authors of the Ref. [310], put a limit on the excess radiation background to $1.9 < A_r < 418$ at reference frequency of 78 MHz by considering the effect of an uniform radiation excess on the 21 cm signal from the cosmic dawn, dark ages and reionization. Authors consider a synchrotron-like spectrum with spectral index -2.6 . The case with $A_r \sim 418$ corresponds to the LWA 1 limit on A_r at the reference frequency of 78 MHz [30, 310]. The stringent constraint on excess radiation comes from the Low-Frequency Array (LOFAR) to $A_r < 182$ (95 percent CL) and $A_r < 259$ (99 percent CL) for a spectral index of -2.6 [313].

4.5 Impact on the thermal and ionization history due to primordial magnetic fields

In the presence of decaying magnetic fields, the gas temperature can increase. $T_{\rm gas}$ can even increase above the background radiation and can erase the 21 cm absorption signal reported by EDGES [50, 254, 259, 303]. Therefore, present-day PMFs strength can be constrained by the EDGES observation in the presence of excess radiation reported by ARCADE 2 and LWA 1 [5, 27, 30, 304, 310, 327]. In the presence of turbulent decay and ambipolar diffusion, the thermal evolution of the gas with the redshift can be written as [254, 259, 302, 303, 328],

$$\frac{dT_{\rm gas}}{dz} = 2\,\frac{T_{\rm gas}}{1+z} + \frac{\Gamma_c}{(1+z)\,H}(T_{\rm gas} - T_{\rm CMB}) - \frac{2}{3\,n_{\rm tot}(1+z)\,H}(\Gamma_{\rm turb} + \Gamma_{\rm ambi})\,, \tag{4.4}$$

Here, $f_{\rm He} = 0.079$ and $T_{\rm CMB} = T_0\,(1+z)$ is the cosmic microwave background (CMB) temperature. At early times, $T_{\rm gas}$ remains in equilibrium with CMB temperature due to Compton scattering. However, the gas temperature will not be strongly affected by the comparatively small amount of energy in the non-thermal radio radiation. Therefore, $T_{\rm gas}$ and T_α can be assumed independent of the excess radiation [304]. The change in the free electron fraction (x_e) with redshift is given by equation (2.9) with $\mathcal{E} = 0$. Heating rate per unit volume due to the ambipolar diffusion ($\Gamma_{\rm ambi}$) and turbulence decay ($\Gamma_{\rm turb}$) is given by [254, 259],

$$\Gamma_{\rm ambi} = \frac{(1-x_e)}{\gamma\,x_e\,(M_{\rm H}\,N_b)^2}\,\frac{|(\boldsymbol{\nabla}\times\boldsymbol{B})\times\boldsymbol{B}|^2}{16\,\pi^2}\,, \tag{4.5}$$

$$\Gamma_{\rm turb} = \frac{1.5\;m\;\;[\ln(1+t_i/t_d)]^m}{[\ln(1+t_i/t_d) + 1.5\ln\{(1+z_i)/(1+z)\}]^{m+1}}\,H\,E_B\,, \tag{4.6}$$

here, $m = 2(n_B+3)/(n_B+5)$, $z_i = 1088$ is the redshift when heating starts due the magnetic fields (recombination epoch), $\gamma = 1.9\times10^{14}\,(T_{\rm gas}/{\rm K})^{0.375}{\rm cm}^3/{\rm g/s}$ is

the coupling coefficient, $M_{\rm H}$ is the mass of hydrogen atom and N_b is the number density of baryons. $t_d = 1/\big(k_d\, V_A(k_d, z)\big)$ is the decay time for the turbulence. For matter dominated era, $t_i = 2/\big(3\, H(z_i)\big)$ and $V_A(k_d, z) = B(k_d, z)/\big(4\,\pi\,\rho_b(z)\,\big)^{1/2}$ is the Alfvén wave velocity. $B(k_d, z)$ is the magnetic field strength smoothed over the scale of k_d at redshift z. k_d is constrained by the damping wavenumber of Alfvén wave. PMFs with wavenumber (k) larger than k_d, are strongly damped by the radiative-viscosity [259, 303, 329–332]. Moreover, $E_B = B^2/(8\pi)$ is the magnetic field energy density,

$$\frac{dE_B}{dz} = 4\,\frac{E_B}{1+z} + \frac{1}{H\;(1+z)}\;\left(\,\Gamma_{\rm turb} + \Gamma_{\rm ambi}\,\right). \tag{4.7}$$

Here, we assume that PMFs are isotropic and homogeneous Gaussian random magnetic field, whose power spectrum is given by the following equation [50, 259, 262, 333]

$$\langle \tilde{\mathbf{B}}_i(\mathbf{k})\,\tilde{\mathbf{B}}^*_j(\mathbf{q})\rangle = \frac{(2\pi)^3}{2}\delta^3_D(\mathbf{k}-\mathbf{q})\left(\delta_{ij} - \frac{k_i k_j}{k^2}\right) P_B(k)\,, \tag{4.8}$$

here, $P_B(k)$ is the magnetic power spectrum, $k = |\mathbf{k}|$ is the comoving wave number and δ_D is the Dirac delta function. Here, we consider a power-law spectrum of the magnetic fields in the Fourier space for $k < k_d$ [50],

$$P_B(k) = \frac{(2\pi)^2}{\Gamma\big[(n_B+3)/2\big]}\;B_0^2\;\left(\frac{k}{\rm Mpc^{-1}}\right)^{n_B}\;{\rm Mpc}^3\,. \tag{4.9}$$

Here, n_B is the spectral index. In particular, $n_B = 2$ for white noise [265], $n_B = 4$ for the Batchelor spectrum [334] and $n_B = -2.9$ for nearly scale invariant spectrum [259]. As discussed above, magnetic fields are strongly damped by the large radiative-viscosity for wavenumber larger than k_d before recombination. Therefore, we consider a sharp cut-off for power spectrum of PMFs: $P_B(k) = 0$ for $k \geq k_d$ [50]. Following the Ref. [50], we take the time evolution of the Alfvén wave damping scale: $k_d(z) = k_{d,\rm i}\, f(z)$ and $f(z_i) = 1$. Here, $k_{d,\rm i}$ is the damping

wavenumber at recombination epoch,

$$k_{d,\mathrm{i}} = 2\pi \ \mathrm{Mpc}^{-1} \left[1.32 \times 10^{-3} \left(\frac{B_0}{\mathrm{nG}} \right)^2 \left(\frac{0.02}{\Omega_{\mathrm{b}} h^2} \right) \left(\frac{\Omega_{\mathrm{m}} h^2}{0.15} \right)^{1/2} \right]^{-\frac{1}{n_B+5}} . \tag{4.10}$$

Here, to smooth the magnetic field amplitude over the inverse length scale of $k_{d,\mathrm{i}}$, we choose the Gaussian window function in Fourier space (k) as [49, 50, 335],

$$B^2_{k_{d,\mathrm{i}}} = \int_0^\infty \frac{d^3k}{(2\pi)^3} \ \mathrm{e}^{-k^2 \left(\frac{2\pi}{k_{d,\mathrm{i}}} \right)^2} P_B(k) = B_0^2 \left[\frac{k_{d,\mathrm{i}}}{2\pi \ \mathrm{Mpc}^{-1}} \right]^{n_B+3} . \tag{4.11}$$

The magnetic field strength smoothed over the scale of 1 Mpc,

$$B^2_{1 \ \mathrm{Mpc}} = \int (dk/2\pi)^3 \ \exp[-(k/\mathrm{Mpc}^{-1})^2] \ P_B(k) = B_0^2 \, .$$

Lorentz force and the magnetic energy density can be calculated as [50],

$$|(\boldsymbol{\nabla} \times \boldsymbol{B}) \times \boldsymbol{B}|^2 = \int_{k_1,k_2} k_1^2 \ P_B(k_1) \ P_B(k_2) \ f^{2n_B+8}(z) \ (1+z)^{10} \, , \tag{4.12}$$

here $\int_{k_1,k_2}[\cdots] = \int\int d^3k_1/(2\pi)^3 \times d^3k_2/(2\pi)^3 \, [\cdots]$, and

$$E_B = \frac{1}{8\pi} \int \frac{d^3k}{(2\pi)^3} \ P_B(k) \ f^{n_B+3}(z) \ (1+z)^4 \, . \tag{4.13}$$

We can get the redshift evolution of the function $f(z)$, by substituting equation (4.13) in equation (4.7).

4.6 Impact on the thermal and ionization history due to background radiation

Heating of IGM due to background radio radiation during cosmic dawn era has been discussed in chapter (2). After inclusion of heating due to excess radio

radiation and x-ray, the equation (4.4) will modify,

$$\frac{dT_{\rm gas}}{dz} = \frac{dT_{\rm gas}}{dz}\bigg|_{\rm [eq.(4.4)]} + \frac{dT_{\rm gas}}{dz}\bigg|_{\rm x-ray} - \frac{\Gamma_R}{(1+z)\,(1+f_{He}+x_e)}\,, \tag{4.14}$$

where, $dT_{\rm gas}/dz\big|_{\rm [eq.(4.4)]}$ stands for the gas temperature evolution represented in equation (4.4). To include the x-ray heating of the gas, we consider the *tanh* parameterization [51, 74, 75]. In the presence of x-ray radiation, the ionization fraction evolution will also change. For the present case, we consider the fiducial model, for x-ray heating and ionization fraction evolution, motivated by Ref. [51]. The heating effects of both the VDKZ18 (the last term in equation 4.14— discussed in chapter 2) and x-ray are shown in plots (4.1, 4.2, 4.4, 4.7 & 4.9).

4.7 Result and discussion

We consider the following values for the cosmological parameters: $\Omega_{\rm m} = 0.31$, $\Omega_{\rm b} = 0.048$, $h = 0.68$, $\sigma_8 = 0.82$ and $n_s = 0.97$ [48]. To study the gas temperature evolution with redshift in the presence of primordial magnetic field dissipation, we solve the coupled equations (2.9 with $\mathcal{E} = 0$), (4.4) and (4.7). To get the Lorentz force term in equation (4.5), we solve the equation (4.12). Similarly, to get the magnetic field energy density in equation (4.6), we solve the equation (4.13). To get the evolution of the $f(z)$ with redshift, $df(z)/dz$, we substitute equation (4.13) in equation (4.7) with initial condition $f(z_i) = 1$. To obtain upper constraint on PMFs strength, we solve the equation (1.19) with equations (4.4), (2.9 with $\mathcal{E} = 0$) and (4.7) for $T_{21} \simeq -300$ mK or -500 mK by varying B_0, n_B and A_r. For infinite Lyα coupling $T_S \simeq T_{\rm gas}$, therefore, T_S solely depends on the gas temperature. While, for finite Lyα coupling, T_S depends on both the gas and background radiation temperature.

In figures (4.1), (4.2) & (4.3), we plot the gas temperature vs. redshift for different values of present-day strengths of PMFs (B_0) and excess radio background

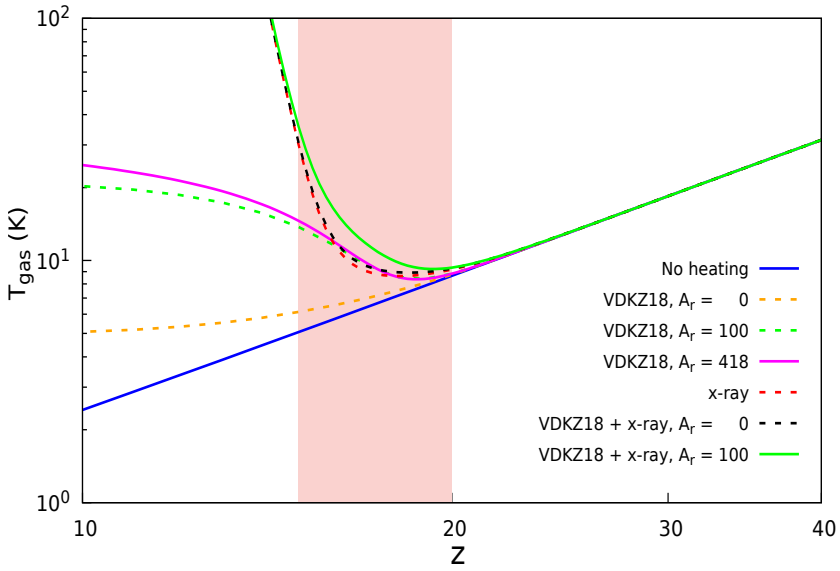

Figure 4.1: The gas temperature evolution with redshift. The solid blue lines represent the case when there is no x-ray, VDKZ18 or magnetic heating. VDKZ18 corresponds to the heat transfer from the background radiation to gas mediated by Lyα. The shaded region represents the EDGES observation redshift range, $15 \leq z \leq 20$. In this figure, we consider only VDKZ18 and x-ray heating with excess radiation (A_r).

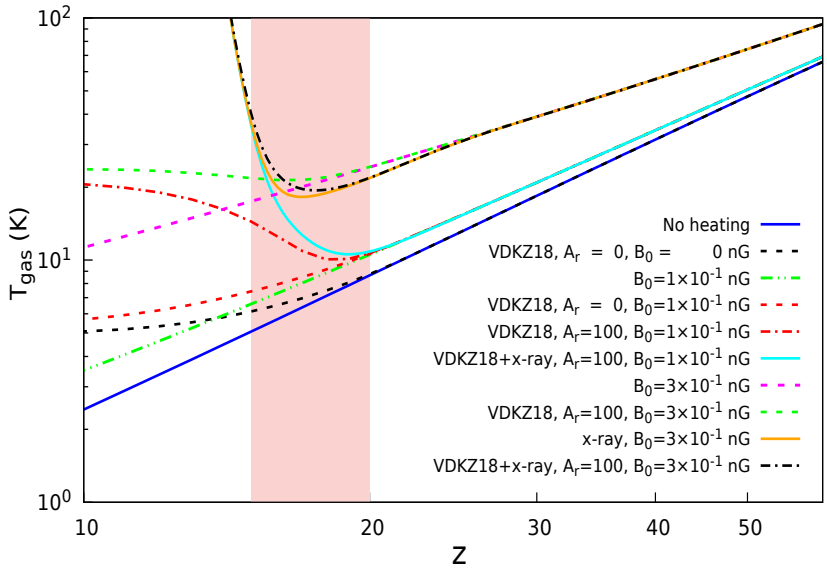

Figure 4.2: The caption is same as in figure (4.1), except here, we include different combination of VDKZ18, x-ray and magnetic heating, and spectral index is fixed to -2.99 .

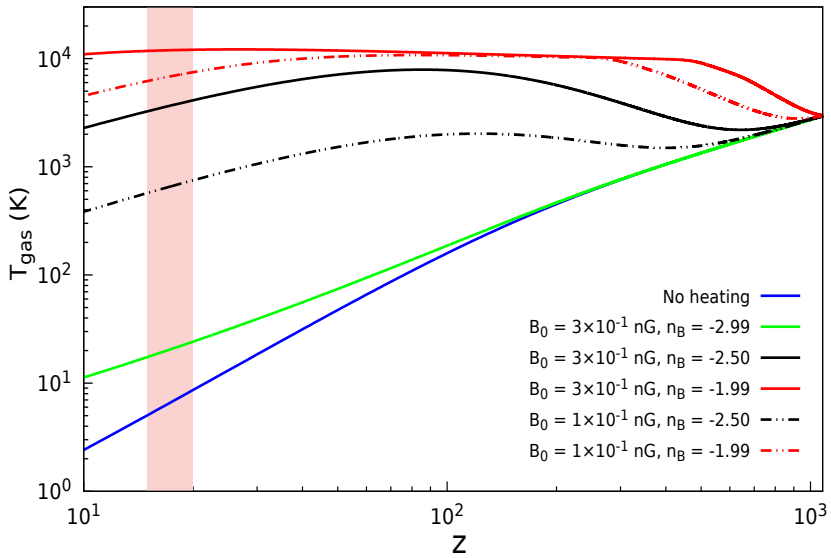

Figure 4.3: The caption is same as in figure (4.1), except here, we vary the spectral index and plot magnetic heating of the gas.

fraction (A_r). The solid blue lines represent the case when there is no heating of the IGM gas, i.e. no x-ray, VDKZ18 or magnetic heating. The pink shaded band in the figure shows the EDGES redshift range, $15 \leq z \leq 20$, for the 21 cm absorption signal. In plot (4.1), we consider only VDKZ18 and x-ray heating. The orange dashed line describes the heating due to VDKZ18 only while keeping $A_r = 0$. Next, we increase the value of A_r from 0 to 100. This case is described by the dashed-green line in plot (4.1), which shows a significant rise in the gas temperature due to the excess radiation fraction. Further, if one increases the A_r to its LWA 1 limit, i.e. $A_r = 418$, the gas temperature does not change significantly from $A_r = 100$ case, as shown by the solid magenta curve. It happens because $\Gamma_R \propto (T_R/T_S - 1) \sim T_R/T_S$, equation (2.15). As we increase A_r, T_R/T_S increases slowly. For example, at $z = 17$, T_R/T_S is 6.5 for $A_r = 0$, 51.4 for $A_r = 100$ and 54.9 for $A_r = 418$. Here, we can see that, even increasing A_r to ~ 4 times (100 to 418), T_R/T_S increases by only 6.8 percent. Therefore, increasing further A_r will not affect gas temperature significantly. To analyse the role of x-ray heating, we have first considered the heating due to x-ray only, depicted by the red dashed line. The inclusion of VDKZ18 for $A_r = 0$ further increases the gas temperature slightly, as shown by the black dashed line. In this case of inclusion of x-ray heating, if we increase the value of A_r to 100, there is a significant increase in the gas temperature as shown by the solid green line. We find the contribution due to x-ray heating dominates for redshift values $z \lesssim 15$.

In plot (4.1), we compare the contribution of VDKZ18 and x-ray heating. In plot (4.2), we compare the contributions of VDKZ18, x-ray and magnetic heating while keeping the spectral-index, $n_B = -2.99$ for a nearly scale-invariant magnetic field spectrum. While in figure (4.3), we vary the magnetic spectral index (n_B) and plot the magnetic heating of the gas.

In plot (4.2), we have included the effect of primordial magnetic fields on the IGM gas evolution. The solid blue line represents the case when there is no heating, and the dashed-black curve shows the case of VDKZ18 with no magnetic fields

and x-ray for $A_r = 0$. The double dot-dashed green curve represents the case when there is only the magnetic heating with a magnetic field strength of $B_0 = 1 \times 10^{-1}$nG. Next, we include the case of VDKZ18 for $A_r = 0$ in the pure magnetic heating scenario, as shown by the red dashed curve. Now, if we increase A_r from 0 to 100, the gas temperature rises significantly in the shaded region as shown by the dash-dotted red curve in figure (4.2). Now the further addition of x-ray heating is shown by the cyan plot, which shows significant heating in the shaded region. Next, for more analysis, we increase the magnetic field strength from $B_0 = 1 \times 10^{-1}$ nG to $B_0 = 3 \times 10^{-1}$ nG and study cases with VDKZ18 and x-ray as before. The magenta dashed line depicts the case with only magnetic heating. The green dashed line shows the case of VDKZ18 with $A_r = 100$. The orange curve shows the case with magnetic and x-ray heating only. Here, as expected, the gas temperature decreases after the inclusion of the x-ray effect with the magnetic fields. It happens because the ionization fraction increases by x-ray radiation. Ambipolar diffusion evolves as $\Gamma_{\rm ambi} \propto (1 - x_e)/x_e$; therefore, as ionization fraction increases, ambipolar diffusion of the magnetic field decreases. Thus, the heating due to magnetic fields also decreases. Therefore, including the x-ray contribution with the magnetic field decreases the magnetic field diffusion. Hence, the gas temperature decreases (this effect also occurs for $B_0 = 1 \times 10^{-1}$ nG, but it is not visible in the plot). The black dot-dashed line includes all the three effects: magnetic and x-ray heating together with VDKZ18 for $A_r = 100$ and $B_0 = 3 \times 10^{-1}$ nG. Here, the addition of the VDKZ18 heating for $A_r = 100$ increases the gas temperature above the solid orange line. It is also lower than the magenta dashed line because of the inclusion of the x-ray contribution. At the smaller redshift, x-ray heating dominates over all other heating mechanisms, and all lines merge.

In figure (4.3), we plot the magnetic heating of the gas for the different spectral index (n_B) and B_0. The solid lines, except the blue one, represent the magnetic heating for $B_0 = 3 \times 10^{-1}$ nG, while double dot-dashed lines are for $B_0 = 1 \times 10^{-1}$ nG. Increasing the spectral index, the magnetic heating due to ambipolar

diffusion and turbulent decay increases as $\Gamma_{\rm ambi} \propto \left(1/\Gamma[(n_B+3)/2]\right)^2$ and $\Gamma_{\rm turb} \propto 1/\Gamma[(n_B+3)/2]$ (by ignoring the logarithmic and integral dependencies). For example, if one changes n_B from its value -2.99 to -1 then $1/\Gamma[(n_B+3)/2]$ changes from 5×10^{-3} to 1. Therefore, by increasing n_B from -2.99 to -1, magnetic heating enhances significantly. To get T_{21} (equation 1.19) around -500 mK or -300 mK at $z = 17.2$, one needs to ensure that even by increasing n_B, that the factor $x_{\rm HI}\,(1 - T_R/T_S)$ remains same. Thus from equations (4.5), (4.6) and (4.9) when we increase n_B, we have to decrease B_0 so that the magnetic heating contribution to the gas remains the same. Therefore, by increasing n_B, the upper bound on B_0 will become more stringent. Here, we also include the collisional ionization of the gas in equation (2.9), as this term is important only when gas temperature is $\gtrsim 1.58 \times 10^5$ K. Otherwise this term is exponentially suppressed as $\propto \exp[-(13.6\ {\rm eV})/T_{\rm gas}]$ [259, 336, 337]. In plot (4.3), the gas temperature rises by increasing B_0, as more magnetic energy is getting injected into thermal energy of the gas via $\Gamma_{\rm ambi} \propto E_B^2$ and $\Gamma_{\rm turb} \propto E_B$. However, for redshift $z \lesssim 100$, the gas temperature starts decreasing as the cooling effect due to expansion of the Universe become dominant, as can be seen in equations (4.4) & (4.7) (it also depends on the strength and spectral index of the magnetic field). Since, with the expansion of the Universe, magnetic energy density (E_B) also dilutes, the contributions from $\Gamma_{\rm ambi}$ and $\Gamma_{\rm turb}$ decreases as can be seen from equations (4.5), (4.6) and (4.7).

In figure (4.4), we plot the spin (dashed lines) and gas (solid lines) temperature. For $A_r = 0$, i.e. $T_R = T_{\rm CMB}$, we get $T_{\rm gas} \simeq T_S$ as seen by the overlapping dashed and solid blue lines in the shaded region. x_α and x_c are $\propto 1/T_R$ as can be seen from equations (1.8) and (1.9). Therefore, the coupling between the gas and spin temperature decreases by increasing A_r. As discussed before, increasing the value of A_r above ~ 100, the spin temperature increases, but the increment in gas temperature becomes insignificant, and the T_R/T_S ratio increases slowly. Therefore, as x_α and x_c decreases, the difference between the gas and spin temperature increases, as shown in the plot (4.4). Increasing the values of A_r from 100 (green

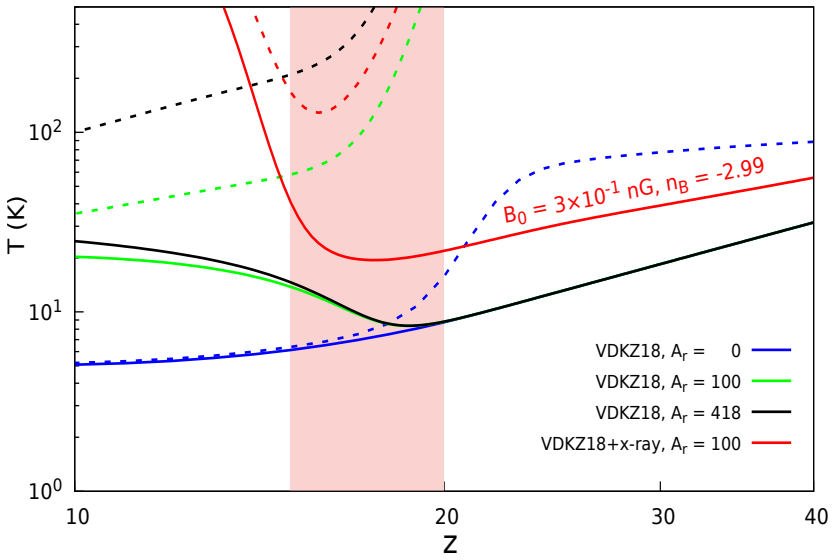

Figure 4.4: This figure shows the gas (solid lines) and spin (dashed lines) temperature evolution, The shaded region corresponds to the redshift $15 \leq z \leq 20$— the redshift range for EDGES reported signal.

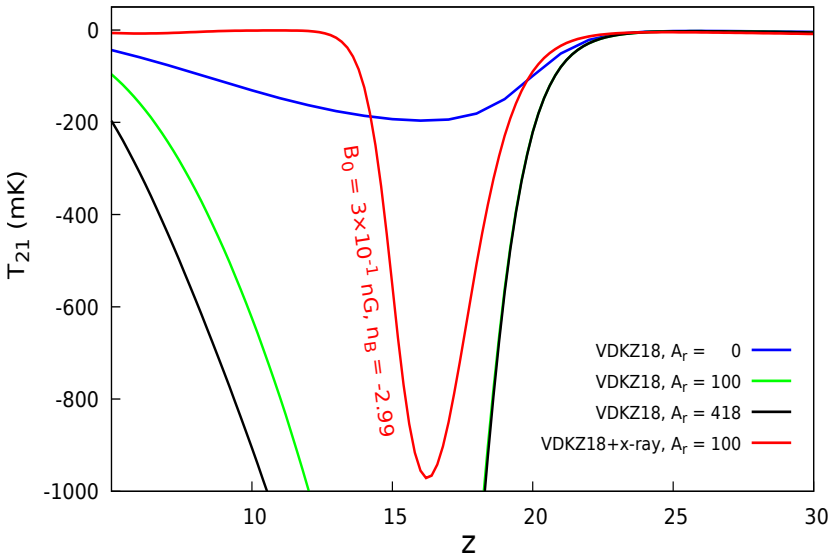

Figure 4.5: This figure shows the 21 cm differential brightness temperature with redshift for same cases in plot (4.4).

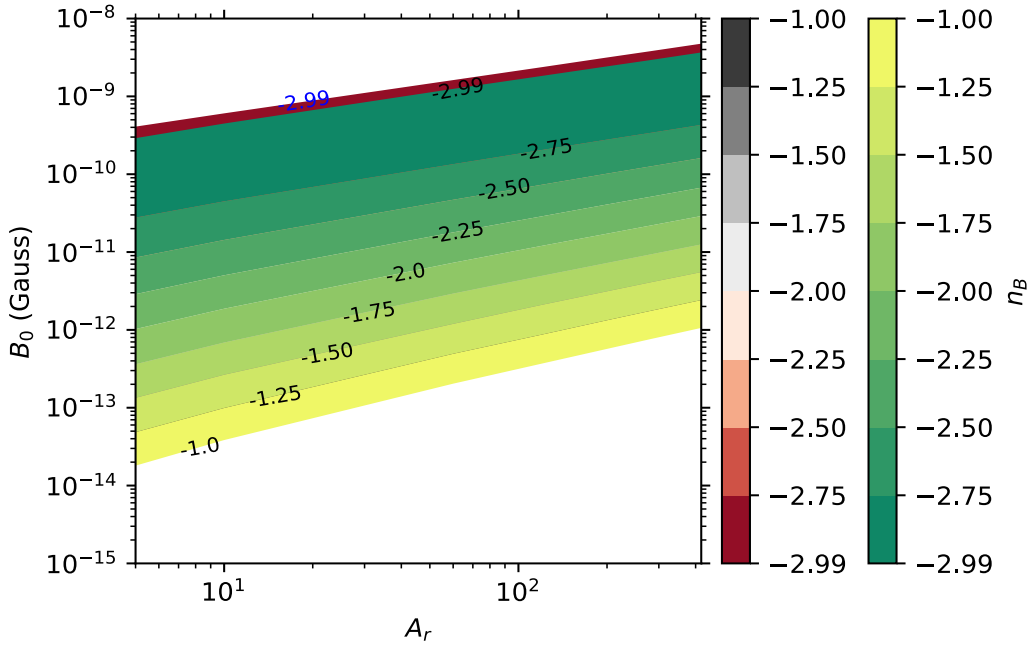

Figure 4.6: In this figure, we study upper bounds on present-day magnetic field strength (B_0) with excess radiation fraction (A_r) for different values of the spectral index, n_B. The green-yellow and red-grey colour schemes represent the cases when $T_{21}|_{z=17.2} \simeq -500$ mK and -300 mK, respectively. For $T_{21}|_{z=17.2} \simeq -300$ mK case the value of n_B written with blue coloured text , while for -500 mK case it is written with black coloured text. Here, we consider $T_{\rm S} \simeq T_{\rm gas}$ and do not take into account the x-ray and VDKZ18 effects.

lines) to 418 (black lines), the difference between gas and spin temperatures increases. Figure (4.5), shows the plots for 21 cm differential brightness temperature vs. redshift, for all the cases discussed in plot (4.4). As we increase the A_r from 0 to 100 the $|T_{21}|$ increases. By increasing A_r from 100 to 418, values of T_{21} does not change significantly. Further, including x-ray heating and magnetic heating (for $B_0 = 3 \times 10^{-1}$ nG and $n_B = -2.99$) the gas temperature rises and $|T_{21}|$ decreases.

In figures (4.6) and (4.7), we plot the maximally allowed values of B_0 versus radiation excess (A_r) for different spectral indexes. The colour-bars represent the

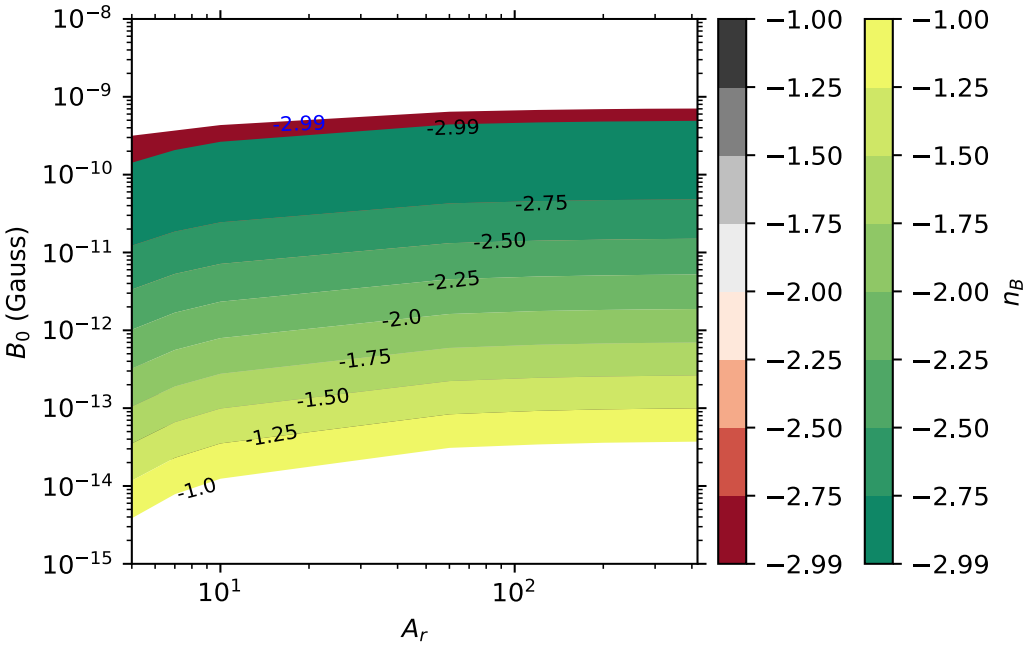

Figure 4.7: The caption is same as in figure (4.6), except here, we consider the effects of VDKZ18 and x-ray heating on the gas due to first stars after $z \lesssim 35$ and consider finite Lyα coupling.

variation of the magnetic field spectral index. In the plots, the spectral index varies from its nearly scale-invariant value (-2.99) to -1. Here, we consider both the EDGES best fit and upper constraint on the 21 cm absorption signal for constraining B_0. The green-yellow colour scheme represents the case with $T_{21}|_{z=17.2} \simeq -500$ mK, while the red-grey colour scheme represents the case with $T_{21}|_{z=17.2} \simeq -300$ mK. Numerical values of n_B for the different colour bands are written with different colour. For $T_{21}|_{z=17.2} \simeq -300$ mK case the value of n_B written with blue coloured text , while for $T_{21}|_{z=17.2} \simeq -500$ mK case it is written with black coloured text. The colour-bars are common for both the plots.

In figure (4.6), we consider infinite Lyα coupling ($x_\alpha \gg x_c$, 1), i.e. $T_S \simeq T_{\rm gas}$. Here, we do not consider the x-ray and VDKZ18 effects on the gas and thus the 21 cm signal $T_{21} \propto (1 - T_R/T_{\rm gas})$. As we increase A_r, the amplitude of $|T_{21}|$ increases, and we get more window to increase the gas temperature. In this plot, we consider heating only due to the decaying magnetohydrodynamics. Therefore, we can increase B_0 as we increase A_r. As discussed earlier, by decreasing n_B, the amplitude of the magnetic field power spectrum also decreases, resulting in less magnetic energy dissipation into the gas kinetic energy. Thus by reducing values of n_B from -1 to -2.99, we get more window to increase B_0. Next, when one increases T_{21} from -500 mK to -300 mK, the allowed value of B_0 also increases. This is shown by the red-grey colour scheme in figures (4.6) and (4.7). In figure (4.7), we consider the effects of VDKZ18 and x-ray on IGM gas evolution due to first stars after $z \lesssim 35$ and consider finite Lyα coupling. As discussed earlier, $T_{\rm gas} \neq T_S$ for $A_r > 0$ and the difference between gas and spin temperature increases as A_r increases. Thus, in the presence of first star's effects, the upper bound on the present-day strength of PMFs modifies. Following the Refs. [51, 74, 75], we consider WF coupling coefficient, $x_\alpha = 2A_\alpha(z) \times (T_0/T_R)$. Here, $A_\alpha(z) = A_\alpha(1 + \tanh[(z_{\alpha 0} - z)/\Delta z_\alpha])$, the step height $A_\alpha = 100$, pivot redshift $z_{\alpha 0} = 17$ and duration $\Delta z_\alpha = 2$. The collisional coupling coefficient, $x_c = T_{10}/T_R \times (N_H\, k_{10}^{HH})/A_{10}$. After the inclusion of x-ray and VDKZ18 heating effects, the gas temperature remains > 10 K. Therefore,

we can take $k_{10}^{HH} \approx 3.1 \times 10^{-11}\ (T_{\rm gas}/{\rm K})^{0.357} \exp(-32\ {\rm K}/T_{\rm gas})\ {\rm cm}^3/{\rm sec}$ for $10\ {\rm K} < T_{\rm gas} < 10^3\ {\rm K}$. As illustrated in plot (4.1), (4.2), (4.4) & (4.5), increasing excess radiation fraction A_r above ~ 100, the T_R/T_S remains nearly constant and this also mean that T_{21} remain unchanged. Consequently one can not increase the value of B_0 and one gets nearly flat profile for B_0 for $A_r \gtrsim 100$ in figure (4.7).

In figures (4.8) & (4.9), we plot the maximally allowed values of B_0 vs n_B for various values of A_r. The colour-bars represent the variation in A_r. In the plots, A_r varies from 5 to LWA 1 limit ~ 418. We consider both the EDGES best fit and upper constraint on 21 cm absorption signal for constraining B_0. The green-yellow scheme represent the case with $T_{21}|_{z=17.2} \simeq -500$ mK, while the red-grey colour scheme represent the case $T_{21}|_{z=17.2} \simeq -300$ mK. Numerical values of A_r for the different colour bands are written in different colours. For $T_{21}|_{z=17.2} \simeq -300$ mK case the value of A_r written with blue coloured text , while for $T_{21}|_{z=17.2} \simeq -500$ mK case it is written with black coloured text. The spectral index ranges from -2.99 to -1. The red dashed line represents the Planck 2015 upper constraint on the present-day magnetic field strength with spectral index in both plots. This constraint has been taken from Refs. [49, 50].

In plot (4.8), we consider $T_{\rm S} \simeq T_{\rm gas}$ and we do not take into account the x-ray and VDKZ18 effects on IGM gas evolution. The zoomed inset in the figure shows the contour plot when $T_{21}|_{z=17.2} \simeq -300$ mK. Here, considering $T_{21}|_{z=17.2} \simeq -300$ mK, for $n_B < -2.98$ the $A_r \gtrsim 200$ is excluded similarly for $n_B < -2.96$ the $A_r \gtrsim 280$ is excluded by Planck 2015 upper constraint on B_0. Likewise, for $T_{21}|_{z=17.2} \simeq -500$ mK, for $n_B < -2.97$ the $A_r \gtrsim 280$ is excluded. For spectral index -2.9 and excess radiation fraction 418, we get the upper constraint on B_0 to be ~ 1 nG and 1.3 nG by requiring $T_{21}|_{z=17.2} \simeq -500$ mK (EDGES best fit constraint) and -300 mK (EDGES upper constraint), respectively. While for $n_B = -1$, these bound change to 1.1×10^{-3} nG and 1.6×10^{-3} nG for $T_{21}|_{z=17.2} \simeq -500$ mK and -300 mK, respectively. In plot (4.9), we include both the VDKZ18 and x-ray effect and consider finite Lyα coupling. As discusses earlier, for $A_r \gtrsim 100$,

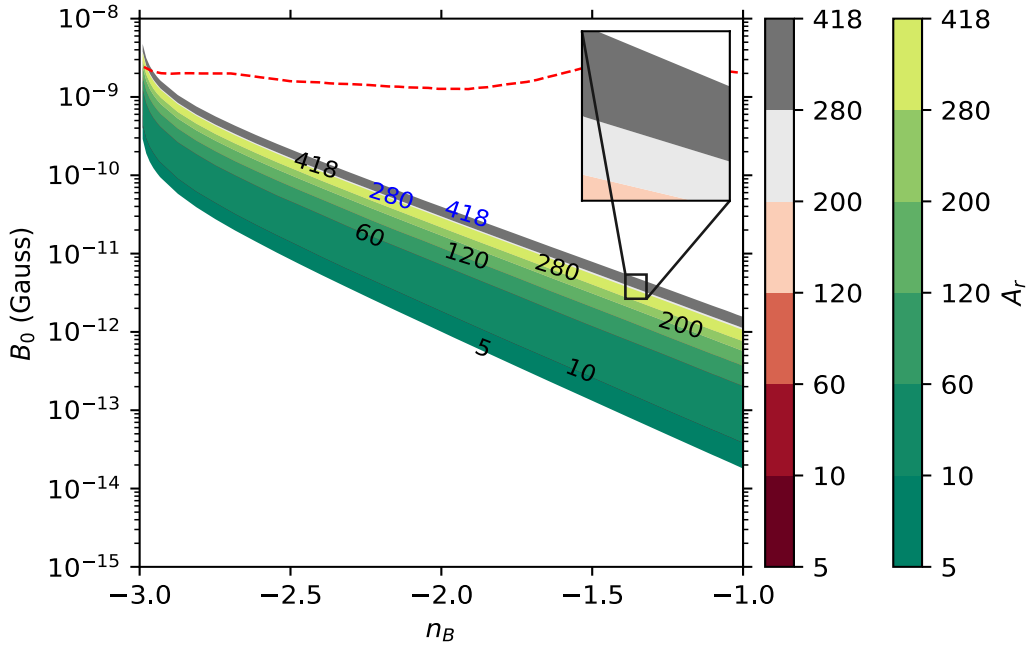

Figure 4.8: In this figure, we study upper bounds on the present-day magnetic field strength (B_0) with spectral index (n_B) for different values of excess radiation fraction (A_r). The green-yellow and red-grey colour schemes represent the cases when $T_{21}|_{z=17.2} \simeq -500$ mK and -300 mK, respectively. For $T_{21}|_{z=17.2} \simeq -300$ mK case the value of n_B written with blue coloured text , while for -500 mK case it is written with black coloured text. The red dashed line depicts the Planck 2015 upper constraint on the present-day magnetic field strength [49, 50]. Here, we consider $T_S \simeq T_{gas}$ and do not take into account the x-ray and VDKZ18 effects.

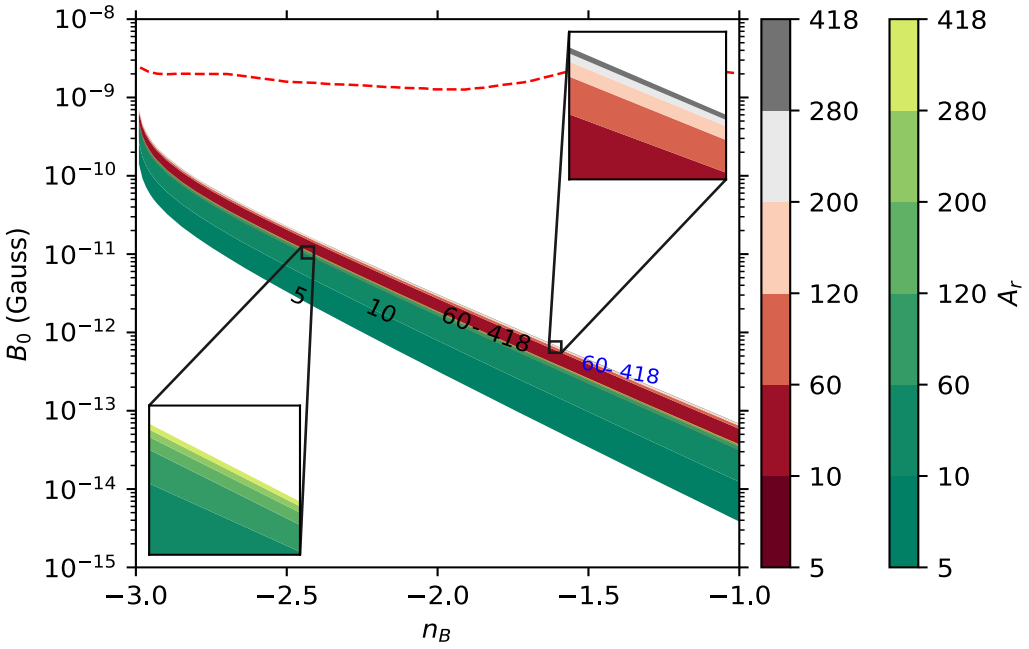

Figure 4.9: The caption is same as in figure (4.8), except here, we consider the heating effects of VDKZ18 and x-ray on IGM gas due to first stars after $z \lesssim 35$ and consider finite Lyα coupling. The colour-bars are common for both plots.

T_R/T_S ratio remain nearly constant. Thus, in the plot (4.9), we can see that for $A_r \gtrsim 100$, the upper bound on B_0 is not changing significantly— the plots are merged for $A_r \gtrsim 100$. These plots have been shown by the zoomed inset. The right upper zoomed inset is shown for $T_{21} \simeq -300$ mK, while left lower zoomed inset is shown for green-yellow contour plots when $T_{21} \simeq -500$ mK. Hence, further increasing $A_r > 100$ will not change significantly the upper bound on B_0. As illustrated in figure (4.4), $T_S > T_{\rm gas}$ for $A_r > 0$, and $T_{21} \propto (1 - T_R/T_S)$. Therefore, to get $T_{21} \simeq -300$ mK or -500 mK, we need to lower B_0 compared to previous scenario— figure (4.8). Hence, we get the more stringent upper bound on present-day magnetic field strength in figure (4.9). For spectral index -2.9 and excess radiation fraction 418, we get the upper constraint on B_0 to be $\lesssim 1.7\times10^{-1}$ nG and 1.2×10^{-1} nG by requiring $T_{21}|_{z=17.2} \simeq -300$ mK and -500 mK, respectively. For $n_B = -1$, we get $B_0 \lesssim 6.9\times10^{-5}$ nG and 3.7×10^{-5} nG by requiring EDGES upper and best fit constraint on 21 cm differential brightness temperature. Decreasing the values of A_r, the upper constraint on B_0 becomes more stringent. For example, when $A_r = 5$, we get upper bound on present day magnetic field strength to be $\lesssim 1.4 \times 10^{-1}$ nG for spectral index -2.99, and for spectral index $n_B = -1$ we get $B_0 \lesssim 3.8 \times 10^{-6}$ nG by requiring EDGES best fit constraint on T_{21}. The upper bounds are also well below the Planck 2015 constraint [49].

4.8 Conclusions

In the present work, we study the upper constraint on the strength of the primordial magnetic fields for different spectral index using the bound of EDGES observation on T_{21}, in the presence of uniform redshift-independent synchrotron like radiation reported by ARCADE 2 and LWA 1 [27, 30, 304, 310]. We have considered excess radiation fraction up to the LWA 1 limit (i.e. $A_r \sim 418$) at the reference frequency of 78 MHz [30, 310]. To get the upper constraint on B_0, we have used both the EDGES upper and best-fit constraints on T_{21}. We have

considered two scenarios: First, infinite Lyα coupling (i.e. $x_\alpha \gg x_c, 1$) without the effects of x-ray and VDKZ18 on IGM gas evolution. In another scenario, we consider the finite Lyα coupling with x-ray and VDKZ18 effects. The following summarises our results for $T_{21} = -500$ mK:

In the first scenario, for $A_r = 418$, we get $B_0 \lesssim 3.7$ nG for spectral index -2.99, while for $n_B = -1$ we get $B_0 \lesssim 1.1 \times 10^{-3}$ nG. When $A_r = 5$, upper constraint on present-day magnetic field strength varies from $B_0 \lesssim 2.9 \times 10^{-1}$ nG to 1.8×10^{-5} nG by varying n_B from -2.99 to -1, respectively.

In the second scenario, the upper bounds on B_0 will modify [34, 51]. For $A_r = 418$, we get the upper constraint on magnetic field to be $B_0(n_B = -2.99) \lesssim 4.9 \times 10^{-1}$ nG and $B_0(n_B = -1) \lesssim 3.7 \times 10^{-5}$ nG. While for $A_r = 5$, we get upper bound on present day magnetic field strength to be $\lesssim 1.4 \times 10^{-1}$ nG for spectral index -2.99, and for spectral index -1 we get $B_0 \lesssim 3.8 \times 10^{-6}$ nG.

We would like to note that these upper bounds on B_0 that we have reported here are also consistent with the Planck observations [49, 338].

"Who sees the future? Let us have free scope for all directions of research"

Ludwig Eduard Boltzmann, *"Lectures on Gas Theory" translated by Stephen G. Brush*

5

Primordial Magnetic Fields and Baryon-Dark matter Interaction

In the previous chapter (4), we have analysed the upper bound on present-day strength of PMFs in the light of EDGES observation and excess radio background reported by ARCADE 2 and LWA 1 observations [25]. As discussed earlier in chapter (1), to explain EDGES observation one requires that either the background radio radiation should be grater than ∼104 K in the absence of any non-standard mechanism for the evolution of the gas temperature or the gas temperature should be less than 3.2 K for the standard evolution of CMB temperature at the centre of the "U" profile for the best fitting amplitude [5]. The first possibility has been investigated by authors of the Ref. [339–342]. In the second scenario, IGM gas can be cooled by emitting the photons between the Ly-limit to Ly-γ wavelengths [343, 344]. There are very few mechanisms to cool the gas. Since the dark matter

is colder than the gas, effective cooling of the gas can be obtained by elastic scattering between the dark matter and baryon particles [73, 345, 346]. A new kind of interaction between dark matter and baryons was proposed by the authors of reference [345, 347] to explain the EDGES absorptional signal. The authors consider a non-standard "Coulomb-like" interaction: $\sigma = \hat{\sigma}\ v^{-4}$; v is the relative velocity between the dark matter and baryons and $\hat{\sigma}$ is the strength of baryon-dark matter interaction cross-section [73, 345–348]. Here, the interaction between dark matter and baryons does not depend on whether the baryons are free or bound within atoms [345]. The cooling of the gas, by transferring energy to the dark matter, is tightly constrained because of constraints on the dark matter mass and cross-section by cosmological and astrophysical observations [73, 345, 349, 350]. In the present chapter, we reanalyse the constraints on PMFs in the presence of baryon-dark matter interaction proposed by the authors of reference [345]. In the presence of baryon-dark matter interaction the bounds on magnetic field, baryon dark matter cross-section strength ($\hat{\sigma}$) and dark matter mass ($M_{\rm DM}$) can strongly influence each other. This requires to rework the bounds on $\hat{\sigma}$, $M_{\rm DM}$ and B_0 which can explain the observed absorption signal by EDGES collaboration. The upper limit on the magnetic field strength can modify in presence of baryon-dark matter interaction cross-section. In the presence of a strong magnetic field, a large baryon-dark matter interaction cross-section is required to balance magnetic heating of gas to explain the EDGES signal as compared to a weak magnetic field. Subsequently, the strong magnetic-fields can even erase the 21 cm signal— this gives an upper bound on the strength of magnetic-fields, dark matter mass and baryon-dark matter cross-section.

In order to explain the EDGES absorption signal, the gas temperature needs to be cooler than the ΛCDM prediction. During the Cosmic dawn era, the Universe was at its coldest phase, and the relative velocity between the dark matter and baryon was very small, $\mathcal{O}(10^{-6})$. Also, the temperature of the dark matter was colder than the baryon temperature during this period, so an interaction of the

baryon with dark matter can cool the gas temperature. Since the relative velocity is small, scattering cross section of the type $\sigma = \hat{\sigma}\, v^{-4}$ can enhance the interaction rate and cool the gas sufficiently to explain EDGES absorption dip [345, 346, 348]. In this chapter, we consider magnetic heating of the gas and dark matter via ambipolar and turbulent decay. Here, we take cosmological parameters Ω_b, Ω_m, and h as $\Omega_b = 0.04859$, $\Omega_m = 0.315$ and $h = 0.68$ [48].

5.1 Baryon-dark matter interaction in presence of magnetic fields

In this section, we discuss the effects of magnetic fields on the gas temperature in the presence of baryon-dark matter interaction. The gas temperature evolves as discussed in the chapter (4), except here, the cooling rate ($dQ_{\rm gas}/dt$) will add due to the energy transfer from gas to dark matter [254, 347],

$$\frac{dT_{\rm gas}}{dz} = 2\,\frac{T_{\rm gas}}{1+z} + \frac{\Gamma_C}{(1+z)H}(T_{\rm gas} - T_{\rm CMB}) - \frac{2}{3\,n_{\rm tot}(1+z)\,H}(\Gamma_{\rm turb} + \Gamma_{\rm ambi}) + \frac{2}{3\,(1+z)\,H}\,\frac{dQ_{\rm gas}}{dt}\,. \tag{5.1}$$

The cooling rate ($dQ_{\rm gas}/dt$) depends on the temperature difference and relative velocity between dark matter and baryons,

$$\frac{dQ_{\rm gas}}{dt} = \frac{2\,M_b\,\rho_{\rm DM}\,\hat{\sigma}\,e^{-r^2/2}}{\sqrt{2\,\pi}\,(M_b + M_{\rm DM})^2\,u_{\rm th}^3}\left(T_{\rm gas} - T_{\rm DM}\right) - \mu\,\frac{\rho_{\rm DM}}{\rho_{\rm M}}\,v\,D(v)\,, \tag{5.2}$$

here, $M_b \approx M_{\rm H}$ is the baryon mass and can be taken as mass of hydrogen atom. $\rho_{\rm DM}$ and $\rho_{\rm M}$ are the dark matter and total matter energy density, respectively. Moreover, $r = v/u_{\rm th}$, v is the relative motion between baryons and dark matter while $u_{\rm th}^2 = T_{\rm gas}/M_b + T_{\rm DM}/M_{\rm DM}$. Here, $T_{\rm DM}$ is the dark matter temperature and $\mu = M_b\,M_{\rm DM}/(M_b + M_{\rm DM})$ is the reduced mass. The first term in equation (5.2), arises due to the temperature difference between dark matter and gas. As

$T_{\rm DM} < T_{\rm gas}$, the first term is positive. It implies that the energy of gas is being transferred to dark matter with time. The second term in equation (5.2), comes due to the friction between two fluids caused by velocity difference— drag term, and it is given by $\mu\,(\rho_{\rm DM}/\rho_{\rm M})\,v\,D(v)$,

$$D(v) \equiv \frac{\rho_{\rm M}\,\hat{\sigma}}{M_b + M_{\rm DM}}\,\frac{1}{v^2}\,F(r)\,, \tag{5.3}$$

here, $r = v/u_{\rm th}$ and the function $F(r)$ is defined as,

$$F(r) \equiv {\rm erf}\left(\frac{r}{\sqrt{2}}\right) - \sqrt{\frac{2}{\pi}}\,r\,e^{-r^2/2}\,, \tag{5.4}$$

here, erf() is the Gauss error function. When the relative velocity between dark matter and baryons is zero, i.e. $r = 0$, one gets $F(0) = 0$. In this case there will not be any drag heating of gas and dark matter. As $r \to \infty$, $F(r) \to 1$. For any value of $r \geq 0$, one finds that $F(r) \geq 0$. Therefore, the last term in equation (5.2) always remains negative. It implies that the energy of gas always increases due to the drag. In equation (5.2), one can check that the heating gets maximize due to drag as $M_{\rm DM} \to M_b$. The dark matter temperature evolution can be written as,

$$\frac{dT_{\rm DM}}{dz} = 2\,\frac{T_{\rm DM}}{(1+z)} + \frac{2}{3\,(1+z)\,H}\,\frac{dQ_{\rm DM}}{dt}\,, \tag{5.5}$$

here, first term represents the cooling of the dark matter due to expansion of the Universe. Heat transfer rate for dark matter $(dQ_{\rm DM}/dt)$ can be obtained by interchanging $b \leftrightarrow$ DM and $T_{\rm gas} \leftrightarrow T_{\rm DM}$ in equation (5.2). As drag term (5.3) remains symmetric under the transformation $b \leftrightarrow$ DM, it heats the dark matter also. We can also check that total energy density of the system is conserved [347],

$$N_{\rm DM}\,\frac{dQ_{\rm DM}}{dt} + N_b\,\frac{dQ_{\rm gas}}{dt} - \frac{\rho_{\rm DM}\,\rho_b}{\rho_{\rm M}}\,v\,D(v) = 0\,, \tag{5.6}$$

here, $N_{\rm DM}$ and N_b are number density of dark matter and baryons. As the relative motion between dark matter and baryons is damped due to friction between both

fluids and expansion of the Universe, one can write the evolution of relative motion as,

$$\frac{dv}{dz} = \frac{v}{1+z} + \frac{D(v)}{(1+z)\,H}\,. \tag{5.7}$$

Temperature evolutions of the gas and dark matter require free electron fraction. It is given by equation (2.9) with $\mathcal{E} = 0$. As it has been confirmed in Ref. [50], that cooling due to effects like Lyα emission, Bremsstrahlung and recombination does not have that much effects on the dynamics of the gas and dark matter, therefore, we have not considered these effects in the present work.

5.2 Results and Discussion

Solving coupled equations (2.9 with $\mathcal{E} = 0$, 4.7, 5.1, 5.5 and 5.7) with initial conditions $T_{\rm gas}(1010) \simeq T_{\rm CMB}(1010)$, $T_{\rm DM}(1010) \sim 0$ K, $x_e(1010) = 0.057$ and $B(z) = B_0\,(1+z)^2|_{z=1010}$ is the initial magnetic field strength, we get the temperature evolution of the dark matter and gas for different dark matter masses, strength of baryon-dark matter interaction cross-sections and magnetic field's strengths. Figures (5.1), (5.2) and (5.3) show the evolution of the gas and dark matter temperature with redshift (z). The solid blue line in all these figures correspond to gas temperature when both the magnetic field and baryon-dark matter interaction are zero. In this case, gas temperature falls as $T_{\rm gas} \propto (1+z)^2$ after $z \sim 200$ and reaches 6.8 K at $z = 17$.

In figure (5.1), temperature evolution of the gas and dark matter is given for different strength of PMFs at constant $\hat{\sigma} = 10^{-41}$ cm^2 and $M_{\rm DM} = 10^{-1}$ GeV. For both the cases $B_0 = 10^{-5}$ G and 10^{-6} G, gas temperature falls down due to Hubble expansion and baryon-dark matter interaction till $z \sim 30$ and ~ 20, respectively, then temperature rises due to magnetic heating. We note that, $T_{\rm DM}$ also increases due to the energy transfer from gas to dark matter depending on $\hat{\sigma}$ and $M_{\rm DM}$.

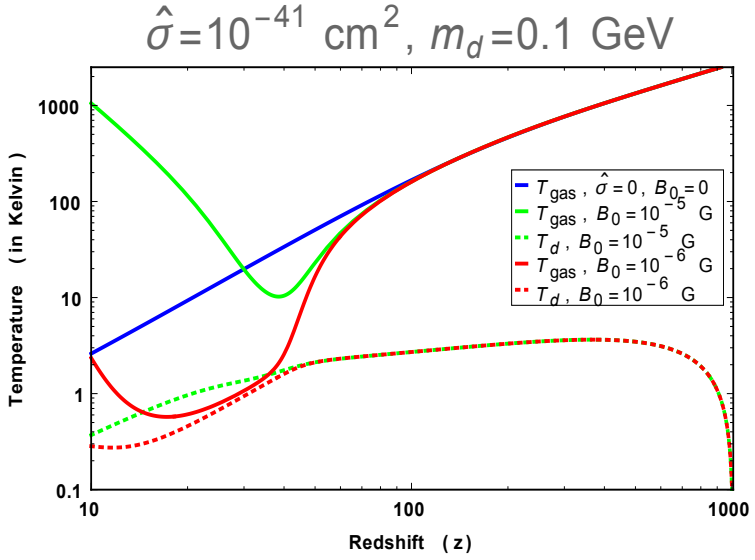

Figure 5.1: This figure shows the temperature evolutions of baryon and dark matter in the presence of PMFs and baryon-dark matter interaction. Blue line corresponds to temperature evolution of gas in the absence of both magnetic heating and baryon-dark matter interaction. The red (green) solid lines represents the variation of the gas temperature and the dotted red (green) line shows the variation of the dark matter temperature in presence of PMFs and the baryon-dark matter interaction. In this plot we vary the strength of PMFs, and keep $\hat{\sigma}$ & dark matter mass constant to 10^{-41} cm^2 & 10^{-1} GeV, respectively. In all figures, notation for the mass of dark matter is written with m_d. While in the text, it is written as $M_{\rm DM}$.

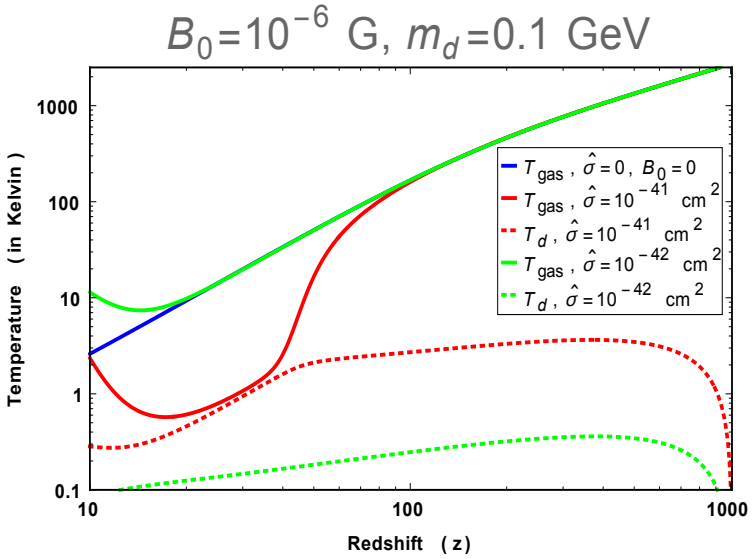

Figure 5.2: The caption is same as in figure (5.1), except here, we only vary the strength of baryon-dark matter cross-section, and keep B_0 & dark matter mass constant to 10^{-6} G & 10^{-1} GeV, respectively.

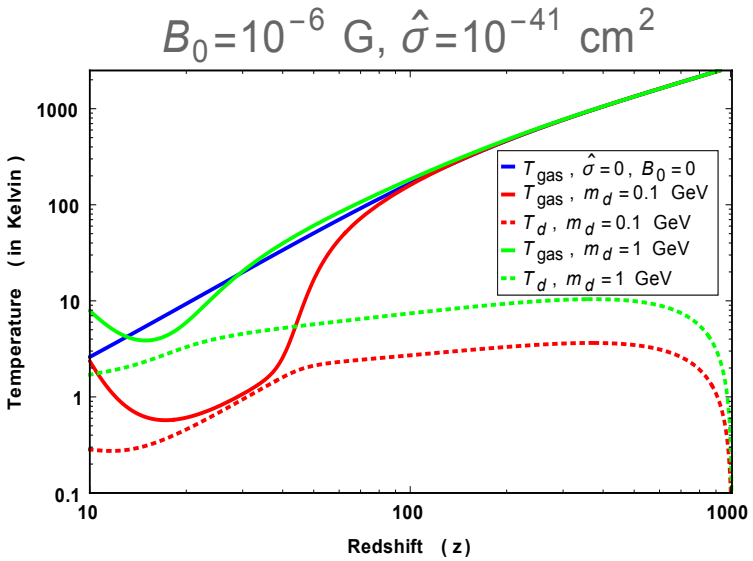

Figure 5.3: The caption is same as in figure (5.1), except here, we only vary the dark matter mass, and keep B_0 & $\hat{\sigma}$ constant to 10^{-6} G & 10^{-41} cm^2, respectively.

Larger the strength of magnetic fields, earlier the heating begins. For example, heating for the case with $B_0 = 10^{-5}$ G starts earlier compared to the case with $B_0 = 10^{-6}$ G in figure (5.1). Although $T_{\rm DM}$ at $z \sim 1010$ is taken to be zero, it increases due to the energy transfer from baryons to dark matter. By increasing B_0, magnetic-heating of the gas rises, subsequently, the value of $T_{\rm DM}$ also rises. It can be seen in figure (5.1), temperature of dark matter for $B_0 = 10^{-5}$ G is larger compared to $B_0 = 10^{-6}$ G.

Figure (5.2) shows the temperature evolution of gas and dark matter for different strength of baryon-dark matter interaction cross-section when $B_0 = 10^{-6}$ G and $M_{\rm DM} = 10^{-1}$ GeV are fixed. Larger the $\hat{\sigma}$, more heat transfers from gas to dark matter and cools the gas efficiently. For the green lines $\hat{\sigma} = 10^{-42}$ cm^2. As we increase $\hat{\sigma}$ to 10^{-41} cm^2, the gas temperature decreases— shown by red solid line. It decreases because the energy transfer from gas to dark matter becomes more efficient by increasing interaction between dark matter and baryons. It results in more heating of dark matter— shown by red dashed line.

For $B_0 = 10^{-6}$ G and $\hat{\sigma} = 10^{-41}$ cm^2, temperature evolution for different dark matter mass is shown in Figure (5.3). As we increase the dark matter mass from 10^{-1} GeV to 1 GeV, temperature of both the dark matter and gas increases, and it becomes more efficient for large dark matter mass [347]. This drag heating is important when mass of dark matter is around $\sim$ 1 GeV [347]. When $M_{\rm DM}$ approaches to 1 GeV, in addition to magnetic heating of the gas, the heating due to drag term also becomes effective . Therefore, the gas temperature for $M_{\rm DM} = 1$ GeV is higher than $M_{\rm DM} = 10^{-1}$ GeV.

5.2.1 Correlation between dark matter mass and baryon-dark matter cross section

In this subsection, we analyse the effect of B_0, $M_{\rm DM}$ and $\hat{\sigma}$ on gas and dark matter temperature. In Fig. (5.4), we study constraints on $M_{\rm DM}$ and $\hat{\sigma}$ for $T_{21} \simeq -500$ mK

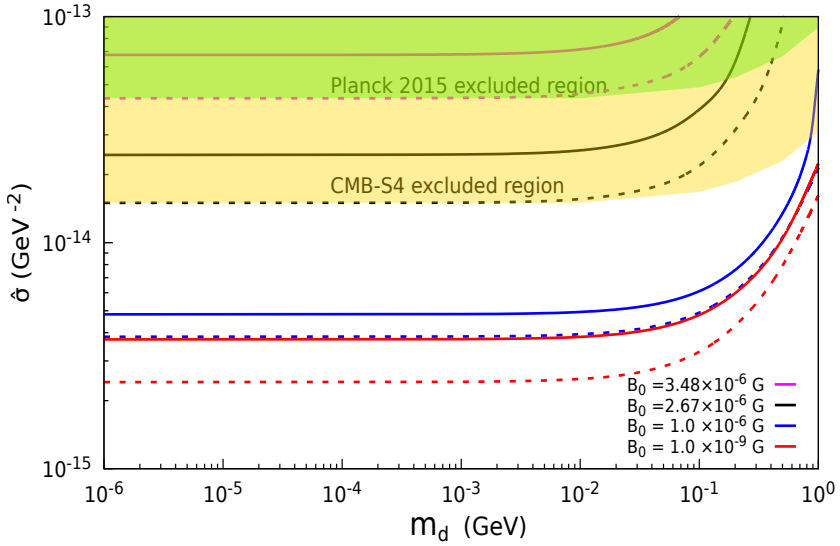

Figure 5.4: The figure shows the minimal cross-section required to get $T_{21} \simeq -500$ mK (solid lines) and $T_{21} \simeq -300$ mK (dashed line) at $z = 17$ as a function of mass for different strengths of PMFs. Here, we assume no x-ray heating of gas, and spin temperature is completely coupled to gas temperature, i.e. $T_{\rm gas} \simeq T_S$. The solid (dashed) magenta, black, blue and red line correspond to $B_0 = 3.48 \times 10^{-6}$ G, 2.67×10^{-6} G, 10^{-6} G and 10^{-9} G respectively. The CMB-S4 (forecast) and Planck 2015 constraints on $\hat{\sigma}$ and $M_{\rm DM}$ with 95% C.L. have been taken from the Refs. [51, 52]. The green and gold regions are excluded by Planck 2015 and CMB-S4 forecast respectively. (1 GeV$^{-2} = 3.89 \times 10^{-28}$ cm^2)

($T_{\rm gas} \simeq 3.26$ K) and -300 mK ($T_{\rm gas} \simeq 5.2$ K). Here, we have taken $x_\alpha \gg 1$ to plot T_{21} profiles. Thus, from equation (1.7) one can get $T_S \approx T_{\rm gas}$ as x_c is already $\ll 1$ at required redshift due to the small number density of hydrogen, free electrons and protons. Subsequently, one can calculate T_{21} from equation (1.19). In Fig. (5.4), we consider cases $B_0 = 3.48 \times 10^{-6}$ G, 2.67×10^{-6} G, 10^{-6} G and 10^{-9} G and solve equations (2.9 with $\mathcal{E} = 0$) and (4.7, 5.1, 5.5 & 5.7) for $T_{\rm gas} \simeq 3.26$ and 5.2 K at $z = 17$ to get $\hat{\sigma}$ vs $M_{\rm DM}$ plots. The solid and dashed lines represent the cases when $T_{21} \simeq -500$ mK and -300 mK, respectively. The gold and green regions respectively show the CMB-S4 (forecast) and Planck 2015 upper constraint on $\hat{\sigma} - M_{\rm DM}$ with 95% C.L. [51, 52]. The magenta, black, blue and red lines corresponds to $B_0 = 3.48 \times 10^{-6}$ G, 2.67×10^{-6} G, 10^{-6} G and 10^{-9} G. As we increase the magnetic field strength from 10^{-9} G to $\sim 10^{-6}$ G, larger value of $\hat{\sigma}$ is required for $M_{\rm DM} \in \{10^{-6},\ 1\}$ GeV to maintain $T_{21} \simeq -500$ or -300 mK at z=17. To get EDGES upper limit on T_{21} (i.e. -300 mK), required $\hat{\sigma}$ is smaller compared to the case when $T_{21} = -500$ mK. This is because we need to transfer less energy from gas to the dark matter to obtain EDGES upper limit on T_{21}. We get the upper limit on PMFs strength to 2.67×10^{-6} G by CMB-S4 (forecast) constraint on $\hat{\sigma} - M_{\rm DM}$ and maintaining $T_{21} \simeq -300$ mK at z=17. For $B_0 = 2.67 \times 10^{-6}$ G, $M_{\rm DM} \gtrsim 10^{-2}$ GeV is excluded by CMB-S4 forecast for $T_{21} \simeq -300$ mK. By Planck 2015 constraint on $\hat{\sigma} - M_{\rm DM}$, the allowed maximum strength of PMFs is 3.48×10^{-6} G by requiring EDGES upper constraint on T_{21} at z=17. For $B_0 = 3.48 \times 10^{-6}$ G, mass of dark matter $\gtrsim 1 \times 10^{-2}$ GeV is excluded. Similarly, for the $B_0 = 10^{-6}$ G, $M_{\rm DM} \gtrsim 8 \times 10^{-1}$ GeV is excluded by CMB-S4 forecast. When the dark matter mass approaches mass of hydrogen, the drag term in equation (5.3) also starts to contribute significantly in heating of the gas in addition to the magnetic heating. Therefore, higher mass of dark matter is excluded for higher magnetic field as shown by figure (5.4). As discussed in [347], when $M_{\rm DM} \sim 1$ GeV, the drag term heat up both the gas and dark matter in such a way that we can not obtain $T_{\rm gas} = 3.26$ K at $z = 17$ as required for the EDGES

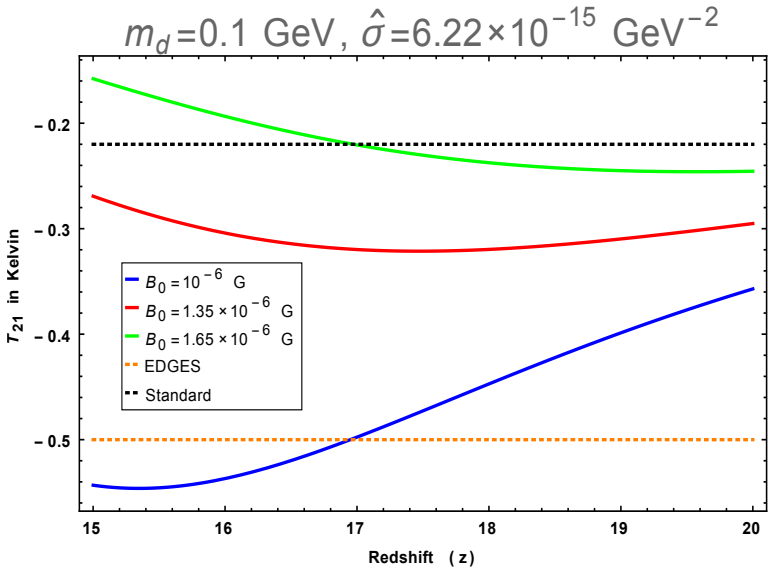

Figure 5.5: 21 cm differential brightness temperature (assuming infinite Lyα coupling) vs redshift when their is no x-ray heating. The dotted black (orange) colour represents standard ΛCDM (EDGES) predictions for the global T_{21} signal. Green, red and blue solid curves correspond to $B_0 = 1\times10^{-6}$, 1.35×10^{-6} and 1.65×10^{-6} G respectively. Here, $M_{\rm DM} = 10^{-1}$ GeV and $\hat{\sigma} = 6.22 \times 10^{-15}$ GeV^{-2}.

signal. There is a independent bound on the primordial magnetic field from CMB of the order of $\lesssim$ nG [287, 288]. This constraint, in our analysis, restricts value of $\hat{\sigma}$. Here, we note that in our analysis further decreasing value of B_0 below 10^{-9} G, does not change our result in significant way.

5.2.2 Effect of primordial magnetic fields on the global 21 cm signal

We have discussed above that, with increase in the strength of the magnetic field the temperature of the gas increases for a fix $M_{\rm DM}$ and $\hat{\sigma}$. In figures (5.5) & (5.6), we plot 21 cm differential brightness temperature with redshift for different magnetic field strengths. These figures are obtained by keeping $M_{\rm DM} = 10^{-1}$ GeV

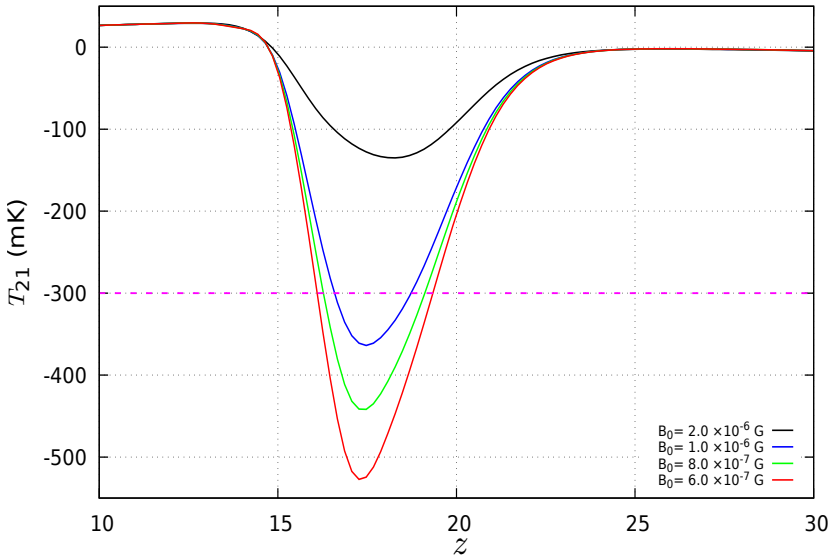

Figure 5.6: T_{21} plot with redshift when x-ray heating and finite Lyα coupling are considered [51]. Black, blue, green and red solid curves correspond to $B_0 = 2 \times 10^{-6}$, 1×10^{-6}, 8×10^{-7} and 6×10^{-7} G respectively. The magenta dashed line is corresponds to the EDGES upper bound on T_{21} : -300 mK. The values of $M_{\rm DM}$ and $\hat{\sigma}$ are same as considered in figure (5.5).

and $\hat{\sigma} = 6.22 \times 10^{-15}$ GeV^{-2} constant. In figure (5.5), to plot T_{21} we assume infinite Lyα coupling ($x_\alpha \to \infty \Rightarrow T_S \simeq T_{\rm gas}$) and do not include the x-ray heating. For $B_0 = 1 \times 10^{-6}$ G, the 21 cm line absorption signal reported by EDGES (i.e. -500 mK) can be explained. In figure (5.6), we include the x-ray heating and consider finite Lyα coupling (x_α) [51, 74–76]. As we decrease B_0 from 2×10^{-6} G, the minimum value of T_{21} profile decreases. For the case when $B_0 = 1 \times 10^{-6}$ G (blue solid line), minimum of T_{21} profile is well below the EDGES upper limit on T_{21} (i.e. -300 mK— magenta dashed line). In figure (5.5), when there is infinite Lyα coupling, $T_{21} = -300$ mK corresponds to $B_0 = 1.35 \times 10^{-6}$ G. Thus, we need to lower B_0 values when the finite Lyα coupling is considered to get desired value of T_{21}. As shown in figures (5.5) and (5.6), brightness temperature is suppressed by the increase of the strength of the magnetic field and it can even erase the standard 21 cm signal when the magnetic field strength increases above $\sim 1 \times 10^{-6}$ G. This sets the upper limit on the strength of the magnetic field for $M_{\rm DM} = 10^{-1}$ GeV and $\hat{\sigma} = 6.22 \times 10^{-15}$ GeV^{-2}.

5.3 Conclusions

Magnetic fields in [50, 259] have shown to heat the gas during the cosmic dawn era by the ambipolar diffusion and the turbulence decay. Since, it could erase the observed 21 cm absorption signal, one can calculate the upper bound on the magnetic field. One of the promising mechanisms to explain the absorption signal of the 21 cm line is to have interaction between the dark matter and baryons [73, 345]. In this work, we have shown that in the presence of such an interaction the upper bound on the strength of magnetic fields can significantly be altered. The magnetic-energy converted to the thermal energy and it heats both the gas and dark matter when $\hat{\sigma}$ is non-zero. This is an extra heating effect of dark matter in addition to the drag heating. The drag term heats the dark matter and baryons; but in the lower range of dark matter mass ($\ll 1$ GeV) it becomes small. To

explain the observed anomaly in the 21 cm signal by the EDGES, a large baryon-dark matter scattering cross-section is required to balance the magnetic heating effect. An earlier saturation occurs in baryon-dark matter cross-section in the presence of the strong magnetic fields. We have also explored the millicharged dark matter scenario. In this case, we are not able to reproduce the EDGES signal by considering the upper bound on $\hat{\sigma} - M_{\rm DM}$ by Planck 2015 and CMB-S4 (forecast) [51, 52]. Recently, the similar results about "millicharged" and "Coulomb-like" dark matters also have been obtained in reference [351]. They find that 100% millicharged dark matter scenario can not reproduce the EDGES result for any parameter space. The inclusion of PMFs will further increase the gas temperature and reduce the amplitude of 21-cm absorptional signal. Therefore, it will further worsen the situation for millicharged dark matter scenario.

Considering upper bound on $\hat{\sigma} - M_{\rm DM}$ by Planck 2015 [52] and EDGES upper constraint on T_{21} (-300 mK) at $z = 17$ [5], we found upper bound on the magnetic field strength: $B_0 = 3.48 \times 10^{-6}$ G, while considering CMB-S4 forecast constraint [51] we get $B_0 = 2.67 \times 10^{-6}$ G for the dark matter mass $\lesssim 10^{-2}$ GeV.

"I seem to have been only like a boy playing on the seashore, and diverting myself in now and then finding a smoother pebble or a prettier shell than ordinary, whilst the great ocean of truth lay all undiscovered before me."

Isaac Newton, *"Memoirs of Newton" (1855), Vol II By David Brewster*

6

Summary and Future outlook

6.1 Summary

The 21 cm signal is shown to be a prestigious probe in the cosmological laboratory to provide robust bounds on the physics of the early and late time Universe. The signal can give a good insight into the period when the galaxies and first stars were formed. In the thesis, I have analysed bounds on the present-day strength of primordial magnetic fields, sterile neutrino lifetime & mixing angle with active neutrinos, and primordial black hole dark matter fraction using the global 21 cm signal during the cosmic dawn era. The 21 cm line corresponds to the wavelength of hyperfine transition between 1S singlet and triplet states of the neutral hydrogen atom. The corresponding frequency for the 21 cm line is 1420.4 MHz. For a transition at redshift z, the frequency can be mapped for a present-day observed frequency as $1420.4/(1+z)$.

In the ΛCDM framework of cosmology, the evolution of the gas temperature and ionization fraction are well-established during the cosmic dawn era [153]. The addition of any exotic source of energy can significantly impact the ionization and thermal history of the Universe. The change in the gas temperature can significantly modify the absorption feature in the global 21 cm signal during cosmic dawn [3]. This can provide constraints on the properties of such exotic sources of energy injection.

The EDGES collaboration has reported the 21 cm differential brightness temperature: $T_{21} = -500^{+200}_{-500}$ mK with 99 percent confidence limit centred at 78 MHz or redshift $z = 17.2$ [5]. By considering $T_{\rm S} = T_{\rm gas}$, the observed brightness temperature translates to gas temperature as $T_{\rm gas}(z = 17.2) = 3.26^{+1.94}_{-1.58}$ K. In the ΛCDM framework, the gas temperature at redshift $z = 17.2$ remains around 7 K. This corresponds to differential brightness temperature $T_{21}(z = 17.2) \simeq -220$ mK—equation (1.19) for $T_{\rm S} \simeq T_{\rm gas}$. To resolve the tension between the theoretical prediction based on ΛCDM model and EDGES observation, one requires to increase the ratio of $T_{\rm R}/T_{\rm S}$ in equation (1.19) over theoretical predictions in redshift range $15 \leq z \leq 20$. This can be achieved either by increasing the background radiation or decrease the gas temperature. Both possibilities have been studied by several authors; for example, see the Refs. [25–27, 289, 304, 315–317, 319–321, 325, 326, 345, 346, 352–354]. However, such mechanisms to increase the background radio radiation or cooling the gas are debatable issues. One of such mechanisms to cool gas is baryon dark matter interaction [345]. This approach has been questioned by several authors [51, 73, 340, 349, 355–358]. Here, it is to be noted that the authors do not consider heating of the gas by decaying or annihilating dark matter. Injection of electrons and photons by decaying or annihilating dark matter into IGM can heat the gas more than cooling of the gas [156, 157]. Moreover, the EDGES measurement has been also questioned in several articles [6–8, 77, 78]. Recently, SARAS 3 observation reported that the EDGES observation is not of an astrophysical origin and it is rejected with the 95.3 percent confidence level

[6]. In the Ref. [77], the authors have questioned the fitting parameters for the foreground emission and data. There is a possibility that the absorption feature in the EDGES observation can be a ground screen artifact [7]. The absorption amplitude may modify depending on modelling of foreground [8, 78]. In Ref. [359], the authors perform the Bayesian comparison of fitting models for EDGES data and argue that the highest evidence models favour an amplitude of $|T_{21}| < 209$ mK. In the light of these controversies, it is require to verify the EDGES result by other observations. The future updated version of the hydrogen Epoch of Reionization Array (HERA)[a], Thirty Meter Telescope (TMT)[b], JWST, etc., will be able to probe the cosmic dawn era more precisely. The following summarizes the results reported in the thesis:

6.1.1 Bounds on dark matter candidates

About 85 per cent of the total matter content in the Universe is dominated by dark matter. In the last decades, many dark matter models have been proposed to explain various astrophysical observations. However, the microscopic nature of dark matter is still unknown. During my doctoral research, I have considered sterile neutrinos and primordial black holes as dark matter candidates and constrain their properties using the absorption feature in 21 cm differential brightness temperature during the cosmic dawn era. As discussed earlier, here, we have taken 21 cm differential brightness temperature such that it does not change from its standard theoretical value (~ -220 mK) by more than a factor of 1/4 (i.e. -150 mK) or 1/2 (i.e. -100 mK) at redshift 17.2 .

Sterile Neutrino Dark Matter

In the warm dark matter models, one of the theoretically well-motivated candidates is KeV mass sterile neutrinos. We have constrained the sterile neutrino dark matter

[a] http://reionization.org/
[b] http://tmt.org/

lifetime and mixing angle with active neutrino as a function of sterile neutrino mass [9]. Here, we have considered the two scenarios to get the bounds: First, IGM evolution without the heat transfer from the background radiation to gas mediated by Lyα photons (VDKZ18 effect). Next, we have considered additional VDKZ18 heating effects on the IGM gas. The following summarises our results for $T_{21} = -150$ mK :

In the first scenario, the lower bound on the sterile neutrino lifetime varies from 8.3×10^{27} sec to 9.4×10^{25} sec by varying sterile neutrino mass from 2 KeV to 50 KeV. While the upper bound on the mixing angle varies from 6.8×10^{-9} to 6.1×10^{-14} by varying sterile neutrino mass from 2 KeV to 50 KeV.

In the second scenario, the lower bound on the sterile neutrino lifetime varies from 1.5×10^{28} sec to 1.7×10^{26} sec by varying sterile neutrino mass from 2 KeV to 50 KeV. While the upper bound on the mixing angle varies from 3.8×10^{-9} to 3.42×10^{-14} by varying sterile neutrino mass from 2 KeV to 50 KeV.

Primordial Black Hole Dark Matter

Spinning primordial black holes can substantially affect the ionization and thermal history of the Universe. Subsequently, it can modify the 21 cm absorption signal during cosmic dawn era by injecting energy due to Hawking evaporation. We study the upper projected bounds on the fraction of dark matter in the form of PBHs as a function of mass and spin. Our projected constraints are stringent compared to DSNB, INTEGRAL observation of the 511 KeV line, IGRB, Planck, Leo T and COMPTEL. In the near future, AMEGO collaboration will be able to probe some parameter space in our considered mass range of PBHs. In the present work, we have considered the monochromatic mass distribution of PBHs. The allowed parameter space can also be explored for different PBHs mass distributions such as log-normal, power-law, critical collapse, etc. [251]. We find the most robust lower projected constraint on the mass of PBHs, which is allowed to constitute the entire dark matter, to 1.5×10^{17} g, 1.9×10^{17} g, 3.9×10^{17} g and 6.7×10^{17} g

for PBH spins 0, 0.5, 0.9 and 0.9999, respectively. The lower bound on $M_{\rm PBH}$ for $\Omega_{\rm PBH} = \Omega_{\rm DM}$, for extremal spinning PBHs is nearly four times larger than non-spinning ones [16].

6.1.2 Primordial Magnetic Fields

Observations suggest that the magnetic fields are ubiquitous in the Universe— from the length scale of planets and stars to the cluster of galaxies [17–20]. The origin and evolution of PMFs are one of the outstanding problems of modern cosmology (Ref. [23, 24] and references cited therein). Decaying PMFs can inject magnetic energy into the thermal energy of the IGM and heat the gas. As discussed earlier, the EDGES collaboration reported an absorption profile for the global 21 cm signal with an amplitude of -500^{+200}_{-500} mK in the redshift range $15 - 20$. To explain the EDGES anomaly, one requires to enhance the background radio radiation above the CMB radiation or lower the gas temperature below 3.2 K at redshift ~ 17. We have explored the upper bounds on the present-day strength of the PMFs in both scenarios by considering different models [25, 26].

In the Presence of Excess Radio Radiation

As discussed, one requires to enhance the background radiation above the CMBR to explain the EDGES anomaly. For excess radiation fraction to be LWA 1 limit, we have reported upper bounds on the present-day PMFs strength, B_0 on the scale of 1 Mpc. The following summarises our results for $T_{21} = -500$ mK (EDGES best fit result):

We have reported $B_0 \lesssim 3.7$ nG for spectral index $n_B = -2.99$ for excess radiation fraction to be LWA 1 limit. While for $n_B = -1$, the upper bound gets more stringent: $B_0 \lesssim 1.1 \times 10^{-3}$ nG. We also discuss the effects of first stars on IGM gas evolution and the allowed value of B_0. By decreasing excess radiation fraction below the LWA 1 limit, we get a more stringent bound on B_0 [25].

In the Presence of Baryon-Dark Matter Interaction

One of the alternatives to explain the EDGES anomaly is by cooling the gas below 3.2 K. Since the dark matter is colder than the gas, adequate cooling of the gas can be obtained by introducing the baryon-dark matter interaction beyond the ΛCDM model. The introduction of baryon-dark matter interaction relaxes the upper bound on B_0 by transferring energy of the gas to the dark matter using drag between gas and dark matter. Considering upper bound on $\hat{\sigma} - m_d$ by Planck 2015 and EDGES upper constraint on T_{21} (-300 mK) at $z = 17$, we found upper bound on the present-day strength of PMFs: $B_0 = 3.48 \times 10^{-6}$ G, while considering CMB-S4 forecast constraint we get $B_0 = 2.67 \times 10^{-6}$ G for the dark matter mass $\lesssim 10^{-2}$ GeV. We have also discussed the bounds on $\hat{\sigma} - m_d$ by considering Planck 2018 upper bound on $B_0 \sim 10^{-9}$ G for EDGES best fit and upper bound on T_{21} [26].

6.2 Future work

In my doctoral research, I have analysed the effect of decaying magnetic field on the thermal evolution of the IGM gas using `21cmFAST`[c] code to get the ionization fraction, spin temperature, 21 cm differential brightness temperature in the redshift range $15 - 30$ [70].

It will be interesting to explore the effects of PMFs on the reionization history and parameters. The presence of PMFs can significantly affect the baryon density fluctuations and the Jeans scale [259]. Dark matter is coupled to baryonic matter via gravity. Therefore, the density fluctuations in the baryonic sector subsequently can alter the dark matter density fluctuations. The change in the matter density fluctuations can affect the physics of first stars formation. PMFs in cosmological hydrodynamical simulations can also be a seed for inhomogeneous reionization in

[c] http://homepage.sns.it/mesinger/DexM__21cmFAST.html

the Universe and it can be explored by observations of Lyα forest at lower redshift.

In previous works, I have constrained the PMFs strength by early Universe observations in the redshift range $10 - 30$. Further, these strengths can be constrained more precisely by late time observational constraints. By observing distant galaxies and quasars Lyα forest, the cosmic heating and ionization of IGM can be constrained. Subsequently, using these constraints, the magnetic heating of the IGM gas can also be constrained.

A

A.1 Spin temperature of hydrogen

In the presence of collisions, rate of change in the population of singlet state [2],

$$\frac{dn_{\rm S}}{dt} = -n_{\rm S}\, P^{\rm C}_{\rm ST} + n_{\rm T}\, P^{\rm C}_{\rm TS}\,. \tag{A.1}$$

In the steady state, the transition coefficients from equation (A.1): $n_{\rm T}/n_{\rm S} = P^{\rm C}_{\rm ST}/P^{\rm C}_{\rm TS}$. In the presence of collisions, the spin temperature will be kinetic temperature of gas only. Therefore, from equation (1.5),

$$P^{\rm C}_{\rm ST} = 3\ \exp\left[-\frac{T_{\rm TS}}{T_{\rm gas}}\right] \times P^{\rm C}_{\rm TS} \simeq 3\ \left[1-\frac{T_{\rm TS}}{T_{\rm gas}}\right] \times P^{\rm C}_{\rm TS}\,. \tag{A.2}$$

As discussed in the section (1.2), $T_{\rm gas},\ T_\alpha \gg T_{\rm TS}:\ \exp\left[-T_{\rm TS}/T_{\rm gas}\right] \simeq 1 - T_{\rm TS}/T_{\rm gas}$. Similarly, for the Ly$\alpha$ radiation, $T_{\rm gas}$ and $P^{\rm C}_{\rm TS}$ will be replaced by T_α and $P^{\alpha}_{\rm TS}$,

respectively, in equation (A.2),

$$P^{\alpha}_{\rm ST} \simeq 3 \left[1 - \frac{T_{\rm TS}}{T_{\alpha}}\right] \times P^{\alpha}_{\rm TS} \,. \tag{A.3}$$

In the hydrogen atom, there can be spontaneous and induced emissions by background radiation also,

$$P^{\rm R}_{\rm TS} = A_{10} + B_{10}\, I^{\rm R}_{\nu} \,, \tag{A.4}$$

here, $B_{10}\, I^{\rm R}_{\nu}$ is the induced emission due to background radiation and $I^{\rm R}_{\nu}$ is the specific intensity for 21 cm transition. Here, A_{10} and B_{10} are Einstein coefficients and their relation is given by $A_{10} = 2\,\nu^2_{\rm TS}\, T_{\rm TS}\, B_{10}$. For the background radiation, in the Rayleigh-Jeans limit from equation (1.11): $I^{\rm R}_{\nu} = 2\,\nu^2_{\rm TS}\, T_{\rm R}$. Therefore, from equation (A.4),

$$P^{\rm R}_{\rm TS} = \left(1 + \frac{T_{\rm R}}{T_{\rm TS}}\right) A_{10} \,. \tag{A.5}$$

The induced transition from singlet to triplet due to background radiation [2],

$$P^{\rm R}_{\rm ST} = B_{01}\, I^{\rm R}_{\nu} = 3\, B_{10}\, I^{\rm R}_{\nu} = 3\, A_{10}\, \frac{T_{\rm R}}{T_{\rm TS}} \,. \tag{A.6}$$

Using equations (A.5) and (A.6),

$$\frac{P^{\rm R}_{\rm ST}}{P^{R}_{\rm TS}} \simeq 3 \left[1 - \frac{T_{\rm TS}}{T_{\rm R}}\right] . \tag{A.7}$$

In the detailed balance between the population of 1S singlet and triplet states ($dn_{\rm S}/dt = 0$), by solving the equation (1.6) with the use of equations (1.5), (A.2), (A.3) and (A.7), we get,

$$\left[1 - \frac{T_{\rm TS}}{T_{\rm S}}\right] = \frac{\left[1 - \frac{T_{\rm TS}}{T_{\rm R}}\right] + x_{\alpha}\left[1 - \frac{T_{\rm TS}}{T_{\alpha}}\right] + x_c\left[1 - \frac{T_{\rm TS}}{T_{\rm gas}}\right]}{1 + x_{\alpha} + x_c} \,, \tag{A.8}$$

here, $x_\alpha = P^{\alpha}_{\rm TS}/P^{\rm R}_{\rm TS}$ and $x_c = P^{\rm C}_{\rm TS}/P^{\rm R}_{\rm TS}$. Solving the equation (A.8), we get [2, 3],

$$T_{\rm S}^{-1} = \frac{T_{\rm R}^{-1} + x_\alpha\, T_\alpha^{-1} + x_c\, T_{\rm gas}^{-1}}{1 + x_\alpha + x_c}\,. \tag{A.9}$$

A.2 Emergent brightness temperature

Solving differential equation (1.13) with initial conditions: when, $l = 0 \rightarrow \tau_\nu = 0$ and $I_\nu = I_{\nu_0}$ (figure 1.4),

$$I_\nu = S_\nu\,(1 - e^{-\tau_\nu}) + I_{\nu_0}\, e^{-\tau_\nu}\,. \tag{A.10}$$

Here, using equation (1.11), $I_\nu = 2\,\nu^2\,T'_{\rm R}$ is the final/emergent specific intensity of light— of frequency ν. $S_\nu = 2\,\nu^2\,T_{\rm exc}$ is the specific intensity due to the medium having an excitation temperature, $T_{\rm exc}$, at a frequency of ν. $I_{\nu_0} = 2\,\nu^2\,T_{\rm R}$ is the initial specific intensity of the light. As a result, we find the final/emergent brightness temperature as [2, 3],

$$T'_{\rm R} = T_{\rm exc}\,(1 - e^{-\tau_\nu}) + T_{\rm R}\, e^{-\tau_\nu}\,. \tag{A.11}$$

A.3 Optical depth of hydrogen medium

The radiative transfer equation in the presence of emission and absorption of a light with travelled distance dl in the medium,

$$\frac{dI_\nu}{dl} = \frac{T_{\rm TS}}{4\,\pi}\;\phi(\nu)\;\left[\,n_{\rm T}\,A_{10} + n_{\rm T}\,B_{10}\,I_\nu - n_{\rm S}\,B_{01}\,I_\nu\,\right]\,, \tag{A.12}$$

here, $T_{\rm TS} = 2\,\pi\,\nu_{\rm TS}$, and $\phi(\nu)$ represents line profile of the light beam. $T_{\rm TS}/(4\,\pi)$ represents the energy of light beam per unit solid angle. The first term in the bracket is due to the spontaneous emission from the triplet to the singlet state, and it is proportional to the population density of the triplet state. The second

and third terms in the bracket are due to the stimulated/induced emission and absorption, respectively. Comparing equations (A.12) and (1.12), we get,

$$\alpha_\nu = \frac{T_{\rm TS}}{4\,\pi}\;\phi(\nu)\;\left[\,n_{\rm S}\,B_{01} - n_{\rm T}\,B_{10}\,\right]\,. \tag{A.13}$$

To get the optical depth of hydrogen medium, we can integrate equation (A.13) over dl (equation 1.14),

$$\tau_\nu = \frac{3\,A_{10}}{32\,\pi\,\nu_{\rm TS}^2} \times \frac{T_{\rm TS}}{T_{\rm S}} \times n_{\rm HI} \int \phi(\nu) dl\,, \tag{A.14}$$

here, we have used the relations: $A_{10} = 2\,\nu_{\rm TS}^2\,T_{\rm TS}\,B_{10}$ and $B_{01} = 3\;B_{10}$. As the neutral hydrogen number density: $n_{\rm HI} = n_{\rm S} + n_{\rm T}$, the singlet state population density can be approximated by $n_{\rm S} \simeq n_{\rm HI}/4$— from equation (1.5). The ratio $n_{\rm T}/n_{\rm S}$, has given by equation (1.5). By solving the integral in equation (A.14) for a line profile $\phi(\nu) = 1/\Delta\nu$ with the Doppler shift in the frequency due to the moving medium with a proper velocity v along the line of sight in the comoving coordinate ($\Delta r = (1+z)\,\Delta l$); we find the optical depth for hydrogen medium as [3],

$$\tau_\nu = \frac{3\,n_{\rm HI}}{32\,\pi\,\nu_{\rm TS}^3} \times \frac{T_{\rm TS}}{T_{\rm S}} \times \frac{A_{10}}{H} \times \left[\frac{H/(1+z)}{\partial v/\partial r}\right]\,. \tag{A.15}$$

Here, $\partial v/\partial r$ is the proper velocity gradient along the line of sight, and it can be taken as $H/(1+z)$ for high redshift or in the absence of peculiar velocity. Here, $n_{\rm HI}$ can be written as $x_{\rm HI}\,n_{\rm H}$, and $x_{\rm HI}$ is the neutral hydrogen fraction. The hydrogen number density can be expressed in the form of dimensionless baryon energy density: $n_{\rm H} \simeq 8.5\times10^{-6}\;(1+\delta_{\rm b})\;\Omega_{\rm b}\,h^2\,(1+z)^3\;\;{\rm cm}^{-3}$. Here, $\delta_{\rm b} = (\rho_{\rm b} - \bar{\rho}_{\rm b})/\bar{\rho}_{\rm b}$ is the baryon density contrast. $\rho_{\rm b}$ and $\bar{\rho}_{\rm b}$ are total and average baryon energy density, respectively. For the matter dominated era, we can take $H = H_0\,\sqrt{\Omega_{\rm m}}\;(1+z)^{3/2}$. Here, H_0 and $\Omega_{\rm m}$ are present-day values of Hubble parameter and dimensionless matter energy density parameter, respectively. After some manipulation, we get

the final expression for optical depth of hydrogen medium for 21 cm line [3, 68–71],

$$\tau_\nu \simeq 27\, x_{\rm HI}\, (1+\delta_{\rm b})\, (1+z) \left(\frac{\rm mK}{T_{\rm S}}\right) \left(\frac{0.15}{\Omega_{\rm m}\, h^2}\, \frac{1+z}{10}\right)^{1/2} \left(\frac{\Omega_{\rm b}\, h^2}{0.023}\right) . \qquad \text{(A.16)}$$

For a global 21 cm signal we can take $1 + \delta_{\rm b}$ as ~ 1.

References

[1] H. I. Ewen and E. M. Purcell. Observation of a Line in the Galactic Radio Spectrum: Radiation from Galactic Hydrogen at 1,420 Mc./sec. Nature, 168 (4270):356, 1951. DOI: 10.1038/168356a0.

[2] G. B. Field. Excitation of the hydrogen 21-cm line. Proceedings of the IRE, 46(1):240–250, 1958. DOI: 10.1109/JRPROC.1958.286741.

[3] Jonathan R Pritchard and Abraham Loeb. 21 cm cosmology in the 21st century. Rep. Prog. Phys, 75(8):086901, 2012. DOI: 10.1088/0034-4885/75/8/086901.

[4] S. A. Wouthuysen. On the excitation mechanism of the 21-cm (radio-frequency) interstellar hydrogen emission line. ApJ, 57:31–32, 1952. DOI: 10.1086/106661.

[5] Judd D. Bowman et al. An absorption profile centred at 78 megahertz in the sky-averaged spectrum. Nature, 555(7694):67–70, 2018. DOI: 10.1038/nature25792.

[6] Saurabh Singh, Jishnu Nambissan T., Ravi Subrahmanyan, N. Udaya Shankar, B. S. Girish, A. Raghunathan, R. Somashekar, K. S. Srivani, and Mayuri Sathyanarayana Rao. On the detection of a cosmic dawn signal in the radio background. Nature Astronomy, 6:607–617, 2022. DOI: 10.1038/s41550-022-01610-5.

[7] Richard F. Bradley, Keith Tauscher, David Rapetti, and Jack O. Burns. A ground plane artifact that induces an absorption profile in averaged spectra from global 21 cm measurements, with possible application to edges. ApJ, 874(2):153, 2019. DOI: 10.3847/1538-4357/ab0d8b.

[8] Keith Tauscher, David Rapetti, and Jack O. Burns. Formulating and critically examining the assumptions of global 21 cm signal analyses: How to

avoid the false troughs that can appear in single-spectrum fits. ApJ, 897(2): 132, 2020. DOI: 10.3847/1538-4357/ab9a3f.

[9] Pravin Kumar Natwariya and Alekha C. Nayak. Bounds on sterile neutrino lifetime and mixing angle with active neutrinos by global 21 cm signal. Physics Letters B, 827:136955, 2022. DOI: 10.1016/j.physletb.2022.136955.

[10] John Michell. On the Means of Discovering the Distance, Magnitude, &c. of the Fixed Stars, in Consequence of the Diminution of the Velocity of Their Light, in Case Such a Diminution Should be Found to Take Place in any of Them, and Such Other Data Should be Procured from Observations, as Would be Farther Necessary for That Purpose. By the Rev. John Michell, B. D. F. R. S. In a Letter to Henry Cavendish, Esq. F. R. S. and A. S. Philosophical Transactions of the Royal Society of London, 74:35–57, 1784. URL: https://ui.adsabs.harvard.edu/abs/1784RSPT...74...35M/abstract.

[11] Simon Schaffer. John michell and black holes. Journal for the History of Astronomy, 10:42, 1979. DOI: 10.1177/002182867901000104.

[12] Colin Montgomery, Wayne Orchiston, and Ian Whittingham. Michell, Laplace and the origin of the black hole concept. J. Astron. Hist. Herit., 12 (2):90–96, 2009. URL: https://ui.adsabs.harvard.edu/abs/2009JAHH...12...90M.

[13] Simeon Bird, Ilias Cholis, Julian B. Muñoz, Yacine Ali-Haïmoud, Marc Kamionkowski, Ely D. Kovetz, Alvise Raccanelli, and Adam G. Riess. Did ligo detect dark matter? Phys. Rev. Lett., 116:201301, 2016. DOI: 10.1103/PhysRevLett.116.201301.

[14] B. P. Abbott et al. Gw151226: Observation of gravitational waves from a 22-solar-mass binary black hole coalescence. Phys. Rev. Lett., 116:241103, 2016. DOI: 10.1103/PhysRevLett.116.241103.

[15] Misao Sasaki, Teruaki Suyama, Takahiro Tanaka, and Shuichiro Yokoyama. Primordial black hole scenario for the gravitational-wave event gw150914. Phys. Rev. Lett., 117:061101, 2016. DOI: 10.1103/PhysRevLett.117.061101.

[16] Pravin Kumar Natwariya, Alekha C Nayak, and Tripurari Srivastava. Constraining spinning primordial black holes with global 21-cm signal. MNRAS, 510(3):4236–4241, 2021. DOI: 10.1093/mnras/stab3754.

[17] M. Haverkorn, J. C. Brown, B. M. Gaensler, and N. M. McClure-Griffiths. The outer scale of turbulence in the magnetoionized galactic interstellar medium. ApJ, 680(1):362–370, 2008. DOI: 10.1086/587165.

[18] Andrew Fletcher. Magnetic fields in nearby galaxies, 2011. ASP Conference Series, 438, 197-210.

[19] C. L. Carilli and G. B. Taylor. Cluster magnetic fields. Annual Review of Astronomy and Astrophysics, 40(1):319–348, 2002. DOI: 10.1146/annurev.astro.40.060401.093852.

[20] Axel Brandenburg and Kandaswamy Subramanian. Astrophysical magnetic fields and nonlinear dynamo theory. Physics Reports, 417(1-4):1 – 209, 2005. DOI: 10.1016/j.physrep.2005.06.005.

[21] Andrii Neronov and Ievgen Vovk. Evidence for strong extragalactic magnetic fields from fermi observations of tev blazars. Science, 328(5974):73–75, 2010. DOI: 10.1126/science.1184192.

[22] Ie. Vovk, A. M. Taylor, D. Semikoz, and A. Neronov. Fermi/lat observations of 1es 0229+200: Implications for extragalactic magnetic fields and background light. ApJ, 747(1):L14, 2012. DOI: 10.1088/2041-8205/747/1/l14.

[23] Kandaswamy Subramanian. The origin, evolution and signatures of primordial magnetic fields. Rep. Prog. Phys., 79(7):076901, 2016. DOI: 10.1088/0034-4885/79/7/076901.

[24] Kandaswamy Subramanian. From primordial seed magnetic fields to the galactic dynamo. Galaxies, 7(2), 2019. DOI: 10.3390/galaxies7020047.

[25] Pravin Kumar Natwariya. Constraint on primordial magnetic fields in the light of arcade 2 and edges observations. Eur. Phys. J. C, 81(5):394, 2021. DOI: 10.1140/epjc/s10052-021-09155-z.

[26] Jitesh R. Bhatt, Pravin Kumar Natwariya, Alekha C. Nayak, and Arun Kumar Pandey. Baryon-Dark matter interaction in presence of magnetic fields in light of EDGES signal. Eur. Phys. J. C, 80(4):334, 2020. DOI: 10.1140/epjc/s10052-020-7886-x.

[27] D. J. Fixsen et al. ARCADE 2 MEASUREMENT OF THE ABSOLUTE SKY BRIGHTNESS AT 3-90 GHz. Astrophys. J., 734(1):5, 2011. DOI: 10.1088/0004-637X/734/1/5.

[28] J. Singal et al. The radio synchrotron background: Conference summary and report. Publications of the Astronomical Society of the Pacific, 130 (985):036001, 2018. DOI: 10.1088/1538-3873/aaa6b0.

[29] J. Singal et al. The second radio synchrotron background workshop: Conference summary and report, 2022. DOI: 10.48550/ARXIV.2211.16547.

[30] Jayce Dowell and Greg B. Taylor. The Radio Background below 100 MHz. Astrophys. J., 858(1):L9, 2018. DOI: 10.3847/2041-8213/aabf86.

[31] Jonathan R Pritchard and Abraham Loeb. Hydrogen was not ionized abruptly. Nature, 468:772773, 2010. DOI: 10.1038/468772b.

[32] Joshua S. Dillon. It's Always Darkest Before the Cosmic Dawn: Early Results from Novel Tools and Telescopes for 21 cm Cosmology. PhD thesis, 2015. DOI: 10.48550/ARXIV.1506.03024.

[33] Max Tegmark and Matias Zaldarriaga. Fast fourier transform telescope. Phys. Rev. D, 79:083530, 2009. DOI: 10.1103/PhysRevD.79.083530.

[34] Tejaswi Venumadhav, Liang Dai, Alexander Kaurov, and Matias Zaldarriaga. Heating of the intergalactic medium by the cosmic microwave background during cosmic dawn. Phys. Rev. D, 98:103513, 2018. DOI: 10.1103/PhysRevD.98.103513.

[35] A. Boyarsky, M. Drewes, T. Lasserre, S. Mertens, and O. Ruchayskiy. Sterile neutrino dark matter. Progress in Particle and Nuclear Physics, 104:1 – 45, 2019. DOI: 10.1016/j.ppnp.2018.07.004.

[36] Brandon M. Roach, Kenny C. Y. Ng, Kerstin Perez, John F. Beacom, Shunsaku Horiuchi, Roman Krivonos, and Daniel R. Wik. Nustar tests of sterile-neutrino dark matter: New galactic bulge observations and combined impact. Phys. Rev. D, 101:103011, 2020. DOI: 10.1103/PhysRevD.101.103011.

[37] Brandon M. Roach, Steven Rossland, Kenny C. Y. Ng, Kerstin Perez, John F. Beacom, Brian W. Grefenstette, Shunsaku Horiuchi, Roman Krivonos, and Daniel R. Wik. Long-exposure nustar constraints on decaying dark matter in the galactic halo, 2022. DOI: 10.48550/ARXIV.2207.04572.

[38] Dominic Sicilian, Dannell Lopez, Massimo Moscetti, Esra Bulbul, and Nico Cappelluti. Constraining sterile neutrino dark matter in the milky way halo with swift-xrt, 2022. DOI: 10.48550/ARXIV.2208.12271.

[39] Joshua W. Foster, Marius Kongsore, Christopher Dessert, Yujin Park, Nicholas L. Rodd, Kyle Cranmer, and Benjamin R. Safdi. Deep search for decaying dark matter with xmm-newton blank-sky observations. Phys. Rev. Lett., 127(5), 2021. DOI: 10.1103/physrevlett.127.051101.

[40] Alexandre Arbey, Jérémy Auffinger, and Joseph Silk. Constraining primordial black hole masses with the isotropic gamma ray background. Phys. Rev. D, 101(2), 2020. DOI: 10.1103/physrevd.101.023010.

[41] Basudeb Dasgupta, Ranjan Laha, and Anupam Ray. Neutrino and positron constraints on spinning primordial black hole dark matter. Phys. Rev. Lett., 125:101101, 2020. DOI: 10.1103/PhysRevLett.125.101101.

[42] Anupam Ray, Ranjan Laha, Julian B. Muñoz, and Regina Caputo. Near future mev telescopes can discover asteroid-mass primordial black hole dark matter. Phys. Rev. D, 104:023516, 2021. DOI: 10.1103/PhysRevD.104.023516.

[43] Ranjan Laha, Julian B. Muñoz, and Tracy R. Slatyer. *integral* constraints on primordial black holes and particle dark matter. Phys. Rev. D, 101: 123514, 2020. DOI: 10.1103/PhysRevD.101.123514.

[44] Ranjan Laha. Primordial black holes as a dark matter candidate are severely constrained by the galactic center 511 kev gamma-ray line. Phys. Rev. Lett., 123:251101, 2019. DOI: 10.1103/PhysRevLett.123.251101.

[45] Steven J. Clark, Bhaskar Dutta, Yu Gao, Louis E. Strigari, and Scott Watson. Planck constraint on relic primordial black holes. Phys. Rev. D, 95(8), 2017. DOI: 10.1103/physrevd.95.083006.

[46] Hyungjin Kim. A constraint on light primordial black holes from the interstellar medium temperature. MNRAS, 504(4):5475–5484, 2021. DOI: 10.1093/mnras/stab1222.

[47] Adam Coogan, Logan Morrison, and Stefano Profumo. Direct detection of hawking radiation from asteroid-mass primordial black holes. Phys. Rev. Lett., 126(17), 2021. DOI: 10.1103/physrevlett.126.171101.

[48] Planck Collaboration et al. Planck 2018 results. vi. cosmological parameters. A&A, 641:A6, 2020. DOI: 10.1051/0004-6361/201833910.

[49] Planck Collaboration et al. Planck 2015 results - xix. constraints on primordial magnetic fields. A&A, 594:A19, 2016. DOI: 10.1051/0004-6361/201525821.

[50] Teppei Minoda, Hiroyuki Tashiro, and Tomo Takahashi. Insight into primordial magnetic fields from 21-cm line observation with edges experiment. MNRAS, 488(2):2001–2005, 2019. DOI: 10.1093/mnras/stz1860.

[51] Ely D. Kovetz, Vivian Poulin, Vera Gluscevic, Kimberly K. Boddy, Rennan Barkana, and Marc Kamionkowski. Tighter limits on dark matter explanations of the anomalous EDGES 21 cm signal. Phys. Rev. D, 98(10):103529, 2018. DOI: 10.1103/PhysRevD.98.103529.

[52] Kimberly K. Boddy, Vera Gluscevic, Vivian Poulin, Ely D. Kovetz, Marc Kamionkowski, and Rennan Barkana. Critical assessment of cmb limits on dark matter-baryon scattering: New treatment of the relative bulk velocity. Phys. Rev. D, 98:123506, 2018. DOI: 10.1103/PhysRevD.98.123506.

[53] Planck Collaboration et al. Planck 2015 results. xiii. cosmological parameters. A&A, 594:A13, 2016. DOI: 10.1051/0004-6361/201525830.

[54] Volker Springel et al. Simulations of the formation, evolution and clustering of galaxies and quasars. Nature, 435(7042):629–636, 2005. DOI: 10.1038/nature03597.

[55] D. N. Spergel et al. First-year wilkinson microwave anisotropy probe (wmap)* observations: Determination of cosmological parameters. ApJ Supplement Series, 148(1):175–194, 2003. DOI: 10.1086/377226.

[56] D. N. Spergel et al. Three-year wilkinson microwave anisotropy probe (wmap) observations: Implications for cosmology. ApJ Supplement Series, 170(2):377–408, 2007. DOI: 10.1086/513700.

[57] N. Jarosik et al. Seven-year wilkinson microwave anisotropy probe (wmap*) observations: Sky maps, systematic errors, and basic results. ApJ Supplement Series, 192(2):14, 2011. DOI: 10.1088/0067-0049/192/2/14.

[58] Adam G. Riess et al. Observational evidence from supernovae for an accelerating universe and a cosmological constant. The Astronomical Journal, 116 (3):1009–1038, 1998. DOI: 10.1086/300499.

[59] S. Perlmutter et al. Measurements of ω and λ from 42 high-redshift supernovae. ApJ, 517(2):565–586, 1999. DOI: 10.1086/307221.

[60] C. L. Bennett et al. Scientific results from the cosmic background explorer (cobe). Proceedings of the National Academy of Sciences, 90(11):4766–4773, 1993. DOI: 10.1073/pnas.90.11.4766.

[61] Alan H. Guth. Inflationary universe: A possible solution to the horizon and flatness problems. Phys. Rev. D, 23:347–356, 1981. DOI: 10.1103/PhysRevD.23.347.

[62] A.D. Linde. A new inflationary universe scenario: A possible solution of the horizon, flatness, homogeneity, isotropy and primordial monopole problems. Physics Letters B, 108(6):389–393, 1982. DOI: 10.1016/0370-2693(82)91219-9.

[63] Edward W. Kolb and Michael S. Turner. The Early Universe, volume 69. 1990. ISBN 978-0-201-62674-2. DOI: 10.1201/9780429492860.

[64] P. J. E. Peebles and Bharat Ratra. The cosmological constant and dark energy. Rev. Mod. Phys., 75:559–606, 2003. DOI: 10.1103/RevModPhys.75.559.

[65] H. C. van de Hulst. Radiogolven uit het wereldruim: II. Herkomst der radiogolvenRadiogolven uit het wereldruim: II. Herkomst der radiogolven-Radio waves from space. Nederlandsch Tijdschrift voor Natuurkunde, 11: 210–221, 1945. URL: https://ui.adsabs.harvard.edu/abs/1945NTvN...11..210V.

[66] G. B. Field. The Spin Temperature of Intergalactic Neutral Hydrogen. ApJ, 129:536, 1959. DOI: 10.1086/146653.

[67] Steven R. Furlanetto, S. Peng Oh, and Frank H. Briggs. Cosmology at low frequencies: The 21cm transition and the high-redshift universe. Physics Reports, 433(4-6):181–301, 2006. DOI: 10.1016/j.physrep.2006.08.002.

[68] Matias Zaldarriaga, Steven R. Furlanetto, and Lars Hernquist. 21 centimeter fluctuations from cosmic gas at high redshifts. ApJ, 608(2):622–635, 2004. DOI: 10.1086/386327.

[69] Andrei Mesinger and Steven Furlanetto. Efficient simulations of early structure formation and reionization. ApJ, 669(2):663–675, 2007. DOI: 10.1086/521806.

[70] Andrei Mesinger, Steven Furlanetto, and Renyue Cen. 21cmfast: a fast, seminumerical simulation of the high-redshift 21-cm signal. MNRAS, 411 (2):955–972, 2011. DOI: 10.1111/j.1365-2966.2010.17731.x.

[71] Shikhar Mittal and Girish Kulkarni. Lyα coupling and heating at cosmic dawn. MNRAS, 503(3):4264–4275, 2020. DOI: 10.1093/mnras/staa3811.

[72] P. J. E. Peebles. Principles of physical cosmology. Princeton University Press, 1993. ISBN 0691074283. URL: https://trove.nla.gov.au/work/22461641.

[73] Rennan Barkana, Nadav Joseph Outmezguine, Diego Redigolo, and Tomer Volansky. Strong constraints on light dark matter interpretation of the edges signal. Phys. Rev. D, 98:103005, 2018. DOI: 10.1103/PhysRevD.98.103005.

[74] Jordan Mirocha, Geraint J. A. Harker, and Jack O. Burns. INTERPRETING THE GLOBAL 21-cm SIGNAL FROM HIGH REDSHIFTS. II. PARAMETER ESTIMATION FOR MODELS OF GALAXY FORMATION. ApJ, 813(1):11, 2015. DOI: 10.1088/0004-637x/813/1/11.

[75] Geraint J. A. Harker, Jordan Mirocha, Jack O. Burns, and Jonathan R. Pritchard. Parametrizations of the 21-cm global signal and parameter estimation from single-dipole experiments. MNRAS, 455(4):3829–3840, 2015. DOI: 10.1093/mnras/stv2630.

[76] B. Zygelman. Hyperfine level–changing collisions of hydrogen atoms and tomography of the dark age universe. ApJ, 622(2):1356–1362, 2005. DOI: 10.1086/427682.

[77] Richard Hills, Girish Kulkarni, P. Daniel Meerburg, and Ewald Puchwein. Concerns about modelling of the edges data. Nature, 564(7736):E32E34, 2018. DOI: 10.1038/s41586-018-0796-5.

[78] Saurabh Singh and Ravi Subrahmanyan. The redshifted 21 cm signal in the edges low-band spectrum. ApJ, 880(1):26, 2019. DOI: 10.3847/1538-4357/ab2879.

[79] James S Bullock and Michael Boylan-Kolchin. Small-Scale Challenges to the ΛCDM Paradigm. Annu. Rev. Astron. Astrophys., 55(1):343–387, 2017. DOI: 10.1146/annurev-astro-091916-055313.

[80] Anatoly A. Klypin, Andrey V. Kravtsov, Octavio Valenzuela, and Francisco Prada. Where are the missing Galactic satellites? Astrophys. J., 522:82–92, 1999. DOI: 10.1086/307643.

[81] B Moore, S Ghigna, F Governato, G Lake, Thomas R Quinn, J Stadel, and P Tozzi. Dark matter substructure within galactic halos. Astrophys. J., 524: 19–22, 1999. DOI: 10.1086/312287.

[82] Michael Boylan-Kolchin, James S Bullock, and Manoj Kaplinghat. Too big to fail? The puzzling darkness of massive Milky Way subhaloes. MNARS Lett., 415(1):L40–L44, 2011. DOI: 10.1111/j.1745-3933.2011.01074.x.

[83] Michael Boylan-Kolchin, James S Bullock, and Manoj Kaplinghat. The Milky Way's bright satellites as an apparent failure of ΛCDM. Mon. Not. R. Astron. Soc., 422(2):1203–1218, 2012. DOI: 10.1111/j.1365-2966.2012.20695.x.

[84] W J G de Blok. The Core-Cusp Problem. Adv. Astron., 2010:789293, 2010. DOI: 10.1155/2010/789293.

[85] A. Drlica-Wagner et al. Milky way satellite census. i. the observational selection function for milky way satellites in des y3 and pan-starrs dr1. ApJ, 893(1):47, 2020. DOI: 10.3847/1538-4357/ab7eb9.

[86] E. Papastergis and F. Shankar. An assessment of the too big to fail problem for field dwarf galaxies in view of baryonic feedback effects. A&A, 591:A58, 2016. DOI: 10.1051/0004-6361/201527854.

[87] David N Spergel and Paul J Steinhardt. Observational Evidence for Self-Interacting Cold Dark Matter. Phys. Rev. Lett., 84(17):3760–3763, 2000. DOI: 10.1103/PhysRevLett.84.3760.

[88] Sean Tulin and Hai-Bo Yu. Dark Matter Self-interactions and Small Scale Structure. Phys. Rept., 730:1–57, 2018. DOI: 10.1016/j.physrep.2017.11.004.

[89] Manoj Kaplinghat, Sean Tulin, and Hai-Bo Yu. Dark Matter Halos as Particle Colliders: Unified Solution to Small-Scale Structure Puzzles from Dwarfs to Clusters. Phys. Rev. Lett., 116(4):41302, 2016. DOI: 10.1103/PhysRevLett.116.041302.

[90] Pravin Kumar Natwariya, Jitesh R. Bhatt, and Arun Kumar Pandey. Viscosity in cosmic fluids. Eur. Phys. J. C, 80(8):767, 2020. DOI: 10.1140/epjc/s10052-020-8341-8.

[91] Wayne Hu, Rennan Barkana, and Andrei Gruzinov. Fuzzy cold dark matter: The wave properties of ultralight particles. Phys. Rev. Lett., 85:1158–1161, 2000. DOI: 10.1103/PhysRevLett.85.1158.

[92] Hsi-Yu Schive, Tzihong Chiueh, and Tom Broadhurst. Cosmic structure as the quantum interference of a coherent dark wave. Nature Physics, 10(7): 496–499, 2014. DOI: 10.1038/nphys2996.

[93] G. R. Blumenthal, H. Pagels, and J. R. Primack. Galaxy formation by dissipationless particles heavier than neutrinos. Nature, 299(5878):37–38, 1982. DOI: 10.1038/299037a0.

[94] Scott Dodelson and Lawrence M. Widrow. Sterile neutrinos as dark matter. Phys. Rev. Lett., 72:17–20, 1994. DOI: 10.1103/PhysRevLett.72.17.

[95] Stephane Colombi, Scott Dodelson, and Lawrence M. Widrow. Large-scale structure tests of warm dark matter. ApJ, 458:1, 1996. DOI: 10.1086/176788.

[96] Michael Sitwell, Andrei Mesinger, Yin-Zhe Ma, and Kris Sigurdson. The imprint of warm dark matter on the cosmological 21-cm signal. MNRAS, 438(3):2664–2671, 2014. DOI: 10.1093/mnras/stt2392.

[97] Vedran Brdar, Joachim Kopp, Jia Liu, and Xiao-Ping Wang. X-ray lines from dark matter annihilation at the kev scale. Phys. Rev. Lett., 120:061301, 2018. DOI: 10.1103/PhysRevLett.120.061301.

[98] Marc S Seigar. Cold dark matter, hot dark matter, and their alternatives. In Dark Matter in the Universe, 2053-2571, pages 3–1 to 3–9. Morgan & Claypool Publishers, 2015. ISBN 978-1-6817-4118-5. DOI: 10.1088/978-1-6817-4118-5ch3.

[99] Aurel Schneider, Robert E. Smith, Andrea V. Macciò, and Ben Moore. Non-linear evolution of cosmological structures in warm dark matter models. MNRAS, 424(1):684–698, 2012. DOI: 10.1111/j.1365-2966.2012.21252.x.

[100] Martin Götz. Astrophysics and Space Science, 284(2):341344, 2003. DOI: 10.1023/a:1024073909753.

[101] Paul Bode, Jeremiah P. Ostriker, and Neil Turok. Halo formation in warm dark matter models. ApJ, 556(1):93–107, 2001. DOI: 10.1086/321541.

[102] Mark R. Lovell, Violeta Gonzalez-Perez, Sownak Bose, Alexey Boyarsky, Shaun Cole, Carlos S. Frenk, and Oleg Ruchayskiy. Addressing the too big to fail problem with baryon physics and sterile neutrino dark matter. MNRAS, 468(3):28362849, 2017. DOI: 10.1093/mnras/stx621.

[103] Andrea V. Macciò, Sinziana Paduroiu, Donnino Anderhalden, Aurel Schneider, and Ben Moore. Cores in warm dark matter haloes: a Catch 22 problem. MNRAS, 424(2):1105–1112, 2012. DOI: 10.1111/j.1365-2966.2012.21284.x.

[104] Mark R. Lovell, Vincent Eke, Carlos S. Frenk, Liang Gao, Adrian Jenkins, Tom Theuns, Jie Wang, Simon D. M. White, Alexey Boyarsky, and Oleg Ruchayskiy. The haloes of bright satellite galaxies in a warm dark matter universe. MNRAS, 420(3):2318–2324, 2012. DOI: 10.1111/j.1365-2966.2011.20200.x.

[105] Esra Bulbul, Maxim Markevitch, Adam Foster, Randall K. Smith, Michael Loewenstein, and Scott W. Randall. DETECTION OF AN UNIDENTIFIED EMISSION LINE IN THE STACKED x-RAY SPECTRUM OF GALAXY CLUSTERS. ApJ, 789(1):13, 2014. DOI: 10.1088/0004-637x/789/1/13.

[106] A. Boyarsky, O. Ruchayskiy, D. Iakubovskyi, and J. Franse. Unidentified line in x-ray spectra of the andromeda galaxy and perseus galaxy cluster. Phys. Rev. Lett., 113:251301, 2014. DOI: 10.1103/PhysRevLett.113.251301.

[107] A. Boyarsky, J. Franse, D. Iakubovskyi, and O. Ruchayskiy. Checking the dark matter origin of a 3.53 kev line with the milky way center. Phys. Rev. Lett., 115:161301, 2015. DOI: 10.1103/PhysRevLett.115.161301.

[108] E. M. Silich, K. Jahoda, L. Angelini, P. Kaaret, A. Zajczyk, D. M. LaRocca, R. Ringuette, and J. Richardson. A search for the 3.5 kev line from the milky ways dark matter halo with halosat. ApJ, 916(1):2, 2021. DOI: 10.3847/1538-4357/ac043b.

[109] R. Adhikari and others. A white paper on keV sterile neutrino dark matter. J. Cosmol. Astropart. Phys., 2017(01):025–025, 2017. DOI: 10.1088/1475-7516/2017/01/025.

[110] Kevork N. Abazajian. Sterile neutrinos in cosmology. Physics Reports, 711-712:1–28, 2017. DOI: 10.1016/j.physrep.2017.10.003.

[111] B. Pontecorvo. Mesonium and Antimesonium. Soviet Journal of Experimental and Theoretical Physics, 6:429, 1958. URL: https://ui.adsabs.harvard.edu/abs/1958JETP....6..429P.

[112] Ziro Maki, Masami Nakagawa, and Shoichi Sakata. Remarks on the Unified Model of Elementary Particles. Progress of Theoretical Physics, 28(5):870–880, 1962. DOI: 10.1143/PTP.28.870.

[113] B. Pontecorvo. Neutrino Experiments and the Problem of Conservation of Leptonic Charge. Soviet Journal of Experimental and Theoretical Physics,

26:984, 1968. URL: https://ui.adsabs.harvard.edu/abs/1968JETP...26..984P.

[114] John N. Bahcall and Raymond Davis. Solar neutrinos: A scientific puzzle. Science, 191(4224):264–267, 1976. DOI: 10.1126/science.191.4224.264.

[115] A Yu Smirnov. Neutrino mass and new physics. Journal of Physics: Conference Series, 53:4482, 2006. DOI: 10.1088/1742-6596/53/1/003.

[116] Julien Lesgourgues and Sergio Pastor. Massive neutrinos and cosmology. Physics Reports, 429(6):307–379, 2006. DOI: 10.1016/j.physrep.2006.04.001.

[117] Y. Ashie et al. Evidence for an oscillatory signature in atmospheric neutrino oscillations. Phys. Rev. Lett., 93:101801, 2004. DOI: 10.1103/PhysRevLett.93.101801.

[118] Y. Ashie et al. Measurement of atmospheric neutrino oscillation parameters by super-kamiokande i. Phys. Rev. D, 71:112005, 2005. DOI: 10.1103/PhysRevD.71.112005.

[119] B. Aharmim et al. Electron energy spectra, fluxes, and day-night asymmetries of ^{8}b solar neutrinos from measurements with nacl dissolved in the heavy-water detector at the sudbury neutrino observatory. Phys. Rev. C, 72:055502, 2005. DOI: 10.1103/PhysRevC.72.055502.

[120] B. Aharmim et al. Search for periodicities in the ^{8}b solar neutrino flux measured by the sudbury neutrino observatory. Phys. Rev. D, 72:052010, 2005. DOI: 10.1103/PhysRevD.72.052010.

[121] F. Capozzi, E. Lisi, A. Marrone, D. Montanino, and A. Palazzo. Neutrino masses and mixings: Status of known and unknown 3ν parameters. Nuclear Physics B, 908:218–234, 2016. DOI: 10.1016/j.nuclphysb.2016.02.016. Neutrino Oscillations: Celebrating the Nobel Prize in Physics 2015.

[122] Particle Data Group. Review of Particle Physics. Progress of Theoretical and Experimental Physics, 2020(8), 2020. DOI: 10.1093/ptep/ptaa104. 083C01.

[123] Basudeb Dasgupta and Joachim Kopp. Sterile neutrinos. Physics Reports, 928:163, 2021. DOI: 10.1016/j.physrep.2021.06.002.

[124] MARCO DREWES. The phenomenology of right handed neutrinos. International Journal of Modern Physics E, 22(08):1330019, 2013. DOI: 10.1142/s0218301313300191.

[125] Takehiko Asaka and Mikhail Shaposhnikov. The νmsm, dark matter and baryon asymmetry of the universe. Physics Letters B, 620(1):17–26, 2005. DOI: 10.1016/j.physletb.2005.06.020.

[126] ALEXANDER MERLE. keV NEUTRINO MODEL BUILDING. International Journal of Modern Physics D, 22(10):1330020, 2013. DOI: 10.1142/s0218271813300206.

[127] Xiangdong Shi and George M. Fuller. New dark matter candidate: Non-thermal sterile neutrinos. Phys. Rev. Lett., 82:2832–2835, 1999. DOI: 10.1103/PhysRevLett.82.2832.

[128] A.D. Dolgov and S.H. Hansen. Massive sterile neutrinos as warm dark matter. Astroparticle Physics, 16(3):339 – 344, 2002. DOI: 10.1016/S0927-6505(01)00115-3.

[129] Andrea Caputo, Marco Regis, and Marco Taoso. Searching for sterile neutrino with X-ray intensity mapping. J. Cosmol. Astropart. Phys., 2020(3): 001, 2020. DOI: 10.1088/1475-7516/2020/03/001.

[130] Charles Thorpe-Morgan, Denys Malyshev, Andrea Santangelo, Josef Jochum, Barbara Jäger, Manami Sasaki, and Sara Saeedi. Theseus insights into axionlike particles, dark photon, and sterile neutrino dark matter. Phys. Rev. D, 102:123003, 2020. DOI: 10.1103/PhysRevD.102.123003.

[131] Ilídio Lopes. The sun: Light dark matter and sterile neutrinos. ApJ, 905(1): 22, 2020. DOI: 10.3847/1538-4357/abbfb6.

[132] André de Gouvêa, O. L. G. Peres, Suprabh Prakash, and G. V. Stenico. On the decaying-sterile-neutrino solution to the electron (anti)neutrino appearance anomalies. Journal of High Energy Physics, 2020(7), 2020. DOI: 10.1007/jhep07(2020)141.

[133] Osamu Seto and Takashi Shimomura. Signal from sterile neutrino dark matter in extra u(1) model at direct detection experiment. Physics Letters B, 811:135880, 2020. DOI: 10.1016/j.physletb.2020.135880.

[134] Alexey Boyarsky, Oleg Ruchayskiy, and Dmytro Iakubovskyi. A lower bound on the mass of dark matter particles. Journal of Cosmology and Astroparticle Physics, 2009(03):005005, 2009. DOI: 10.1088/1475-7516/2009/03/005.

[135] Venno Vipp, Andi Hektor, and Gert Hütsi. Rapid onset of the 21-cm signal suggests a preferred mass range for dark matter particle. Phys. Rev. D, 103 (12), 2021. DOI: 10.1103/physrevd.103.123002.

[136] Matteo Viel, Julien Lesgourgues, Martin G. Haehnelt, Sabino Matarrese, and Antonio Riotto. Constraining warm dark matter candidates including sterile neutrinos and light gravitinos with wmap and the lyman-alpha forest. Phys. Rev. D, 71:063534, 2005. DOI: 10.1103/PhysRevD.71.063534.

[137] Kevork Abazajian and Savvas M. Koushiappas. Constraints on sterile neutrino dark matter. Phys. Rev. D, 74:023527, 2006. DOI: 10.1103/PhysRevD.74.023527.

[138] Uro š Seljak, Alexey Makarov, Patrick McDonald, and Hy Trac. Can sterile neutrinos be the dark matter? Phys. Rev. Lett., 97:191303, 2006. DOI: 10.1103/PhysRevLett.97.191303.

[139] Alexey Boyarsky, Julien Lesgourgues, Oleg Ruchayskiy, and Matteo Viel. Lyman-alpha constraints on warm and on warm-plus-cold dark matter models. JCAP, 2009(05):012–012, 2009. DOI: 10.1088/1475-7516/2009/05/012.

[140] Matteo Viel, George D. Becker, James S. Bolton, and Martin G. Haehnelt. Warm dark matter as a solution to the small scale crisis: New constraints from high redshift lyman-α forest data. Physical Review D, 88(4), 2013. DOI: 10.1103/physrevd.88.043502.

[141] Andrea V. Macciò and Fabio Fontanot. How cold is dark matter? Constraints from Milky Way satellites. MNRAS, 404(1):L16–L20, 2010. DOI: 10.1111/j.1745-3933.2010.00825.x.

[142] Emil Polisensky and Massimo Ricotti. Constraints on the dark matter particle mass from the number of milky way satellites. Phys. Rev. D, 83:043506, 2011. DOI: 10.1103/PhysRevD.83.043506.

[143] A. Boyarsky, D. Iakubovskyi, O. Ruchayskiy, A. Rudakovskyi, and W. Valkenburg. 21-cm observations and warm dark matter models. Phys. Rev. D, 100:123005, 2019. DOI: 10.1103/PhysRevD.100.123005.

[144] Alberto Salvio and Simone Scollo. Axion-sterile-neutrino dark matter, 2021.

[145] K. N. Abazajian et al. Light sterile neutrinos: A white paper, 2012.

[146] Subinoy Das, Rajesh Mondal, Vikram Rentala, and Srikanth Suresh. On dark matter-dark radiation interaction and cosmic reionization. J. Cosmol. Astropart. Phys., 2018(08):045–045, 2018. DOI: 10.1088/1475-7516/2018/08/045.

[147] Soroush Shakeri, Fazlollah Hajkarim, and She-Sheng Xue. Shedding new light on sterile neutrinos from xenon1t experiment. Journal of High Energy Physics, 2020(12), 2020. DOI: 10.1007/jhep12(2020)194.

[148] Laura Lopez-Honorez, Olga Mena, Sergio Palomares-Ruiz, and Pablo Villanueva-Domingo. Warm dark matter and the ionization history of the universe. Phys. Rev. D, 96(10), 2017. DOI: 10.1103/physrevd.96.103539.

[149] S Vegetti, G Despali, M R Lovell, and W Enzi. Constraining sterile neutrino cosmologies with strong gravitational lensing observations at redshift z $\sim$ 0.2. MNRAS, 481(3):3661–3669, 2018. DOI: 10.1093/mnras/sty2393.

[150] A Rudakovskyi and D Iakubovskyi. Dark matter model favoured by reionization data: 7 kev sterile neutrino versus cold dark matter. MNRAS, 483 (3):4080–4084, 2018. DOI: 10.1093/mnras/sty3057.

[151] F. Bezrukov, A. Chudaykin, and D. Gorbunov. Hiding an elephant: heavy sterile neutrino with large mixing angle does not contradict cosmology. J. Cosmol. Astropart. Phys., 2017(06):051–051, 2017. DOI: 10.1088/1475-7516/2017/06/051.

[152] Boyarsky, A., Nevalainen, J., and Ruchayskiy, O. Constraints on the parameters of radiatively decaying dark matter from the dark matter halos of the milky way and ursa minor. A&A, 471(1):51–57, 2007. DOI: 10.1051/0004-6361:20066774.

[153] S. Seager, D. D. Sasselov, and D. Scott. A New Calculation of the Recombination Epoch. Ast. J., 523(1):L1–L5, 1999. DOI: 10.1086/312250.

[154] Sara Seager, Dimitar D. Sasselov, and Douglas Scott. How exactly did the universe become neutral? ApJ, 128(2):407–430, 2000. DOI: 10.1086/313388.

[155] Hongwan Liu and Tracy R. Slatyer. Implications of a 21-cm signal for dark matter annihilation and decay. Phys. Rev. D, 98:023501, 2018. DOI: 10.1103/PhysRevD.98.023501.

[156] Andrea Mitridate and Alessandro Podo. Bounds on dark matter decay from 21 cm line. J. Cosmol. Astropart. Phys., 2018(05):069–069, 2018. DOI: 10.1088/1475-7516/2018/05/069.

[157] Guido D'Amico, Paolo Panci, and Alessandro Strumia. Bounds on dark-matter annihilations from 21-cm data. Phys. Rev. Lett., 121:011103, 2018. DOI: 10.1103/PhysRevLett.121.011103.

[158] Yacine Ali-Haimoud and Christopher M. Hirata. HyRec: A fast and highly accurate primordial hydrogen and helium recombination code. Phys. Rev., D83:043513, 2011. DOI: 10.1103/PhysRevD.83.043513.

[159] Silvia Galli, Fabio Iocco, Gianfranco Bertone, and Alessandro Melchiorri. Cmb constraints on dark matter models with large annihilation cross section. Phys. Rev. D, 80:023505, 2009. DOI: 10.1103/PhysRevD.80.023505.

[160] P. J. E. Peebles. Recombination of the Primeval Plasma. Astrophys. J., 153: 1, 1968. DOI: 10.1086/149628.

[161] J. H. Tung, X. M. Salamo, and F. T. Chan. Two-photon decay of hydrogenic atoms. Phys. Rev. A, 30:1175–1184, 1984. DOI: 10.1103/PhysRevA.30.1175.

[162] E. Ripamonti, M. Mapelli, and A. Ferrara. Intergalactic medium heating by dark matter. MNRAS, 374(3):1067–1077, 2006. DOI: 10.1111/j.1365-2966.2006.11222.x.

[163] M. Mapelli and A. Ferrara. Background radiation from sterile neutrino decay and reionization. MNRAS, 364(1):2–12, 2005. DOI: 10.1111/j.1365-2966.2005.09507.x.

[164] Xuelei Chen and Marc Kamionkowski. Particle decays during the cosmic dark ages. Phys. Rev. D, 70(4), 2004. DOI: 10.1103/physrevd.70.043502.

[165] J. M. Shull and M. E. van Steenberg. X-ray secondary heating and ionization in quasar emission-line clouds. ApJ, 298:268–274, 1985. DOI: 10.1086/163605.

[166] M. Mapelli, A. Ferrara, and E. Pierpaoli. Impact of dark matter decays and annihilations on reionization. MNRAS, 369(4):1719–1724, 2006. DOI: 10.1111/j.1365-2966.2006.10408.x.

[167] Karl Schwarzschild. On the gravitational field of a mass point according to Einstein's theory. Sitzungsber. Preuss. Akad. Wiss. Berlin (Math. Phys.), 1916:189–196, 1916. Translated by S. Antoci and A. Loinger.

[168] Roy P. Kerr. Gravitational field of a spinning mass as an example of algebraically special metrics. Phys. Rev. Lett., 11:237–238, 1963. DOI: 10.1103/PhysRevLett.11.237.

[169] E. T. Newman, E. Couch, K. Chinnapared, A. Exton, A. Prakash, and R. Torrence. Metric of a rotating, charged mass. Journal of Mathematical Physics, 6(6):918–919, 1965. DOI: 10.1063/1.1704351.

[170] Ya. B. Zel'dovich and I. D. Novikov. The Hypothesis of Cores Retarded during Expansion and the Hot Cosmological Model. Soviet Astronomy, 10: 602, 1967. URL: https://ui.adsabs.harvard.edu/abs/1967SvA....10..602Z.

[171] Stephen Hawking. Gravitationally Collapsed Objects of Very Low Mass. MNRAS, 152(1):75–78, 1971. DOI: 10.1093/mnras/152.1.75.

[172] B. J. Carr and S. W. Hawking. Black holes in the early universe. MNRAS, 168(2):399–415, 1974. DOI: 10.1093/mnras/168.2.399.

[173] B. J. Carr. The primordial black hole mass spectrum. ApJ, 201:1–19, 1975. DOI: 10.1086/153853.

[174] Alexander Vilenkin. Cosmological density fluctuations produced by vacuum strings. Phys. Rev. Lett., 46:1169–1172, 1981. DOI: 10.1103/PhysRevLett.46.1169.

[175] S.W. Hawking. Black holes from cosmic strings. Physics Letters B, 231(3): 237–239, 1989. DOI: 10.1016/0370-2693(89)90206-2.

[176] Alexander Polnarev and Robert Zembowicz. Formation of primordial black holes by cosmic strings. Phys. Rev. D, 43:1106–1109, 1991. DOI: 10.1103/PhysRevD.43.1106.

[177] S.W. Hawking. Gravitational radiation from collapsing cosmic string loops. Physics Letters B, 246(1):36–38, 1990. DOI: 10.1016/0370-2693(90)91304-T.

[178] Jaume Garriga and Alexander Vilenkin. Black holes from nucleating strings. Phys. Rev. D, 47:3265–3274, 1993. DOI: 10.1103/PhysRevD.47.3265.

[179] Ubi F Wichoski, Jane H MacGibbon, and Robert H Brandenberger. Astrophysical constraints on primordial black hole formation from collapsing cosmic strings. Physics Reports, 307(1):191–196, 1998. DOI: 10.1016/S0370-1573(98)00070-2.

[180] Alexander C. Jenkins and Mairi Sakellariadou. Primordial black holes from cusp collapse on cosmic strings, 2020.

[181] S. W. Hawking, I. G. Moss, and J. M. Stewart. Bubble collisions in the very early universe. Phys. Rev. D, 26:2681–2693, 1982. DOI: 10.1103/PhysRevD.26.2681.

[182] Daile La and Paul J. Steinhardt. Bubble percolation in extended inflationary models. Physics Letters B, 220(3):375–378, 1989. DOI: 10.1016/0370-2693(89)90890-3.

[183] Tae Hyun Jung and Takemichi Okui. Primordial black holes from bubble collisions during a first-order phase transition, 2021.

[184] Paul H Frampton, Masahiro Kawasaki, Fuminobu Takahashi, and Tsutomu T Yanagida. Primordial black holes as all dark matter. J. Cosmol. Astropart. Phys., 2010(04):023–023, 2010. DOI: 10.1088/1475-7516/2010/04/023.

[185] Sébastien Clesse and Juan García-Bellido. Massive primordial black holes from hybrid inflation as dark matter and the seeds of galaxies. Phys. Rev. D, 92:023524, 2015. DOI: 10.1103/PhysRevD.92.023524.

[186] Keisuke Inomata, Masahiro Kawasaki, Kyohei Mukaida, and Tsutomu T. Yanagida. Double inflation as a single origin of primordial black holes for all dark matter and ligo observations. Phys. Rev. D, 97:043514, 2018. DOI: 10.1103/PhysRevD.97.043514.

[187] Bernard Carr, Kazunori Kohri, Yuuiti Sendouda, and Junichi Yokoyama. Constraints on primordial black holes. Rep. Prog. Phys., 84(11):116902, 2021. DOI: 10.1088/1361-6633/ac1e31.

[188] B. J. Carr, Kazunori Kohri, Yuuiti Sendouda, and Jun'ichi Yokoyama. New cosmological constraints on primordial black holes. Phys. Rev. D, 81:104019, 2010. DOI: 10.1103/PhysRevD.81.104019.

[189] Anne M. Green. Primordial black holes: Sirens of the early universe. Quantum Aspects of Black Holes, page 129149, 2014. DOI: 10.1007/978-3-319-10852-0_5.

[190] P. Agnes et al. First results from the darkside-50 dark matter experiment at laboratori nazionali del gran sasso. Physics Letters B, 743:456–466, 2015. DOI: 10.1016/j.physletb.2015.03.012.

[191] D. S. Akerib et al. Results from a search for dark matter in the complete lux exposure. Phys. Rev. Lett., 118:021303, 2017. DOI: 10.1103/PhysRevLett.118.021303.

[192] E. Aprile et al. First dark matter search results from the xenon1t experiment. Phys. Rev. Lett., 119(18), 2017. DOI: 10.1103/physrevlett.119.181301.

[193] Xiangyi Cui et al. Dark matter results from 54-ton-day exposure of pandax-ii experiment. Phys. Rev. Lett., 119(18), 2017. DOI: 10.1103/physrevlett.119.181302.

[194] A. H. Abdelhameed et al. First results from the cresst-iii low-mass dark matter program. Phys. Rev. D, 100:102002, 2019. DOI: 10.1103/PhysRevD.100.102002.

[195] C. Amole et al. Dark matter search results from the complete exposure of the PICO-60 C_3F_8 bubble chamber. Phys. Rev. D, 100:022001, 2019. DOI: 10.1103/PhysRevD.100.022001.

[196] B. P. Abbott et al. Observation of gravitational waves from a binary black hole merger. Phys. Rev. Lett., 116:061102, 2016. DOI: 10.1103/PhysRevLett.116.061102.

[197] B. P. Abbott et al. Gw170104: Observation of a 50-solar-mass binary black hole coalescence at redshift 0.2. Phys. Rev. Lett., 118:221101, 2017. DOI: 10.1103/PhysRevLett.118.221101.

[198] B. P. Abbott et al. Gw170814: A three-detector observation of gravitational waves from a binary black hole coalescence. Phys. Rev. Lett., 119:141101, 2017. DOI: 10.1103/PhysRevLett.119.141101.

[199] Hiroko Niikura, Masahiro Takada, Naoki Yasuda, Robert H. Lupton, Takahiro Sumi, Surhud More, Toshiki Kurita, Sunao Sugiyama, Anupreeta More, Masamune Oguri, and Masashi Chiba. Microlensing constraints on primordial black holes with subaru/hsc andromeda observations. Nature Astronomy, 3(6):524534, 2019. DOI: 10.1038/s41550-019-0723-1.

[200] J. R. Espinosa, D. Racco, and A. Riotto. Cosmological signature of the standard model higgs vacuum instability: Primordial black holes as dark matter. Phys. Rev. Lett., 120:121301, 2018. DOI: 10.1103/PhysRevLett.120.121301.

[201] P. Meszaros. Primeval black holes and galaxy formation. A&A, 38(1): 5–13, 1975. URL: https://ui.adsabs.harvard.edu/abs/1975A&A....38...5M.

[202] G. F. Chapline. Cosmological effects of primordial black holes. Nature, 253 (5489):251–252, 1975. DOI: 10.1038/253251a0.

[203] Juan García-Bellido. Massive primordial black holes as dark matter and their detection with gravitational waves. Journal of Physics: Conference Series, 840:012032, 2017. DOI: 10.1088/1742-6596/840/1/012032.

[204] George M. Fuller, Alexander Kusenko, and Volodymyr Takhistov. Primordial black holes and r-process nucleosynthesis. Phys. Rev. Lett., 119:061101, 2017. DOI: 10.1103/PhysRevLett.119.061101.

[205] S. W. Hawking. Black hole explosions? Nature, 248(5443):30–31, 1974. DOI: 10.1038/248030a0.

[206] S. W. Hawking. Particle Creation by Black Holes. Commun. Math. Phys., 43: 199–220, 1975. DOI: 10.1007/BF02345020. [Erratum: Commun.Math.Phys. 46, 206 (1976)].

[207] Gulab C. Dewangan, Lev Titarchuk, and Richard E. Griffiths. Black hole mass of the ultraluminous x-ray source m82 x-1. ApJ, 637(1):L21–L24, 2006. DOI: 10.1086/499235.

[208] N. Madhusudhan, S. Justham, L. Nelson, B. Paxton, E. Pfahl, Ph. Podsiadlowski, and S. Rappaport. Models of ultraluminous x-ray sources with intermediate-mass black holes. ApJ, 640(2):918–922, 2006. DOI: 10.1086/500238.

[209] Ji-Feng Liu, Joel N. Bregman, Yu Bai, Stephen Justham, and Paul Crowther. Puzzling accretion onto a black hole in the ultraluminous x-ray source m 101 ulx-1. Nature, 503(7477):500503, 2013. DOI: 10.1038/nature12762.

[210] Sébastien Clesse and Juan García-Bellido. Seven hints for primordial black hole dark matter. Physics of the Dark Universe, 22:137–146, 2018. DOI: 10.1016/j.dark.2018.08.004.

[211] Edward L. Wright. On the Density of Primordial Black Holes in the Galactic Halo. ApJ, 459:487, 1996. DOI: 10.1086/176910.

[212] R. Lehoucq, M. Cassé, J. M. Casandjian, and I. Grenier. New constraints on the primordial black hole number density from Galactic γ-ray astronomy. A&A, 502(1):37–43, 2009. DOI: 10.1051/0004-6361/200911961.

[213] B. J. Carr. Some cosmological consequences of primordial black-hole evaporations. ApJ, 206:8–25, 1976. DOI: 10.1086/154351.

[214] D. N. Page and S. W. Hawking. Gamma rays from primordial black holes. ApJ, 206:1–7, 1976. DOI: 10.1086/154350.

[215] D. B. Cline, D. A. Sanders, and W. Hong. Further evidence for some gamma-ray bursts consistent with primordial black hole evaporation. ApJ, 486(1): 169–178, 1997. DOI: 10.1086/304480.

[216] Anne M. Green. Viability of primordial black holes as short period gamma-ray bursts. Phys. Rev. D, 65:027301, 2001. DOI: 10.1103/PhysRevD.65.027301.

[217] K. M. Belotsky, A. E. Dmitriev, E. A. Esipova, V. A. Gani, A. V. Grobov, M. Yu. Khlopov, A. A. Kirillov, S. G. Rubin, and I. V. Svadkovsky. Signatures of primordial black hole dark matter. Modern Physics Letters A, 29 (37):1440005, 2014. DOI: 10.1142/s0217732314400057.

[218] K.M. Belotsky and A.A. Kirillov. Primordial black holes with mass 1016-1017g and reionization of the universe. J. Cosmol. Astropart. Phys., 2015 (01):041–041, 2015. DOI: 10.1088/1475-7516/2015/01/041.

[219] Anne M Green and Bradley J Kavanagh. Primordial black holes as a dark matter candidate. Journal of Physics G: Nuclear and Particle Physics, 48 (4):043001, 2021. DOI: 10.1088/1361-6471/abc534.

[220] Bernard Carr and Florian Kühnel. Primordial black holes as dark matter: Recent developments. Annual Review of Nuclear and Particle Science, 70 (1):355–394, 2020. DOI: 10.1146/annurev-nucl-050520-125911.

[221] Andi Hektor, Gert Hütsi, Luca Marzola, Martti Raidal, Ville Vaskonen, and Hardi Veermäe. Constraining primordial black holes with the edges 21-cm absorption signal. Phys. Rev. D, 98(2), 2018. DOI: 10.1103/physrevd.98.023503.

[222] Steven J. Clark, Bhaskar Dutta, Yu Gao, Yin-Zhe Ma, and Louis E. Strigari. 21 cm limits on decaying dark matter and primordial black holes. Phys. Rev. D, 98(4), 2018. DOI: 10.1103/physrevd.98.043006.

[223] Olga Mena, Sergio Palomares-Ruiz, Pablo Villanueva-Domingo, and Samuel J. Witte. Constraining the primordial black hole abundance with 21-cm cosmology. Phys. Rev. D, 100(4), 2019. DOI: 10.1103/physrevd.100.043540.

[224] Yupeng Yang. Constraints on primordial black holes and curvature perturbations from the global 21-cm signal. Phys. Rev. D, 102(8), 2020. DOI: 10.1103/physrevd.102.083538.

[225] Ashadul Halder and Shibaji Banerjee. Bounds on abundance of primordial black hole and dark matter from edges 21-cm signal. Phys. Rev. D, 103(6), 2021. DOI: 10.1103/physrevd.103.063044.

[226] Hiroyuki Tashiro and Kenji Kadota. Constraining mixed dark-matter scenarios of wimps and primordial black holes from cmb and 21-cm observations. Phys. Rev. D, 103(12), 2021. DOI: 10.1103/physrevd.103.123532.

[227] Yupeng Yang. The abundance of primordial black holes from the global 21cm signal and extragalactic gamma-ray background. The European Physical Journal Plus, 135(9), 2020. DOI: 10.1140/epjp/s13360-020-00710-3.

[228] Pablo Villanueva-Domingo and Kiyotomo Ichiki. 21 cm forest constraints on primordial black holes, 2021.

[229] Subrahmanyan Chandrasekhar and Steven L. Detweiler. On the Reflection and Transmission of Neutrino Waves by a Kerr Black Hole. Proc. Roy. Soc. Lond. A, 352:325–338, 1977. DOI: 10.1098/rspa.1977.0002.

[230] Brett E. Taylor, Chris M. Chambers, and William A. Hiscock. Evaporation of a kerr black hole by emission of scalar and higher spin particles. Phys. Rev. D, 58(4), 1998. DOI: 10.1103/physrevd.58.044012.

[231] Alexandre Arbey, Jérémy Auffinger, Pearl Sandick, Barmak Shams Es Haghi, and Kuver Sinha. Precision calculation of dark radiation from spinning primordial black holes and early matter-dominated eras. Phys. Rev. D, 103 (12), 2021. DOI: 10.1103/physrevd.103.123549.

[232] Ranjan Laha, Philip Lu, and Volodymyr Takhistov. Gas heating from spinning and non-spinning evaporating primordial black holes. Physics Letters B, 820:136459, 2021. DOI: 10.1016/j.physletb.2021.136459.

[233] Don N. Page. Particle emission rates from a black hole: Massless particles from an uncharged, nonrotating hole. Phys. Rev. D, 13:198–206, 1976. DOI: 10.1103/PhysRevD.13.198.

[234] Michael Kesden, Guglielmo Lockhart, and E. Sterl Phinney. Maximum black-hole spin from quasicircular binary mergers. Phys. Rev. D, 82(12), 2010. DOI: 10.1103/physrevd.82.124045.

[235] Eric Cotner and Alexander Kusenko. Primordial black holes from scalar field evolution in the early universe. Phys. Rev. D, 96(10), 2017. DOI: 10.1103/physrevd.96.103002.

[236] Tomohiro Harada, Chul-Moon Yoo, Kazunori Kohri, Yasutaka Koga, and Takeru Monobe. Spins of primordial black holes formed in the radiation-dominated phase of the universe: First-order effect. ApJ, 908(2):140, 2021. DOI: 10.3847/1538-4357/abd9b9.

[237] V. De Luca, V. Desjacques, G. Franciolini, A. Malhotra, and A. Riotto. The initial spin probability distribution of primordial black holes. J. Cosmol. Astropart. Phys., 2019(05):018–018, 2019. DOI: 10.1088/1475-7516/2019/05/018.

[238] V. De Luca, G. Franciolini, P. Pani, and A. Riotto. The evolution of primordial black holes and their final observable spins. J. Cosmol. Astropart. Phys., 2020(04):052–052, 2020. DOI: 10.1088/1475-7516/2020/04/052.

[239] Tomohiro Harada, Chul-Moon Yoo, Kazunori Kohri, and Ken-Ichi Nakao. Spins of primordial black holes formed in the matter-dominated phase of the universe. Phys. Rev. D, 96(8), 2017. DOI: 10.1103/physrevd.96.083517.

[240] Florian Kühnel. Enhanced detectability of spinning primordial black holes. Eur. Phys. J. C, 80(3), 2020. DOI: 10.1140/epjc/s10052-020-7807-z.

[241] Marcos M. Flores and Alexander Kusenko. Spins of primordial black holes formed in different cosmological scenarios. Phys. Rev. D, 104(6), 2021. DOI: 10.1103/physrevd.104.063008.

[242] Alexandre Arbey, Jérémy Auffinger, and Joseph Silk. Evolution of primordial black hole spin due to hawking radiation. MNRAS, 494(1):1257–1262, 2020. DOI: 10.1093/mnras/staa765.

[243] Minxi He and Teruaki Suyama. Formation threshold of rotating primordial black holes. Phys. Rev. D, 100(6), 2019. DOI: 10.1103/physrevd.100.063520.

[244] Eric Cotner, Alexander Kusenko, Misao Sasaki, and Volodymyr Takhistov. Analytic description of primordial black hole formation from scalar field fragmentation. J. Cosmol. Astropart. Phys., 2019(10):077–077, 2019. DOI: 10.1088/1475-7516/2019/10/077.

[245] Ruifeng Dong, William H. Kinney, and Dejan Stojkovic. Gravitational wave production by hawking radiation from rotating primordial black holes. J. Cosmol. Astropart. Phys., 2016(10):034–034, 2016. DOI: 10.1088/1475-7516/2016/10/034.

[246] Shikhar Mittal, Anupam Ray, Girish Kulkarni, and Basudeb Dasgupta. Constraining primordial black holes as dark matter using the global 21-cm signal with x-ray heating and excess radio background. Journal of Cosmology and Astroparticle Physics, 2022(03):030, 2022. DOI: 10.1088/1475-7516/2022/03/030.

[247] Tracy R. Slatyer. Indirect dark matter signatures in the cosmic dark ages. ii. ionization, heating, and photon production from arbitrary energy injections. Phys. Rev. D, 93:023521, 2016. DOI: 10.1103/PhysRevD.93.023521.

[248] Tracy R. Slatyer. Indirect dark matter signatures in the cosmic dark ages. i. generalizing the bound on s-wave dark matter annihilation from planck results. Phys. Rev. D, 93:023527, 2016. DOI: 10.1103/PhysRevD.93.023527.

[249] Hongwan Liu, Gregory W. Ridgway, and Tracy R. Slatyer. Code package for calculating modified cosmic ionization and thermal histories with dark matter and other exotic energy injections. Phys. Rev. D, 101(2), 2020. DOI: 10.1103/physrevd.101.023530.

[250] Jane H. MacGibbon and B. R. Webber. Quark- and gluon-jet emission from primordial black holes: The instantaneous spectra. Phys. Rev. D, 41: 3052–3079, 1990. DOI: 10.1103/PhysRevD.41.3052.

[251] Alexandre Arbey and Jérémy Auffinger. Blackhawk: a public code for calculating the hawking evaporation spectra of any black hole distribution. Eur. Phys. J. C, 79(8), 2019. DOI: 10.1140/epjc/s10052-019-7161-1.

[252] Alexandre Arbey and Jérémy Auffinger. Physics beyond the standard model with blackhawk v2.0. Eur. Phys. J. C, 81(10), 2021. DOI: 10.1140/epjc/s10052-021-09702-8.

[253] Adam Coogan, Logan Morrison, and Stefano Profumo. Hazma: a python toolkit for studying indirect detection of sub-gev dark matter. Journal of Cosmology and Astroparticle Physics, 2020(01):056056, 2020. DOI: 10.1088/1475-7516/2020/01/056.

[254] Jens Chluba, D. Paoletti, F. Finelli, and J. A. Rubiño-Martín. Effect of primordial magnetic fields on the ionization history. MNRAS, 451(2): 2244–2250, 2015. DOI: 10.1093/mnras/stv1096.

[255] D. J. Fixsen. THE TEMPERATURE OF THE COSMIC MICROWAVE BACKGROUND. ApJ, 707(2):916–920, 2009. DOI: 10.1088/0004-637x/707/2/916.

[256] Sai Wang, Dong-Mei Xia, Xukun Zhang, Shun Zhou, and Zhe Chang. Constraining primordial black holes as dark matter at juno. Phys. Rev. D, 103 (4), 2021. DOI: 10.1103/physrevd.103.043010.

[257] Don N. Page. Particle emission rates from a black hole. ii. massless particles from a rotating hole. Phys. Rev. D, 14:3260–3273, 1976. DOI: 10.1103/PhysRevD.14.3260.

[258] Don N. Page. Particle emission rates from a black hole. iii. charged leptons from a nonrotating hole. Phys. Rev. D, 16:2402–2411, 1977. DOI: 10.1103/PhysRevD.16.2402.

[259] Shiv K. Sethi and Kandaswamy Subramanian. Primordial magnetic fields in the post-recombination era and early reionization. MNRAS, 356(2):778–788, 2005. DOI: 10.1111/j.1365-2966.2004.08520.x.

[260] Eun-jin Kim, Angela Olinto, and Robert Rosner. Generation of density perturbations by primordial magnetic fields. Astrophys. J., 468:28, 1996. DOI: 10.1086/177667.

[261] R. Beck and P. Hoernes. Magnetic spiral arms in the galaxy ngc6946. Nature, 379:47–49, 1996. DOI: 10.1038/379047a0.

[262] Hiroyuki Tashiro and Naoshi Sugiyama. Probing primordial magnetic fields with the 21cm fluctuations. MNRAS, 372:1060–1068, 2006. DOI: 10.1111/j.1365-2966.2006.10901.x.

[263] R. Beck et al. Structure, dynamical impact and origin of magnetic fields in nearby galaxies in the SKA era. In Advancing Astrophysics with the Square Kilometre Array (AASKA14), page 94, 2015.

[264] Rainer Beck. Magnetic fields in the nearby spiral galaxy IC 342: A multi-frequency radio polarization study. A&A, 578:A93, 2015. DOI: 10.1051/0004-6361/201425572.

[265] Craig J. Hogan. Magnetohydrodynamic effects of a first-order cosmological phase transition. Phys. Rev. Lett., 51:1488–1491, 1983. DOI: 10.1103/PhysRevLett.51.1488.

[266] Nigel Weiss. Dynamos in planets, stars and galaxies. Astronomy & Geophysics, 43(3):3.9–3.14, 2002. DOI: 10.1046/j.1468-4004.2002.43309.x.

[267] Beck Rainer. Magnetic fields in normal galaxies. Phil. Trans. R. Soc. A., 358:777–796, 2000. DOI: 10.1098/rsta.2000.0558.

[268] Rainer Beck, Luke Chamandy, Ed Elson, and Eric G. Blackman. Synthesizing observations and theory to understand galactic magnetic fields: Progress and challenges. Galaxies, 8(1), 2020. DOI: 10.3390/galaxies8010004.

[269] Vogt, C. and Enßlin, T. A. A bayesian view on faraday rotation maps - seeing the magnetic power spectra in galaxy clusters. A&A, 434(1):67–76, 2005. DOI: 10.1051/0004-6361:20041839.

[270] Taylor, A. M., Vovk, I., and Neronov, A. Extragalactic magnetic fields constraints from simultaneous gev-tev observations of blazars. A&A, 529: A144, 2011. DOI: 10.1051/0004-6361/201116441.

[271] T Vernstrom, G Heald, F Vazza, T J Galvin, J L West, N Locatelli, N Fornengo, and E Pinetti. Discovery of magnetic fields along stacked cosmic filaments as revealed by radio and x-ray emission. MNRAS, 505(3):41784196, 2021. DOI: 10.1093/mnras/stab1301.

[272] Dario Grasso and Hector R. Rubinstein. Magnetic fields in the early universe. Physics Reports, 348(3):163 – 266, 2001. DOI: 10.1016/S0370-1573(00)00110-1.

[273] Kandaswamy Subramanian. The origin, evolution and signatures of primordial magnetic fields. Rept. Prog. Phys., 79(7):076901, 2016. DOI: 10.1088/0034-4885/79/7/076901.

[274] Serena Bertone, Corina Vogt, and Torsten EnSSlin. Magnetic field seeding by galactic winds. MNRAS, 370(1):319–330, 2006. DOI: 10.1111/j.1365-2966.2006.10474.x.

[275] Michael S. Turner and Lawrence M. Widrow. Inflation-produced, large-scale magnetic fields. Phys. Rev. D, 37:2743–2754, 1988. DOI: 10.1103/PhysRevD.37.2743.

[276] Bharat Ratra. Cosmological "Seed" Magnetic Field from Inflation. ApJ, 391:L1, 1992. DOI: 10.1086/186384.

[277] David Lemoine and Martin Lemoine. Primordial magnetic fields in string cosmology. Phys. Rev. D, 52:1955–1962, 1995. DOI: 10.1103/PhysRevD.52.1955.

[278] M. Gasperini, M. Giovannini, and G. Veneziano. Primordial magnetic fields from string cosmology. Phys. Rev. Lett., 75:3796–3799, 1995. DOI: 10.1103/PhysRevLett.75.3796.

[279] Vittoria Demozzi, Viatcheslav Mukhanov, and Hector Rubinstein. Magnetic fields from inflation? Journal of Cosmology and Astroparticle Physics, 2009 (08):025–025, 2009. DOI: 10.1088/1475-7516/2009/08/025.

[280] Alireza Talebian, Amin Nassiri-Rad, and Hassan Firouzjahi. Revisiting magnetogenesis during inflation. Phys. Rev. D, 102:103508, 2020. DOI: 10.1103/PhysRevD.102.103508.

[281] Gordon Baym, Dietrich Bödeker, and Larry McLerran. Magnetic fields produced by phase transition bubbles in the electroweak phase transition. Phys. Rev. D, 53:662–667, 1996. DOI: 10.1103/PhysRevD.53.662.

[282] Jean M. Quashnock, Abraham Loeb, and David N. Spergel. Magnetic Field Generation during the Cosmological QCD Phase Transition. ApJ Letters, 344:L49, 1989. DOI: 10.1086/185528.

[283] Christopher T. Hill, Hardy M. Hodges, and Michael S. Turner. Bosonic superconducting cosmic strings. Phys. Rev. D, 37:263–282, 1988. DOI: 10.1103/PhysRevD.37.263.

[284] Tanmay Vachaspati and Alexander Vilenkin. Large-scale structure from wiggly cosmic strings. Phys. Rev. Lett., 67:1057–1061, 1991. DOI: 10.1103/PhysRevLett.67.1057.

[285] E. R. Harrison. Generation of Magnetic Fields in the Radiation ERA. MNRAS, 147(3):279–286, 1970. DOI: 10.1093/mnras/147.3.279.

[286] Karsten Jedamzik and Levon Pogosian. Relieving the hubble tension with primordial magnetic fields. Phys. Rev. Lett., 125(18), 2020. DOI: 10.1103/physrevlett.125.181302.

[287] Pranjal Trivedi, T. R. Seshadri, and Kandaswamy Subramanian. Cosmic microwave background trispectrum and primordial magnetic field limits. Phys. Rev. Lett., 108:231301, 2012. DOI: 10.1103/PhysRevLett.108.231301.

[288] Pranjal Trivedi, Kandaswamy Subramanian, and T. R. Seshadri. Primordial magnetic field limits from the CMB trispectrum: Scalar modes and Planck constraints. Phys. Rev. D, 89(4):043523, 2014. DOI: 10.1103/PhysRevD.89.043523.

[289] Pravin Kumar Natwariya and Jitesh R Bhatt. Edges signal in the presence of magnetic fields. MNRAS Lett., 497(1):L35–L39, 2020. DOI: 10.1093/mnrasl/slaa108.

[290] John Ellis, Malcolm Fairbairn, Marek Lewicki, Ville Vaskonen, and Alastair Wickens. Intergalactic magnetic fields from first-order phase transitions. J. Cosmol. Astropart. Phys., 2019(09):019–019, 2019. DOI: 10.1088/1475-7516/2019/09/019.

[291] The FLAT Collaboration and Jonathan Biteau. The search for spatial extension in high-latitude sources detected by the fermi large area telescope. ApJS, 237(2):32, 2018. DOI: 10.3847/1538-4365/aacdf7.

[292] F. Tavecchio, G. Ghisellini, L. Foschini, G. Bonnoli, G. Ghirlanda, and P. Coppi. The intergalactic magnetic field constrained by Fermi/Large Area Telescope observations of the TeV blazar 1ES 0229+200. MNRAS: Letters, 406(1):L70–L74, 2010. DOI: 10.1111/j.1745-3933.2010.00884.x.

[293] Baolian Cheng, Angela V. Olinto, David N. Schramm, and James W. Truran. Constraints on the strength of primordial magnetic fields from big bang nucleosynthesis reexamined. Phys. Rev. D, 54:4714–4718, 1996. DOI: 10.1103/PhysRevD.54.4714.

[294] J. J. Matese and R. F. O'Connell. Neutron beta decay in a uniform constant magnetic field. Phys. Rev., 180:1289–1292, 1969. DOI: 10.1103/PhysRev.180.1289.

[295] George Greenstein. Primordial helium production in magnetic cosmologies. Nature, 223:938–939, 1969. DOI: 10.1038/223938b0.

[296] Hiroyuki Tashiro and Naoshi Sugiyama. The early reionization with the primordial magnetic fields. MNRAS, 368:965–970, 2006. DOI: 10.1111/j.1365-2966.2006.10178.x.

[297] Kanhaiya L. Pandey, T. Roy Choudhury, Shiv K. Sethi, and Andrea Ferrara. Reionization constraints on primordial magnetic fields. MNRAS, 451(2): 1692–1700, 2015. DOI: 10.1093/mnras/stv1055.

[298] Karsten Jedamzik and Andrey Saveliev. Stringent limit on primordial magnetic fields from the cosmic microwave background radiation. Phys. Rev. Lett., 123:021301, 2019. DOI: 10.1103/PhysRevLett.123.021301.

[299] K. Subramanian. Magnetic fields in the early universe. Astronomische Nachrichten, 331(1):110–120, 2010. DOI: 10.1002/asna.200911312.

[300] Arun Kumar Pandey, Pravin Kumar Natwariya, and Jitesh R. Bhatt. Magnetic fields in a hot dense neutrino plasma and the gravitational waves. Phys. Rev. D, 101:023531, 2020. DOI: 10.1103/PhysRevD.101.023531.

[301] Ankita Bera, Kanan K Datta, and Saumyadip Samui. Primordial magnetic fields during the cosmic dawn in light of EDGES 21-cm signal. MNRAS, 498 (1):918–925, 2020. DOI: 10.1093/mnras/staa1529.

[302] F. H. Shu. The physics of astrophysics. Volume II: Gas dynamics. ISBN 0-935702-65-2, 1992. URL: http://adsabs.harvard.edu/abs/1992pavi.book.....S.

[303] Dominik R. G. Schleicher, Robi Banerjee, and Ralf S. Klessen. Reionization: A probe for the stellar population and the physics of the early universe. Phys. Rev. D, 78:083005, 2008. DOI: 10.1103/PhysRevD.78.083005.

[304] Chang Feng and Gilbert Holder. Enhanced global signal of neutral hydrogen due to excess radiation at cosmic dawn. ApJ, 858(2):L17, 2018. DOI: 10.3847/2041-8213/aac0fe.

[305] Roger, R. S., Costain, C. H., Landecker, T. L., and Swerdlyk, C. M. The radio emission from the galaxy at 22 mhz. Astron. Astrophys. Suppl. Ser., 137(1):7–19, 1999. DOI: 10.1051/aas:1999239.

[306] K. Maeda, H. Alvarez, J. Aparici, J. May, and P. Reich. A 45-MHz continuum survey of the northern hemisphere. A&AS, 140:145–154, 1999. DOI: 10.1051/aas:1999413.

[307] C. G. T. Haslam et al. A 408 MHz all-sky continuum survey. I - Observations at southern declinations and for the North Polar region. A&A, 100: 209–219, 1981. URL: https://ui.adsabs.harvard.edu/abs/1981A&A...100..209H.

[308] P. Reich and W. Reich. A radio continuum survey of the northern sky at 1420 MHz. II. A&AS, 63:205, 1986. URL: https://ui.adsabs.harvard.edu/abs/1986A&AS...63..205R.

[309] D. J. Fixsen and J. C. Mather. The spectral results of the far-infrared absolute spectrophotometer instrument on cobe. The Astrophysical Journal, 581(2):817, 2002. DOI: 10.1086/344402.

[310] Anastasia Fialkov and Rennan Barkana. Signature of excess radio background in the 21-cm global signal and power spectrum. MNRAS, 486(2): 1763–1773, 2019. DOI: 10.1093/mnras/stz873.

[311] Itamar Reis, Anastasia Fialkov, and Rennan Barkana. High-redshift radio galaxies: a potential new source of 21-cm fluctuations. MNRAS, 2020. DOI: 10.1093/mnras/staa3091. staa3091.

[312] Yupeng Yang. Contributions of dark matter annihilation to the global 21 cm spectrum observed by the edges experiment. Phys. Rev. D, 98:103503, 2018. DOI: 10.1103/PhysRevD.98.103503.

[313] R Mondal et al. Tight constraints on the excess radio background at z = 9.1 from LOFAR. MNRAS, 498(3):4178–4191, 2020. DOI: 10.1093/mnras/staa2422.

[314] Alon Banet, Rennan Barkana, Anastasia Fialkov, and Or Guttman. Quantiles as robust probes of non-gaussianity in 21-cm images. MNRAS, 503(1): 12211232, 2021. DOI: 10.1093/mnras/stab318.

[315] A. Ewall-Wice, T.-C. Chang, J. Lazio, O. Doré, M. Seiffert, and R. A. Monsalve. Modeling the radio background from the first black holes at cosmic dawn: Implications for the 21 cm absorption amplitude. ApJ, 868(1):63, 2018. DOI: 10.3847/1538-4357/aae51d.

[316] Peter L. Biermann, Biman B. Nath, Laureniu I. Caramete, Benjamin C. Harms, Todor Stanev, and Julia Becker Tjus. Cosmic backgrounds due to the formation of the first generation of supermassive black holes. MNRAS, 441(2):1147–1156, 2014. DOI: 10.1093/mnras/stu541.

[317] Ranita Jana, Biman B Nath, and Peter L Biermann. Radio background and IGM heating due to Pop III supernova explosions. MNRAS, 483(4): 5329–5333, 2018. DOI: 10.1093/mnras/sty3426.

[318] Jayce Dowell, Gregory B. Taylor, Frank K. Schinzel, Namir E. Kassim, and Kevin Stovall. The LWA1 Low Frequency Sky Survey. MNRAS, 469(4): 4537–4550, 2017. DOI: 10.1093/mnras/stx1136.

[319] K. Lawson and A.R. Zhitnitsky. The 21ăcm absorption line and the axion quark nugget dark matter model. Physics of the Dark Universe, 24:100295, 2019. DOI: 10.1016/j.dark.2019.100295.

[320] Kyle Lawson and Ariel R. Zhitnitsky. Isotropic radio background from quark nugget dark matter. Physics Letters B, 724(1):17 – 21, 2013. DOI: 10.1016/j.physletb.2013.05.070.

[321] D. G. Levkov, A. G. Panin, and I. I. Tkachev. Radio-emission of axion stars. Phys. Rev. D, 102:023501, 2020. DOI: 10.1103/PhysRevD.102.023501.

[322] Richard H Mebane, Jordan Mirocha, and Steven R Furlanetto. The effects of population III radiation backgrounds on the cosmological 21-cm signal. MNRAS, 493(1):1217–1226, 2020. DOI: 10.1093/mnras/staa280.

[323] Takeo Moroi, Kazunori Nakayama, and Yong Tang. Axion-photon conversion and effects on 21ăcm observation. Phys. Lett. B, 783:301–305, 2018. DOI: 10.1016/J.PHYSLETB.2018.07.002.

[324] D. Aristizabal Sierra and Chee Sheng Fong. The EDGES signal: An imprint from the mirror world? Phys. Lett. B, 784:130–136, 2018. DOI: 10.1016/J.PHYSLETB.2018.07.047.

[325] Robert Brandenberger, Bryce Cyr, and Rui Shi. Constraints on superconducting cosmic strings from the global 21-cm signal before reionization. J. Cosmol. Astropart. Phys., 2019(09):009–009, 2019. DOI: 10.1088/1475-7516/2019/09/009.

[326] M. Chianese, P. Di Bari, K. Farrag, and R. Samanta. Probing relic neutrino radiative decays with 21cm cosmology. Physics Letters B, 790:64 – 70, 2019. DOI: 10.1016/j.physletb.2018.09.040.

[327] A. Kogut et al. Arcade 2 observations of galactic radio emission. ApJ, 734 (1):4, 2011. DOI: 10.1088/0004-637x/734/1/4.

[328] Shiv K Sethi, Biman B. Nath, and Kandaswamy Subramanian. Primordial magnetic fields and formation of molecular hydrogen. MNRAS, 387:1589, 2008. DOI: 10.1111/j.1365-2966.2008.13302.x.

[329] Karsten Jedamzik, Vi šnja Katalinić, and Angela V. Olinto. Damping of cosmic magnetic fields. Phys. Rev. D, 57:3264–3284, 1998. DOI: 10.1103/PhysRevD.57.3264.

[330] Kerstin E Kunze and Eiichiro Komatsu. Constraining primordial magnetic fields with distortions of the black-body spectrum of the cosmic microwave background: pre- and post-decoupling contributions. J. Cosmol. Astropart. Phys., 2014(01):009–009, 2014. DOI: 10.1088/1475-7516/2014/01/009.

[331] Kandaswamy Subramanian and John D. Barrow. Magnetohydrodynamics in the early universe and the damping of noninear Alfven waves. Phys. Rev., D58:083502, 1998. DOI: 10.1103/PhysRevD.58.083502.

[332] Andrew Mack, Tina Kahniashvili, and Arthur Kosowsky. Microwave background signatures of a primordial stochastic magnetic field. Phys. Rev. D, 65:123004, 2002. DOI: 10.1103/PhysRevD.65.123004.

[333] L.D. LANDAU and E.M. LIFSHITZ. Fluid Mechanics (Second Edition), volume 6. Pergamon, second edition edition, 1987. ISBN 978-0-08-033933-7. DOI: 10.1016/C2013-0-03799-1.

[334] Ruth Durrer and Chiara Caprini. Primordial magnetic fields and causality. J. Cosmol. Astropart. Phys., 0311:010, 2003. DOI: 10.1088/1475-7516/2003/11/010.

[335] Chiara Caprini, Ruth Durrer, and Tina Kahniashvili. Cosmic microwave background and helical magnetic fields: The tensor mode. Phys. Rev. D, 69: 063006, 2004. DOI: 10.1103/PhysRevD.69.063006.

[336] X. Asselin, G. Girardi, P. Salati, and A. Blanchard. Hot-warm unstable supersymmetric dark matter and galaxy formation. Nuclear Physics B, 310 (3):669–692, 1988. DOI: 10.1016/0550-3213(88)90098-3.

[337] Maresuke Shiraishi, Hiroyuki Tashiro, and Kiyotomo Ichiki. 21 cm fluctuations from primordial magnetic fields. Phys. Rev. D, 89:103522, 2014. DOI: 10.1103/PhysRevD.89.103522.

[338] Planck Collaboration et al. Planck 2013 results. xvi. cosmological parameters. A&A, 571:A16, 2014. DOI: 10.1051/0004-6361/201321591.

[339] Takeo Moroi, Kazunori Nakayama, and Yong Tang. Axion-photon conversion and effects on 21 cm observation. Phys. Lett., B783:301–305, 2018. DOI: 10.1016/j.physletb.2018.07.002.

[340] Sean Fraser et al. The edges 21 cm anomaly and properties of dark matter. Phys. Lett. B, 785:159 – 164, 2018. DOI: 10.1016/j.physletb.2018.08.035.

[341] Maxim Pospelov, Josef Pradler, Joshua T. Ruderman, and Alfredo Urbano. Room for new physics in the rayleigh-jeans tail of the cosmic microwave background. Phys. Rev. Lett., 121:031103, 2018. DOI: 10.1103/PhysRevLett.121.031103.

[342] Hongwan Liu, Nadav Joseph Outmezguine, Diego Redigolo, and Tomer Volansky. Reviving millicharged dark matter for 21-cm cosmology. Phys. Rev. D, 100:123011, 2019. DOI: 10.1103/PhysRevD.100.123011.

[343] Leonid Chuzhoy and Paul R. Shapiro. Heating and cooling of the early intergalactic medium by resonance photons. ApJ, 655(2):843–846, 2007. DOI: 10.1086/510146.

[344] Leonid Chuzhoy and Paul R. Shapiro. Ultraviolet Pumping of Hyperfine Transitions in the Light Elements, with Application to 21 cm Hydrogen and 92 cm Deuterium Lines from the Early Universe. ApJ, 651(1):1–7, 2006. DOI: 10.1086/507670.

[345] Rennan Barkana. Possible interaction between baryons and dark-matter particles revealed by the first stars. Nature, 555(7694):71–74, 2018. DOI: 10.1038/nature25791.

[346] Hiroyuki Tashiro, Kenji Kadota, and Joseph Silk. Effects of dark matter-baryon scattering on redshifted 21 cm signals. Phys. Rev. D, 90(8):083522, 2014. DOI: 10.1103/PhysRevD.90.083522.

[347] Julian B. Muñoz, Ely D. Kovetz, and Yacine Ali-Haïmoud. Heating of baryons due to scattering with dark matter during the dark ages. Phys. Rev. D, 92:083528, 2015. DOI: 10.1103/PhysRevD.92.083528.

[348] Cora Dvorkin, Kfir Blum, and Marc Kamionkowski. Constraining Dark Matter-Baryon Scattering with Linear Cosmology. Phys. Rev., D89(2): 023519, 2014. DOI: 10.1103/PhysRevD.89.023519.

[349] Asher Berlin, Dan Hooper, Gordan Krnjaic, and Samuel D. McDermott. Severely Constraining Dark-Matter Interpretations of the 21-cm Anomaly. Phys. Rev. Lett., 121(1):011102, 2018. DOI: 10.1103/PhysRevLett.121.011102.

[350] Cyril Creque-Sarbinowski, Lingyuan Ji, Ely D. Kovetz, and Marc Kamionkowski. Direct millicharged dark matter cannot explain the edges signal. Phys. Rev. D, 100(2), 2019. DOI: 10.1103/physrevd.100.023528.

[351] Trey Driskell, Ethan O. Nadler, Jordan Mirocha, Andrew Benson, Kimberly K. Boddy, Timothy D. Morton, Jack Lashner, Rui An, and Vera Gluscevic. Structure formation and the global 21-cm signal in the presence of coulomb-like dark matter-baryon interactions, 2022. DOI: 10.48550/ARXIV.2209.04499.

[352] Pierre Sikivie. Axion dark matter and the 21-cm signal. Physics of the Dark Universe, 24:100289, 2019. DOI: 10.1016/j.dark.2019.100289.

[353] Jordan Mirocha and Steven R Furlanetto. What does the first highly redshifted 21-cm detection tell us about early galaxies? MNRAS, 483(2): 1980–1992, 2019. DOI: 10.1093/mnras/sty3260.

[354] Raghunath Ghara and Garrelt Mellema. Impact of Ly α heating on the global 21-cm signal from the Cosmic Dawn. MNRAS, 492(1):634–644, 2019. DOI: 10.1093/mnras/stz3513.

[355] Julian B. Muñoz and Abraham Loeb. A small amount of mini-charged dark matter could cool the baryons in the early Universe. Nature, 557(7707): 684–686, 2018. DOI: 10.1038/s41586-018-0151-x.

[356] B H Bransden, A Dalgarno, T L John, and M J Seaton. The Elastic Scattering of Slow Electrons by Hydrogen Atoms. Proc. Phys. Soc., 71(6):877–892, 1958. DOI: 10.1088/0370-1328/71/6/301.

[357] Julian B. Muñoz, Cora Dvorkin, and Abraham Loeb. 21-cm Fluctuations from Charged Dark Matter. Phys. Rev. Lett., 121(12):121301, 2018. DOI: 10.1103/PhysRevLett.121.121301.

[358] Tracy R. Slatyer and Chih-Liang Wu. Early-Universe constraints on dark matter-baryon scattering and their implications for a global 21ăcm signal. Phys. Rev. D, 98(2):023013, 2018. DOI: 10.1103/PhysRevD.98.023013.

[359] Peter H Sims and Jonathan C Pober. Testing for calibration systematics in the edges low-band data using bayesian model selection. MNRAS, 492(1): 22–38, 2019. DOI: 10.1093/mnras/stz3388.